Master's Thesis

Isospin-Violating Dark Matter and Direct Detection Experiments

Author:

Zakary F. Whittamore

Advisor:

Dr. James M. Cline

Department of Physics

McGill University, Montréal

December 2013

A thesis submitted to McGill University in partial fulfillment of the requirements of the degree of Master of Science.

MCGILL UNIVERSITY

Abstract

Faculty of Science
Department of Physics

Master of Science

Isospin-Violating Dark Matter and Direct Detection Experiments

by Zakary F. Whittamore

Hints of direct detection of dark matter have been presented by the DAMA, CoGeNT, and CRESST collaborations, despite a number of null results that seem to contradict such claims. Although standard spin-independent dark matter is not capable of reconciling the results, dark matter models containing isospin-violating couplings have shown promise in solving the issues surrounding direct detection of dark matter. Inelastic or momentum-dependent scattering dark matter has also been shown to help alleviate these tensions. In light of the 2012 XENON100 observations, updated analysis of surface event contamination at CoGeNT, revision of the energy resolution employed by XENON10, and new results from the CDMS-II silicon detectors, we study the extent to which spin-independent, spin-dependent, and combined models of isospin-violating dark matter are capable of explaining current direct detection data. Moreover, we explore the effect of an energy-dependent sodium quenching factor Q_{Na} for fitting the DAMA observations, and give an isospin-violating prediction for XENON1T. In addition to the usual analysis involving phase space plots, we investigate a halo-independent model of dark matter in the space of minimum velocities required for a dark matter particle to scatter off a given nucleus. For the first time, such an analysis is performed for models of dark matter which embrace both inelastic and isospin-violating couplings, as well as for dark matter with momentum- and spin-dependent interactions. With respect to the models considered herein, our results do not support a dark matter interpretation of direct detection data in either the standard or halo-independent formalisms.

UNIVERSITÉ DE MCGILL

Résumé

Faculté des Sciences

Département de Physique

Maître des Sciences

Matière Noire Isospin-Violation et Expériences de Détection Directe

par Zakary F. WHITTAMORE

Conseils de détection directe de la matière noire ont été présentés par les DAMA, CoGeNT, et CRESST collaborations, malgré un certain nombre de résultats nuls qui semblent contredire ces allégations. Bien que la norme matière noire indépendante du spin n'est pas capable de concilier la résultats, la matière noire modèles contenant couplages de isospin-violation ont montré des résultats prometteurs dans résolution des problèmes de détection directe de la matière noire. Diffusion inélastique ou dynamique dépendant de la matière noire a également été démontré que aider à atténuer ces tensions. À la lumière des observations XENON100 2012, analyse actualisée de la contamination de l' événement de surface à CoGeNT, la révision de la résolution de l'énergie utilisée par XENON10, et de nouveaux résultats provenant des détecteurs de silicium CDMS-II, nous étudier la mesure dans laquelle indépendante du spin, dépendant du spin, et des modèles combinés de la matière noire isospin-violation sont capables d'expliquer les données de détection directs actuels. De plus, nous explorons l'effet d'une trempe de sodium dépendant de l'énergie facteur Q_{Na} pour le montage des observations DAMA, et de donner une prévision de isospin-violation de XENON1T. En plus de l'analyse habituelle impliquant des parcelles de l'espace de phase, nous étudions un modèle de halo-indépendant de la matière noire dans l'espace des vitesses minimales requises pour une particule de matière noire se disperser hors d'un noyau donné. Pour la première fois, une telle analyse est effectuée pour les modèles de matière noire qui embrassent les deux couplages élastiques et isospin-violation, ainsi que de la matière noire avec des interactions dépendant du dynamique et spin. En ce qui concerne les modèles considérés ici, nos résultats ne soutiennent pas une question d'interprétation sombre de données de détection directe soit dans la norme ou formalismes halo-indépendant .

Acknowledgements

I wish to thank all of those who have contributed to this thesis project in one way or another.

First and foremost, I would like to express gratitude towards my graduate advisor Dr. James M. Cline. Jim afforded me the opportunity to pursue a M.Sc. degree at McGill university and introduced to me a field of physics which I have found overwhelmingly fascinating. Under his supervision, I completed my undergraduate research in a specialized topic involving isospin-violating dark matter, and with his guidance and suggestion, this evolved into the research topic of the present Master's thesis. I am grateful to Jim for his ongoing advice and support regarding this project.

Next, I would like to acknowledge those within the McGill physics department who have lent an invaluable hand. I am indebted to Zuowei Lui for aiding me in the computation of confidence intervals for some particularly non-trivial cases, and never hesitating to help with questions regarding the direct detection of dark matter. Also, thanks to Wei Xue for his collaboration during the initial stages of this research project, and a thank you to Pat Scott for his useful discussions surrounding likelihood functions.

Furthermore, I would like to acknowledge Eric Armengaud for his correspondence regarding the analysis of EDELWEISS-II data, and Eugenio Del Nobile for taking the time to explain some important details involving the halo-independent analysis of dark matter.

I would like to thank my peers and collegues who have helped me throughout my studies including: Madeleine Anthonisen, Omer Dirar, Justin Lee, Evan McDonough, and Giovanni Vizcardo. Last, but certainly not least, none of this would have been made possible without the unwavering support of my friends and family.

Contents

Abstract/Résumé i

Acknowledgements iii

List of Figures vi

List of Tables viii

Abbreviations x

1 Our Dark Universe **1**

1.1 Introduction 1
1.2 Evidence for dark matter 3
1.3 Criteria for dark matter candidates 6
1.3.1 The WIMP miracle 9
1.4 Outline 10

2 Theoretical Aspects of Dark Matter Scattering **12**

2.1 Differential event rates 12
2.1.1 Spin-independent differential cross section 13
2.1.2 Spin-dependent differential cross section 14
2.1.3 Momentum-dependent scattering 16
2.1.4 Detector isotopes 17
2.2 Total number of DM events 19
2.3 DM halo velocity distribution 20

3 Direct Detection Experiments **22**

3.1 CoGeNT 22
3.2 DAMA 24
3.3 CRESST-II 25
3.4 XENON100 26
3.5 XENON10 28

3.6 CDMS-Ge 29
3.7 CDMS-Si 30
3.8 SIMPLE 31
3.9 EDELWEISS-II 32

4 Isospin-Violating Dark Matter: A Review 34
4.1 From Dirac neutrinos to generalized IV couplings 34
4.2 Early results for IVDM 37
4.3 In light of new experimental results 40
4.4 Results from halo-independent analyses 41

5 Searching the Dark Matter Parameter Space 46
5.1 Methodology 47
5.2 Standard dark matter 49
5.3 Astrophysical uncertainties 52
5.4 Spin-independent isospin-violating dark matter 56
5.4.1 Inelastic scattering 60
5.4.2 Momentum-dependent scattering 63
5.4.3 Energy dependent DAMA quenching factors 66
5.4.4 Expectations for XENON1T 68
5.5 Spin-dependent isospin-violating DM 69
5.5.1 Inelastic and momentum-dependent couplings 71
5.6 Combined isospin-violating DM 74

6 A Halo-Independent Analysis 77
6.1 Theory: Converting to v_{min}-space 78
6.1.1 Inelastic halo-independent analysis 81
6.1.2 Determining upper limits in $\tilde{\eta}$-v_{min} space 83
6.2 Methodology 84
6.3 Defining consistency in v_{min}-space 85
6.4 Spin-independent results 86
6.5 Spin-dependent results 92

7 Summary and Conclusions 97
7.1 Future expectations for isospin-violating dark matter 98

A Integration of the Velocity Distribution 100

B Supplementary Phase Space Plots 102

C Supplementary Halo-Independent Plots 104

References 106

List of Figures

1.1 Data points for the velocity profile of spiral galaxy M33. Also shown, is the observed rotation curve, and the curve expected from the luminous disc. There is also a smaller contribution from galactic gas that is not shown. Figure taken from [10]. 4
1.2 CMB measurements in the nine-year WMAP analysis. The WMAP data (black) is given, as well as the extended CMB data set which includes SPT data (blue) and ACT data (orange). The solid grey curve represents the best fitting ΛCDM model to the WMAP data alone. Figure taken from [12]. 6

3.1 Forms of the electronic response function Q_y. The solid curve labelled Collar is from reference [69], dotted curve is that employed by XENON10 (see [68]), the dashed curve is the hypothetical intermediate ansatz. Figure taken from reference [71]. 29

5.1 Elastic isospin-conserving spin-independent DM fit to the experimental data in the σ_p^{SI}-M_{DM} plane with $f_n/f_p = 1.0$ and $\delta = 0.0$ keV. 50
5.2 Elastic purely protonic spin-dependent DM fit to the experimental data in the σ_p^{SD}-M_{DM} plane with $a_n = 0.0$, $a_p = 1.0$ and $\delta = 0.0$ keV. 51
5.3 Elastic purely neutronic spin-dependent DM fit to the experimental data in the σ_p^{SD}-M_{DM} plane with $a_n = 1.0$, $a_p = 0.0$ and $\delta = 0.0$ keV. 52
5.4 Elastic isospin-conserving spin-independent DM fit to the experimental data in the σ_p^{SI}-M_{DM} plane for different values of the Galactic escape velocity, v_{esc}. Solid (dashed) contours correspond to $v_{esc} = 608$ (498) km/s. 54
5.5 Elastic isospin-conserving spin-independent DM fit to the experimental data in the σ_p^{SI}-M_{DM} plane for different values of the Sun's circular velocity, v_0. Solid (dashed) contours correspond to $v_0 = 255$ (195) km/s. 55
5.6 Graphing the function $\xi(f_n/f_p)$ of equation (2.22) for various target material and for DM mass $M_{DM} = 10$ GeV. Vertical dashed lines correspond to the elastic SI benchmark value of the isospin violation ratio $f_n/f_p = -0.708$, and the value $f_n/f_p = -0.744$ for which larger f_n/f_p weaken the XENON100 bound relative the CoGeNT ROI. 57
5.7 Elastic isospin-violating spin-independent DM fit to the experimental data in the σ_p^{SI}-M_{DM} plane with $f_n/f_p = -0.708$ and $\delta = 0.0$ keV. 59
5.8 Elastic isospin-violating spin-independent DM fit to the experimental data in the σ_p^{SI}-M_{DM} plane for the upper limit value of the sodium quenching factor, $Q_{\mathrm{Na}} = 0.4$, with $f_n/f_p = -0.705$ and $\delta = 0.0$ keV. 60
5.9 Inelastic isospin-violating spin-independent DM fit to the experimental data in the σ_p^{SI}-M_{DM} plane with $f_n/f_p = -0.715$ and $\delta = 3.25$ keV. 62

5.10 Differential event rate for momentum-dependent DM scattering on sodium nuclei for DM mass $M_{DM} = 10$ GeV, and with arbirtrary normaliztion. The dashed blue, solid red, dot-dashed green, and dotted purple curves correspond to momentum-dependent scattering with $n = -1$, $n = 0$, $n = 1$, and $n = 2$, respectively. 63
5.11 Momentum-dependent inelastic isospin-violating spin-independent DM fit to the experimental data in the σ_p^{SI}-M_{DM} plane with $n = -1$, $f_n/f_p = -0.706$ and $\delta = 8.4$ keV. . 65
5.12 Momentum-dependent inelastic isospin-violating spin-independent DM fit to the experimental data in the σ_p^{SI}-M_{DM} plane with $n = 1$, $f_n/f_p = -0.808$ and $\delta = 4.0$ keV. . . 65
5.13 Momentum-dependent inelastic isospin-violating spin-independent DM fit to the experimental data in the σ_p^{SI}-M_{DM} plane with $n = 2$, $f_n/f_p = -0.730$ and $\delta = -2.8$ keV. . 66
5.14 Forms of the sodium (Na) and iodine (I) energy dependent quenching factors of this thesis in percent, as interpolated using the original results in Figure 9 of reference [56]. 67
5.15 Elastic isospin-violating spin-independent DM fit to the experimental data in the σ_p^{SI}-M_{DM} plane with $f_n/f_p = -0.686$, $\delta = 0.0$ keV and using the energy dependent quenching factors of Figure 5.14 for DAMA target material. 68
5.16 Expectations for XENON1T on elastic isospin-violating spin-independent DM. An IVDM fit to the positive-signal data is also plotted. The 2011 XENON100 constraint is shown in black, the 2012 XENON100 constraint is shown in red, and the projected 2017 XENON1T 90% CL is shown in blue. 69
5.17 Graphing the spin-dependent function $\xi^{SD}(a_n/a_p)$ of equation (5.4) for various target material and for DM mass $M_{DM} = 10$ GeV. 71
5.18 Elastic isospin-violating spin-dependent DM fit to the experimental data in the σ_p^{SD}-M_{DM} plane with $a_n/a_p = 2.93$ and $\delta = 0.0$ keV. 72
5.19 Inelastic isospin-violating spin-dependent DM fit to the experimental data in the σ_p^{SD}-M_{DM} plane with $a_n/a_p = 1.84$ and $\delta = -14.7$ keV. 73
5.20 Momentum-dependent inelastic isospin-violating spin-independent DM fit to the experimental data in the σ_p^{SD}-M_{DM} plane with $n = -1$, $a_n/a_p = 1.76$ and $\delta = -10.36$ keV. 74
5.21 Inelastic isospin-violating combined DM fit to the experimental data in the σ_p^{SI}-M_{DM} plane with $f_n/f_p = -0.712$, $a_n/a_p = 1.60$, $\sigma_p^{SD} = 4.63 \times 10^{-37}$ cm^2 and $\delta = -14.2$ keV. Fiducial values of v_{esc}, v_0, ρ_{DM}, and $Q_{\rm Na}$ are used. 75
5.22 Inelastic isospin-violating combined DM fit to the experimental data in the σ_p^{SI}-M_{DM} plane with $n = -1$, $f_n/f_p = -0.809$, $a_n/a_p = 1.72$, $\sigma_p^{SD} = 2.39 \times 10^{-38}$ cm^2 and $\delta = -8.56$ keV. Fiducial values of v_{esc}, v_0, ρ_{DM}, and $Q_{\rm Na}$ are used. 76

6.1 Plotting v_{min} as a function of E_{nr} for arbitrary nucleus mass, WIMP mass, and mass splitting $\delta > 0$. For a nuclear recoil energy range $[E_1, E_2]$, the corresponding range of minimum velocities $[u_{min}, u_{max}]$ is shown. The velocity v_{med} demonstrates how one value of v_{min} can arise from two values of E_{nr}. 82
6.2 Elastic isospin-conserving spin-independent halo-independent DM fit to the experimental data in $\tilde{\eta}$-v_{min} space with $M_{DM} = 8.7$ GeV, $f_n/f_p = 1.0$, and $\delta = 0.0$ keV. 87
6.3 Elastic isospin-violating spin-independent halo-independent DM fit to the experimental data in $\tilde{\eta}$-v_{min} space with $M_{DM} = 8.03$ GeV, $f_n/f_p = -0.708$, and $\delta = 0.0$ keV. . . . 88
6.4 Elastic isospin-conserving spin-independent halo-independent DM fit to the experimental data in $\tilde{\eta}$-v_{min} space for energy dependent DAMA quenching factors with $M_{DM} = 8.36$ GeV, $f_n/f_p = -0.686$, and $\delta = 0.0$ keV. 88

6.5 Inelastic isospin-violating spin-independent halo-independent DM fit to the experimental data in $\tilde{\eta}$-v_{min} space with $M_{DM} = 8.60$ GeV, $f_n/f_p = -0.715$, and $\delta = 3.25$ keV. . . 89
6.6 Momentum-dependent inelastic isospin-violating spin-independent halo-independent DM fit to the experimental data in $\tilde{\eta}$-v_{min} space with $n = -1$, $M_{DM} = 10.5$ GeV, $f_n/f_p = -0.706$, and $\delta = 8.4$ keV. 90
6.7 Momentum-dependent inelastic isospin-violating spin-independent halo-independent DM fit to the experimental data in $\tilde{\eta}$-v_{min} space with $n = 1$, $M_{DM} = 7.8$ GeV, $f_n/f_p = -0.808$, and $\delta = 4.0$ keV. 91
6.8 Momentum-dependent inelastic isospin-violating spin-independent halo-independent DM fit to the experimental data in $\tilde{\eta}$-v_{min} space with $n = 2$, $M_{DM} = 6.6$ GeV, $f_n/f_p = -0.730$, and $\delta = -2.8$ keV. 91
6.9 Elastic purely protonic spin-dependent halo-independent DM fit to the experimental data in $\tilde{\eta}$-v_{min} space with $M_{DM} = 8.0$ GeV, $a_n = 0.0$, $a_p = 1.0$, and $\delta = 0.0$ keV. . . . 93
6.10 Elastic purely neutronic spin-dependent halo-independent DM fit to the experimental data in $\tilde{\eta}$-v_{min} space with $M_{DM} = 8.0$ GeV, $a_n = 1.0$, $a_p = 0.0$, and $\delta = 0.0$ keV. . . . 93
6.11 Elastic isospin-violating spin-dependent halo-independent DM fit to the experimental data in $\tilde{\eta}$-v_{min} space with $M_{DM} = 8.74$ GeV, $a_n/a_p = 2.93$, and $\delta = 0.0$ keV. 95
6.12 Inelastic isospin-violating spin-dependent halo-independent DM fit to the experimental data in $\tilde{\eta}$-v_{min} space with $M_{DM} = 6.9$ GeV, $a_n/a_p = 1.84$, and $\delta = -14.7$ keV. 95

B.1 Exothermic inelastic isospin-violating spin-independent DM fit to the experimental data in the $\sigma_p^{SI} - M_{DM}$ plane for larger (negative) mass splitting with $f_n/f_p = -0.633$ and $\delta = -15.0$ keV. 102
B.2 Endothermic inelastic isospin-violating spin-independent DM fit to the experimental data in the $\sigma_p^{SI} - M_{DM}$ plane for larger mass splitting with $f_n/f_p = -0.748$ and $\delta = 15.0$ keV. 103
B.3 Inelastic isospin-violating spin-independent fit to the experimental data in the f_n/f_p-δ plane with $M_{DM} = 8.55$ GeV and $\sigma_p^{SI} = 2.90 \times 10^{-38}$ cm^2. 103

C.1 Momentum-dependent inelastic isospin-violating spin-dependent halo-independent DM fit to the experimental data in $\tilde{\eta} - v_{min}$ space with $n = -1$, $M_{DM} = 8.5$ GeV, $a_n/a_p = 1.76$, and $\delta = -10.36$ keV. 104
C.2 Momentum-dependent inelastic isospin-violating spin-dependent halo-independent DM fit to the experimental data in $\tilde{\eta} - v_{min}$ space with $n = 1$, $M_{DM} = 4.53$ GeV, $a_n/a_p = 1.31$, and $\delta = -39.4$ keV. 105

List of Tables

2.1 The total spin J, and nucleon spin matrix elements $\langle S_n \rangle$ and $\langle S_n \rangle$ for direct detection isotopes with odd spin. Quantities are taken from reference [30]. 16
2.2 Number of nucleons A_{ij} for isotope i of element type j and their fractional abundances β_{ij} in percent. Only isotopes with $\eta_{ij} \geq 1\%$ are presented. Values are taken from [26]. Any unspecified fractional abundances are assumed to have an averaged value of A corresponding to the standard atomic mass. 19

3.1 Energy bins, event rates, and uncertainties used to fit the DAMA modulated amplitude. The event rate displayed is an average taken over the exposure period. 24
3.2 Energy intervals, total number of events, and estimated background used to fit the CRESST-II unmodulated data. 26

5.1 Definitions for the objects of the parameter space plots including the colour scheme, and labels. The solid (dashed) lines correspond to the 95.4% (99.7%) CL. 48

Abbreviations

BBN	**B**ig **B**ang **N**ucleosynthesis
CMB	**C**osmic **M**icrowave **B**ackground
DM	**D**ark **M**atter
IC	**I**sospin-**C**onserving
IV	**I**sospin-**V**iolating
IVDM	**I**sospin-**V**iolating **D**ark **M**atter
MACHO	**MA**ssive **C**ompact **H**alo **O**bject
MSSM	**M**inimal **S**upersymmetric **S**tandard **M**odel
MD	**M**omentum-**D**ependent
NR	**N**on-**R**elativistic
ROI	**R**egion **O**f **I**nterest
SD	**S**pin-**D**ependent
SDSF	**S**pin-**D**ependent **S**tructure **F**unction
SI	**S**pin-**I**ndependent
SM	**S**tandard **M**odel
WIMP	**W**eakly **I**nteracting **M**assive **P**article

For Evelyn, Gilbert, and Marilyn

Chapter 1

Our Dark Universe

1.1 Introduction

For centuries, the motion of celestial bodies across the sky have provided physicists with a catalyst for understanding the fundamental laws of nature. From the discovery of Newton's inverse-square law of gravitation, to a confirmation of general relativity by observation of the precession of the perihelion of Mercury's orbit; from effectuating ideas that would develop into the big bang theory of cosmological evolution, to the motion of supernovae revealing the accerelated expansion of our Universe, extraterrestrial phenomena have driven our pursuit for knoweledge regarding the physical world. However, not all questions that arise from such astrophysical observations have led to simple answers, if any at all.

One of the first indications that the Universe might be partially made up of an invisible but gravitating matter component occurred in 1922. Attempts by James Hopwood Jeans to derive the total matter density in our Solar vicinty resulted in the conclusion that for every bright star, there must be two dark stars [1].[1] The contradiction between the masses of visible stars and the masses of the stellar systems they belonged to would be extended to the scale of galaxies within galaxy clusters. In 1933, by observing the dynamics of galaxies composing the Coma

[1] In early years, Jeans was not the only physicist to discover a non-luminous gravitating mass component. Between 1915 and 1932 calculations performed by Öpik [2], Kapteyn [3], and Oort [4] were able to show that the total local matter density in our Solar vicinity could be explained provided a reasonable extrapolation of invisible baryons.

cluster, Fritz Zwicky reasoned that within the cluster there must exist an electromagnetically neutral mass component for which he bestowed the illustrious title of "dunkle Materie", or in other words "dark matter" [5].[2]

Today there exists indisputable indirect evidence for *dark matter* (DM) through its gravitational signatures, which explain observations of the rotational velocity of stars in galaxies and galaxies in galactic clusters, as well as the gravitational lensing of objects at high redshift and the structure of the temperature and polarization anisotropies of the cosmic microwave background (see section 1.2 for more details). As one might surmise, the problem of DM holds some of the most important outstanding questions in both cosmology and particle physics. Despite there being a plethora of evidence asserting gravitational interactions of DM, the particle characteristic of DM continues to elude a definitive explanation.

Hitherto, there is nothing to preclude the possibility that non-gravitational couplings to particles of the *standard model* (SM) are intrinsic to the nature of DM. As a matter of fact, models in which DM particles are thermally produced require such interactions. Under scenarios of this kind, the creation of DM pairs via the annihilation of SM particles during the freezout epoch, along with the inverse process, is needed in order to produce the abundance of DM observed today. In a Universe where such interactions exist, the direct detection of DM via its scattering on SM particles would be essential for sharpening our understanding of the fundamental properties of dark matter. Over the past two decades, a multitude of experiments have set out to measure the recoil energy of DM scattering with nucleons, leading to increasingly stringent limits on the DM-nucleon cross section, and a few tentative signals that might be interpreted as detections of DM. However, based on our simplest assumptions regarding the nature of DM interactions, these findings along with those obtained from null experiments appear to be inconsistent. Attempts to build a DM model that yields compatible best-fit regions in the DM parameter space have proven unsuccessful, not to mention unable to satisfy constraints arising from null experiments.

Motivated by the work of recent studies, this thesis aims to provide an in-depth examination of a specific class of dark matter referred to as *isospin-violating dark matter* (IVDM) and its pertinence to current terrestial direct detection experiments. Resolving the issues surrounding

[2] For a brief review on the early history of dark matter see [6].

direct detection of DM requires a thorough exploration of the available phenomenological avenues and an emphasis on better quantifying the feasibility of various DM models.

In this chapter, a general introduction to the concepts and ideas relating to the DM paradigm is given. In section 1.2 we motivate the existence of DM with explanations of some prominent pieces of observational evidence. Following this, section 1.3 presents the various criteria that any viable DM candidate must satisfy in order to fulfill its gravitational roles. Also in this section, arguments are given in favour of weakly interacting massive particles as being the propitious DM candidate. Finally, section 1.4 outlines the direction of this thesis, and connects the information of this chapter to the subsequent subject matter.

1.2 Evidence for dark matter

There are a number of indirect pieces of evidence supporting the existence of dark matter. In this section, we present the most compelling examples in an attempt to reiterate the importance of dark matter in our Universe and why dark matter must exist.[3]

Rotation curves of spiral galaxies: Firstly, we examine the rotation curves of spiral galaxies as a presentation of support for the existence of DM on galactic scales. Spiral galaxies consist of a flat, rotating disk of visible stars and interstellar matter which for the most part are concentrated in one or more spiral arms. Measurements on the velocity distributions of visible matter within spiral galaxies have revealed that the rotation speed at the outer regions of the galaxies is faster than what is predicted from the laws of gravitation [8, 9]. In other words, the gravitational potential that is necessary for galaxies to rotate at the observed velocities must contain a considerably greater amount of mass than expected based on the amount of luminous matter observed therein.

Newtonian dynamics predicts that the speed of rotation v at a radius r from the center of the galaxy is given by

$$v(r) = \sqrt{\frac{GM(r)}{r}}, \tag{1.1}$$

[3]Alternatives to dark matter have been proposed, the most prominent being modified Newtonian dynamics or MOND [7]. MOND involves the introduction of a new large scale beyond which the gravitational potential takes a different form. Since deviations from the standard theory of gravity occur on multiple scales, to explain all observations within the MOND framework would be an arduous task.

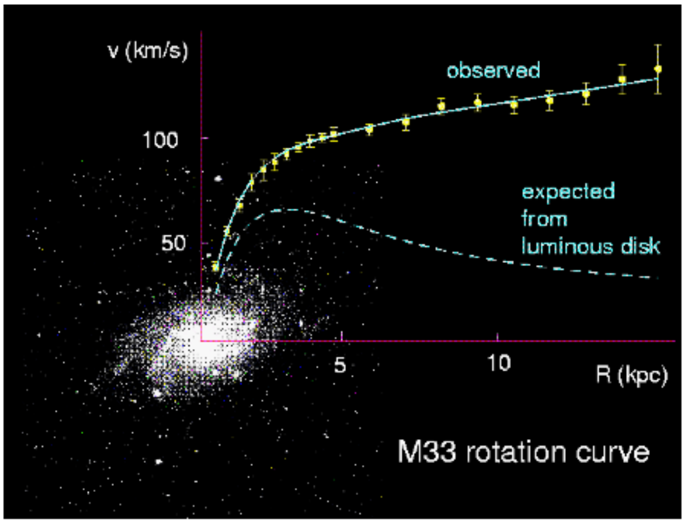

FIGURE 1.1: Data points for the velocity profile of spiral galaxy M33. Also shown, is the observed rotation curve, and the curve expected from the luminous disc. There is also a smaller contribution from galactic gas that is not shown. Figure taken from [10].

where $M(r)$ is the total mass in the galaxy enclosed within the radius r. Beyond the disc of visible matter, $M(r)$ should remain constant and $v(r)$ should decrease proportional to $1/\sqrt{r}$. However, observations indicate that past the optical disk, $v(r)$ is nearly constant meaning that $M(r)$ must scale like r, despite the absence of any luminous matter. To explain this observation, it requires to postulate an addition of an invisible halo of matter to the mass profiles of galaxies. This invisible halo of matter extends beyond the visible component and is generally attributed to DM. It is referred to as the *dark matter halo*. Figure 1.1 shows the rotation curve for the dwarf spiral galaxy M33 clearly demonstrating the discrepancy between prediction of the velocity profile based solely on visible matter, and observation.

Gravitational lensing: General relativity affirms the bending of light around massive objects. This generates a phenomenon known as gravitational lensing in which the light deflection field of a background source due to a mass concentration in the foreground, results in either a slight distortion of the source's shape (weak lensing), or in arcs called Einstein rings or several images of the source (strong lensing). Gravitational lensing provides an unmistakable way of determining the true mass density of a foreground object including any DM constituent, since larger concentrations of mass cause greater amounts of distortion in the image of a background source. As an example, in the galaxy cluster Abell 2218, an analysis of lensed arcs reveals a mass-to-light ratio which is 80 - 180 in units of the solar ratio [11].

Doppler peaks of the cosmic microwave background: The relic blackbody radiation of the hot Big Bang, last emitted from the surface of last scattering when photons decoupled from the photon-baryon plasma, is referred to as the *cosmic microwave background* (CMB). Observations of the temperature and polarization anisotropies in the CMB on the order of 10 μK and 0.1 μK respectively, have played a pivotal role in constructing and improving the standard ΛCDM model of cosmology. Based on a set of initial conditions along with assumptions regarding the background cosmology, it is possible to numerically compute the angular power spectrum of the CMB anisotropies. Therefore, precise experimental measurements can be used to set tight constraints on the cosmological parameters of the ΛCDM model including the mass density of non-baryonic matter in the Universe.

Precipitated by the competition between gravity and radiation pressure prior to photon decoupling, oscillations about the potential wells of small overdensities in the photon-baryon fluid would result in temperature fluctuations of the CMB at the surface of last scattering. The presence of dark matter in the photon-baryon fluid would have the effect of reducing the driving effect of the acoustic oscillations since DM would interact gravitationally but not electromagnetically. Hence, the CMB anisotropies give an excellent probe into the mass density of cold dark matter at the time of last scattering.

Multipole moments are used to analyze the temperature and polarization fluctuations. The resulting power spectrum in terms of multipole l exhibits a distinct pattern of Doppler peaks. Figure 1.2 shows the power spectrum of the temperature anisotopies corresponding to the nine-year analysis of the Wilkinson Microwave Anisotropy Probe (WMAP), along with SPT and ACT data [12]. The solid line represents the best fitting standard ΛCDM model of cosmology to the WMAP data alone. The results show an astounding agreement between experimental CMB measurements and the ΛCDM model. Most recently, the PLANCK collaboration used temperature power spectrum data to determine the densities of baryonic, cold dark matter, and dark energy in our Universe [13]. The 68% limits of these cosmological parameters were found to be, respectively:

$$\Omega_b h^2 = 0.02207 \pm 0.00033,\ \Omega_{CDM} h^2 = 0.1196 \pm 0.0031,\ \Omega_\Lambda = 0.686 \pm 0.020. \tag{1.2}$$

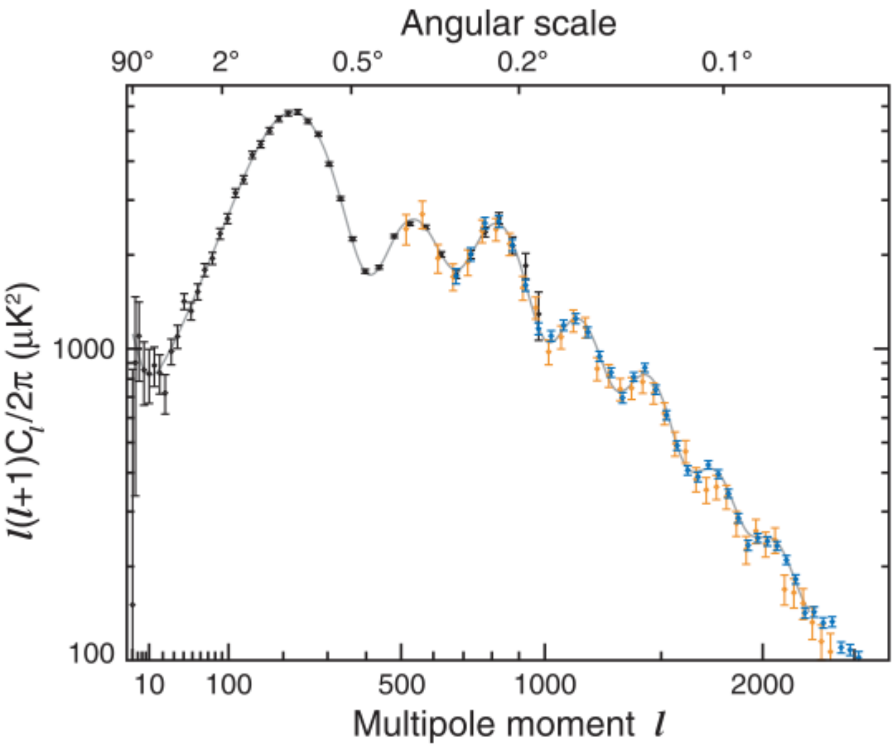

FIGURE 1.2: CMB measurements in the nine-year WMAP analysis. The WMAP data (black) is given, as well as the extended CMB data set which includes SPT data (blue) and ACT data (orange). The solid grey curve represents the best fitting ΛCDM model to the WMAP data alone. Figure taken from [12].

1.3 Criteria for dark matter candidates

For a DM particle candidate of the standard ΛCDM cosmological model to be considered viable, i.e. sucessfully demonstrate its gravitational signatures, it must first satisfy the following basic criteria. These criteria are placed under the assumption that a single DM species dominates the DM sector. For more details, see [14].

Relic abundance: If DM particles are created in the early Universe, they do so either by standard thermal interactions with the thermal bath, or via non-thermal processes. Regardless of the production mechanism, the underlying microphysical theory which encapsulates the DM's particle properties and the parameters of said theory, as well as the early Universe conditions must combine to reproduce the correct value of the relic density.

Arguably the most promising DM candidate (and that for which this dissertation focuses on), *weakly interacting massive particles* or WIMPs[4] form a class of particles which are an example

[4]What is the etymology behind the term WIMP? The following is an excerpt from a footnote appearing on page 310 of Kolb and Turner's textbook *The Early Universe*, and is perhaps a humorous reference to Steigman

of a thermal relic. Particles that exist in thermal equilibrium during the early Universe will, as the Universe cools down, have a number density which is Boltzmann suppressed, thus causing the likelihood of particle annihilations of this species to decrease. The particle will fall out of thermal equilibrium once the expansion rate of the universe surpasses the particle species' rate of creation and destruction. At this point, the particle decouples from the thermal bath becoming a thermal relic, the relic is said to "freeze out".

It is possible to show that an order of magnitude estimate of today's relic density for a generic thermally produced DM particle is given by[5]

$$\Omega_{CDM}h^2 \approx \frac{3 \times 10^{-26}\mathrm{cm}^3/\mathrm{s}}{\langle \sigma_{ann} v \rangle}, \tag{1.3}$$

where $\langle \sigma_{ann} v \rangle$ is the thermally averaged annihilation cross section times velocity. As a result, a successful theory of DM should predict an annihilation cross section which, in equation (1.3), yields a cold DM density consistent with the experimentally determined value of Ω_{CDM}.

Neutrality and collisionless nature: The electromagnetic properties and interaction strength of DM play a vital role in determining the feasibility of phenomenological models. Electromagnetic couplings of DM to SM photons must be considerably weaker than those of standard charged particles in order to circumvent bounds concerning relic density, DM halo shape, large scale structure, recombination-era coupling, and direct detection considerations [20]. In terms of ϵ, the fraction of elementary charge defining the electromagnetic interaction strength, these constraints set $\epsilon < 10^{-6}$ for standard DM with a mass of 1 GeV.

DM must be (at the very least) weakly interacting with both itself and neutral baryonic matter. The conjecture that DM is nearly collisionless is in part due to the morphology of DM halos however, astrophysical examples such as the Bullet cluster, and limits from direct terrestial searches underpin the collisionless nature of DM [21]. Currently, there exist a number of reported bounds on the ratio of the spin-independent self-interaction cross section and the DM

and Turner's 1984 paper [15] where the term reportedly first appeared: "WIMP© is a copyrighted trademark of the Chicago group, standing for Weakly Interacting Massive Particle."

[5]The more exact expression for the cold DM density is $\Omega_{CDM}h^2 \approx \frac{1.07\times10^9\mathrm{GeV}^{-1}}{M_{pl}}\frac{x_f}{g_{*f}}\frac{1}{(a+3b/x_f)}$, where M_{pl} is Planck's mass, g_{*f} counts the relativistic degrees of freedom, and $x_f = M_{DM}/T_f$. Here M_{DM} is the mass of the DM particle, T_f is the temperature at freeze out, and $\langle \sigma_{ann} v \rangle = a + b\langle v^2 \rangle + \mathcal{O}(\langle v^4 \rangle)$. Taking $x_f \sim 20$ produces the result of equation (1.3) [16].

mass, σ_{DM}^{SI}/M_{DM}. For instance, Markevitch *et* al. place a limit on this ratio of $\sigma_{DM}^{SI}/M_{DM} < 0.7$ cm^{2}g^{-1} [22].

Cold dark matter: In order for the "bottom-up" hierarchy of large-scale structure formation in the Universe to remain unaltered by DM density perturbations, the "temperature" of Dark matter must be inherently *cold*, that is to say, we require the dominant DM species to be non-relativistic in nature. To be more complete, consider the following. As the Universe entered the matter-dominated epoch, DM density perturbations drove the oscillations of the baryon-photon fluid eventually causing a decoupling of the baryons. Once decoupled, the baryons became trapped in existing DM potential wells forming small scale structures. However, the growth of baryon density fluctuations would continue, ultimately leading to the large scale structures we observe today.

If a collisionless DM species were relativistic (hot) during structure formation, then small scale density perturbations would have been carried away by free streaming of the DM. In this case, one is left with structures on the scale of the free streaming length, which is large for relativistic particles. As a result, in order to obtain small scale structures, the splintering of large scale structures into smaller ones would have to have occurred — a contradiction to current observation since it is known that galaxies are older than superclusters. Not suprisingly, for this reason neutrinos are ruled out as the dominate DM component.

Dark matter is non-baryonic: Evidence derived from *big bang nucleosynthesis* (BBN) and CMB considerations suggests a non-baryonic picture of DM. The primordial abundances of light elements are highly dependent upon the baryon-to-photon ratio. Suppose we fix the photon density and consider a Universe made up predominately of baryonic DM. A larger baryon density would result in a faster rate of fusion to ^{4}He meaning fewer "spare" nucleons for the formation of lighter elements such as ^{2}H and ^{3}He. Measurements of the CMB temperature have set the photon density thus allowing for excellent measurements of ordinary matter abundances using light element ratios. To obtain the correct abundances, DM must be non-baryonic.

Faint neutron stars, brown dwarfs, white dwarfs, planets, etc. . . , collectively referred to as *massive compact halo objects* or MACHOs, provide examples of baryonic dark matter. However, due to constraints arising from observed chemical abundances and searches for microlensing by MACHOs, MACHOs are ruled out as the primary DM candidate.

Stability over cosmological lifetimes: DM particles must be stable over cosmological timescales. Models which involve decaying DM are tightly constrained by cosmological analyses of the CMB, Type Ia supernova, Lyman-α forest, galaxy clustering and weak lensing observations. Furthermore, a stable DM particle is necessary so that the fraction of DM decays occuring during or immediately after BBN is inconsequential to the predictions of BBN [18]. Reference [23] sets limits on the lifetime for the decay of DM into W^+W^- and $b\bar{b}$ both around $\tau_{DM} \gtrsim 10^{27}$s for masses at the multi-GeV scale.

1.3.1 The WIMP miracle

The coincidence of scales that occurs between the relic abundance of DM and strength of the weak force interaction is known as the *WIMP miracle*. Dimensional analysis tells us that the annihilation cross section of a WIMP goes like

$$\langle \sigma v \rangle \approx \frac{g_w^4}{16\pi^2 M_{DM}^2}, \tag{1.4}$$

where g_w is some weak-scale effective coupling between WIMPs and SM particles, and provided that M_{DM} is the dominating scale. Interestingly, since WIMPs are an example of thermal relics, and for WIMP masses on the order of 100 - 1000 GeV, it is possible to obtain an annihilation cross section which is compatible with observations of Ω_{CDM} by substituting the above expression into equation (1.3) for reasonable values of g_w. It is this naturalness for WIMPs to produce the correct relic abundance that garners the term WIMP miracle. It should also be mentioned, that WIMPs receive the adulation of phyisicists because strong candidates are known to appear in supersymmetric extensions of the SM and in string theory.

Given the strong support for WIMPs as dark matter candidates and assuming that DM couplings to SM particles remain tenable, henceforth we assume that WIMPs act as the primary source for any unaccountable signals at direct detection experiments.

1.4 Outline

By now the reader should be convinced of the following two statements:

- on the basis of gravitational observations, there is clear and compelling evidence which asserts the existence of DM in our Universe and its role as a fundamental feature of cosmology and particle physics,
- DM particles known as WIMPs, under the conditions that they be collisonless, non-relativistic and stable, provide physicists with a natural dark particle candidate in which to test theoretical models of DM against the observations of direct detection experiments.

As previously mentioned, the direct detection of WIMPs via scattering with SM nucleons is an essential next step in understanding the DM sector and refining current theories and predictions of DM models. Thus far, direct detection experiments which have claimed an excess signal compatible with a DM interpretation of the data appear to be in contradiction with each other, not to mention strenuously constrained by the results of null experiments.

In recent years, so-called isospin-violating dark matter has been shown to yield an overall more consistent picture in the findings of experimental DM searches. IVDM refers to DM species in which the couplings between DM and neutrons is allowed to differ from that between DM and protons. *A priori*, there is no reason why WIMPs should couple equally to protons and neutrons hence, IVDM is a well-motivated construct. In this thesis we investigate whether or not IVDM models are capable of alleviating the tensions posed by positive signal experiments while simultaneosly circumventing bounds set by null ones. The theoretical frameworks of *spin-independent* (SI) and *spin-dependent* (SD) DM are analysed, along with inelastic and *momentum-dependent* (MD) extensions of the IVDM model. In a scenario which we refer to here as *combined* DM, the possibility of a DM differential event rate which preserves both the SI and SD components is explored under completely generalized couplings. Moreover, we examine the effect of an energy-dependent sodium quenching factor Q_{Na} for fitting the DAMA observations, and give an IV interpretation of predicted XENON1T results.

Our analysis of IVDM is presented in the way of two distinct formalisms. First, the standard formalism which assesses the compatibility of direct detection data via a series of DM parameter space plots. This method assumes a particular velocity distribution of DM in the Galactic halo in order to make theoretical predictions on the DM differential event rate. Second, the halo-independent formalism which investigates experimental data in the space of minimum velocities required for a dark matter particle to scatter off a given nucleus. The halo-independent formalism makes almost no assumptions regarding the DM velocity distribution.

The subsequent topics of this thesis are outlined as follows. In Chapter 2, the theory of dark matter scattering is presented focusing on differential event rates and the calculation of the total number of DM events for the theoretical models considered herein. The DM model parameters are introduced and given brief explanations. Chapter 3 focuses on the direct detection experiments relevant to this analysis. Detailed descriptions of the experiments are given including: methods of data acquisition, experimental results, outstanding criticisms, and the methodology used to compute confidence intervals and upper limits in DM parameter space. Afterwards, a phenomenological review of past and current results for IVDM is laid out in Chapter 4, with an emphasis on the evolution of experimental and theoretical findings. In Chapter 5, the results of the standard formalism are presented. Following this, Chapter 6 provides the reader with a halo-independent analysis of the experimental data. Finally, in Chapter 7, conclusions of this research are drawn, and we discuss the future outlook for IVDM.

Chapter 2

Theoretical Aspects of Dark Matter Scattering

A review of the theoretical framework for calculating both the SI and SD DM differential event rate and the total number of events expected in a given detector is provided in this chapter. The various parameters of the DM model are introduced and given brief explanations. Furthermore, a description of the standard halo model is given, which will complete the theory necessary to carry out computations within the standard formalism of DM direct detection analysis.

2.1 Differential event rates

In general, the differential event rate or energy spectrum for the scattering of a DM particle of mass M_{DM} with a nucleus of mass M_A is written as (see [24]):

$$\frac{dR}{dE_{nr}} = N_T \frac{\rho_{DM}}{M_{DM}} \int_{v_{min}}^{\infty} \mathrm{d}^3 v \frac{d\sigma}{dE_{nr}} v f(\vec{v} + \vec{v_e}), \tag{2.1}$$

where N_T is the number of target nuclei per kilogram of the detector, ρ_{DM} is the Galactic DM density, $\vec{v}$ and $\vec{v_e}$ are the velocity of the dark matter and Earth relative the Sun, respectively with $v \equiv |\vec{v}|$, $d\sigma/dE_{nr}$ is the DM-nucleus differential cross section, and $f(\vec{v}+\vec{v_e})$ is the local DM velocity distribution in the detector rest frame. For an event with nuclear recoil energy E_{nr}, the incoming DM particle must have a minumum velocity v_{min} given by

$$v_{min} = \sqrt{\frac{1}{2M_A E_{nr}}}\left(\frac{M_A E_{nr}}{\mu_A} + \delta\right), \tag{2.2}$$

where μ_A is the DM-nucleus reduced mass, and δ is the mass splitting (mass difference) in keV between the incoming and outgoing DM particles. We consider $\delta = \mathcal{O}(\text{keV})$ since DM kinetic energies relevant to direct detection experiments are on this scale. If $\delta = 0$, then the DM particle will scatter elastically otherwise, the DM contains inelastic couplings which are either exothermic ($\delta < 0$) or endothermic ($\delta > 0$).

The differential cross section for DM-nucleus scattering can be separated into a scalar spin-independent and an axial-vector spin-dependent component [25]:

$$\frac{d\sigma}{dE_{nr}}(E_{nr}) = \left(\frac{d\sigma}{dE_{nr}}\right)_{SI} + \left(\frac{d\sigma}{dE_{nr}}\right)_{SD}. \tag{2.3}$$

The components of the DM differential cross section can be written as:

$$\left(\frac{d\sigma}{dE_{nr}}\right)_{SI} = \frac{M_A \sigma_0^{SI}}{2\mu_A^2 v^2} F_{SI}^2(E_{nr}) \tag{2.4}$$

$$\left(\frac{d\sigma}{dE_{nr}}\right)_{SD} = \frac{M_A \sigma_0^{SD}}{2\mu_A^2 v^2} F_{SD}^2(E_{nr}), \tag{2.5}$$

where $\sigma_0^{SI(SD)}$ is the SI (SD) DM-nucleus cross section at zero-momentum transfer and in the elastic limit, and $F_{SI(SD)}(E_{nr})$ is the SI (SD) nuclear form factor for nucleus with atomic number Z and atomic mass number A.

2.1.1 Spin-independent differential cross section

For SI scattering, it is known that the DM-nucleus cross section at zero-momentum transfer takes the form

$$\sigma_0^{SI} = \frac{\mu_A^2}{\pi}\Big[f_p Z + f_n(A - Z)\Big]^2, \tag{2.6}$$

where f_n and f_p parameterize the relative dark matter coupling to neutrons and protons, respectively. Equation (2.6) can be written in terms of the SI DM-proton cross section σ_p^{SI}, using the fact that

$$\sigma_p^{SI} = \frac{\mu_p^2}{\pi} f_p^2, \tag{2.7}$$

where μ_p is the DM-proton reduced mass. Combining the above results and inserting them into equation (2.4), one obtains the following expression for the SI DM differential event rate:

$$\left(\frac{d\sigma}{dE_{nr}}\right)_{SI} = \frac{1}{2v^2}\frac{M_A \sigma_p^{SI}}{\mu_p^2}\left[\left(Z + \frac{f_n}{f_p}(A-Z)\right)\right]^2 F_{SI}^2(E_{nr}). \tag{2.8}$$

We identify the ratio of the DM-nucleon couplings f_n/f_p as the *SI isospin violation ratio*. Our SI DM model will be *isospin-conserving* (IC) if $f_n/f_p = 1$, and isopin-violating otherwise.

As it turns out, equation (2.4) makes the implicit assumption that the SI nuclear form factors for neutrons ($F_{SI}^n(E_{nr})$) and protons ($F_{SI}^p(E_{nr})$) are identical, that is to say $F_{SI}(E_{nr}) \equiv F_{SI}^n(E_{nr}) = F_{SI}^p(E_{nr})$. Indeed, in reality these form factors can be different. However, the dependence of the differential cross section on differences in these terms is sub-dominant next to possible variations of the ratio f_n/f_p [26]. As a result, we assume these form factors to be equivalent and refer to them both as $F_{SI}(E_{nr})$. $F_{SI}(E_{nr})$ reflects the loss of coherence with increasing momentum transfer. For our purposes, we use the Lewin-Smith parametrization of the Helm form factor [24]:

$$F_{SI}^2(E_{nr}) = \left(\frac{3j_1(qR)}{qR}\right)^2 \exp\left(-q^2 s^2\right), \tag{2.9}$$

where $q = \sqrt{2M_A E_{nr}}$ is the momentum transfer, and j_1 is the spherical Bessel function. R and s are parameters that describe the form and size of the nucleus [27]. In this work, $R = \sqrt{c^2 + \frac{7}{3}\pi^2 a^2 - 5s^2}$, $c = (1.23A^{1/3} - 0.60)$ fm, $a = 0.52$ fm, and $s = 0.9$ fm.

2.1.2 Spin-dependent differential cross section

Turning to the SD scenario, the general form of the SD DM-nucleus cross section at zero-momentum transfer is given by [28]:

$$\sigma_0^{SD} = \frac{32G_f^2\mu_A^2}{\pi}\frac{J+1}{J}\left[a_p\langle S_p\rangle + a_n\langle S_n\rangle\right]^2, \tag{2.10}$$

where G_F is Fermi's constant, J is the total spin of the nucleus with atomic number Z and atomic mass number A, $\langle S_p \rangle$ and $\langle S_n \rangle$ are the proton and neutron spin matrix elements for the scattered nucleus, and a_n and a_p are the DM couplings to the matrix elements of the axial-vector currents in neutrons and protons, respectively. Similar to the SI case, it is possible to write equation (2.10) in terms of the SD DM-proton cross section for a proton whose spin and total angular momentum take the same value ($J = S = \pm 1/2$):

$$\sigma_p^{SD} = \frac{24 G_F^2 \mu_p^2}{\pi} a_p^2. \tag{2.11}$$

However, given the complex relationship between the DM-nucleon couplings a_n and a_p, it is important to realise that equation (2.11) represents the true SD DM-proton cross only in the case where $a_n = 0$ and $a_p = 1$. For more general values of the SD DM-nucleon couplings, it remains that the SD DM-proton cross section defined by equation (2.11) is a useful measure by which upper limits in the SD parameter space may be set, and we employ this parameter accordingly.

Unlike the SI nuclear form factor, it is not possible to decouple the SD form factor from the DM-nucleon couplings. The SD nuclear form factor is written in terms of the so-called *spin-dependent structure functions* (SDSFs): $S_{00}(E_{nr})$, $S_{01}(E_{nr})$, $S_{11}(E_{nr})$, and the isoscalar ($a_0 = a_p + a_n$) and isovector ($a_1 = a_p - a_n$) couplings as follows:

$$F_{SD}^2(E_{nr}) = S(E_{nr})/S(0), \tag{2.12}$$

where

$$S(E_{nr}) = a_0^2 S_{00}(E_{nr}) + a_0 a_1 S_{01}(E_{nr}) + a_1^2 S_{11}(E_{nr}), \tag{2.13}$$

and

$$S(0) = \frac{2J+1}{\pi} \frac{J+1}{J} \left[a_p \langle S_p \rangle + a_n \langle S_n \rangle \right]^2. \tag{2.14}$$

The SDSFs depend on the nucleus under consideration, and are calculated theoretically using nuclear physics models. For the nucleons examined in the present analysis whose isotopes carry spin, we implement the SDSFs as given by Bednyakov and Šimkovicin in reference [29].

With the previous results at hand, the SD differential cross section may be worked into the

Isotope	J	$\langle S_n \rangle$	$\langle S_p \rangle$
^{19}F	1/2	0.441	-0.109
^{23}Na	3/2	0.248	0.020
^{29}Si	1/2	-0.002	0.130
^{73}Ge	9/2	0.030	0.378
^{127}I	5/2	0.309	0.075
^{129}Xe	1/2	0.010	0.329
^{131}Xe	3/2	-0.009	-0.272

TABLE 2.1: The total spin J, and nucleon spin matrix elements $\langle S_n \rangle$ and $\langle S_n \rangle$ for direct detection isotopes with odd spin. Quantities are taken from reference [30].

following form:

$$\left(\frac{d\sigma}{dE_{nr}}\right)_{SD} = \frac{2}{3v^2}\frac{\pi M_A \sigma_p^{SD}}{\mu_p^2(2J+1)}\left[S_{00}+S_{01}+S_{11}+2(a_n/a_p)(S_{00}-S_{11})+(a_n/a_p)^2(S_{00}-S_{01}+S_{11})\right], \tag{2.15}$$

where we identify the couplings ratio a_n/a_p as the *SD isospin violation ratio*. Finally, the values of J, $\langle S_n \rangle$, and $\langle S_n \rangle$ for the nuclides considered in our analysis are summarized in Table 2.1.

For the remainder of this chapter, we concentrate on the SI model of DM scattering however, the following results can be easily generalized to the SD model, or the combined DM model using findings of the previous sections.

2.1.3 Momentum-dependent scattering

Next, it is possible to allow for momentum-dependent scattering by rescaling the differential cross section as follows:

$$\frac{d\sigma}{dE_{nr}} \rightarrow \left(\frac{q^2}{q_{ref}^2}\right)^n \frac{d\sigma}{dE_{nr}}, \tag{2.16}$$

where $q_{ref} = 100$ MeV, and $n = -1, 0, 1, 2$ models are considered. Scattering in direct detection is *non-relativistic* (NR) since incoming DM velocities are $\sim 10^{-3}c$. As a result, the kinetic energy of incident DM and recoil energy are around 10 keV. For direct detection experiments probing this low energy scale, different microscopic models or field theory operators describing the DM-nucleus scattering lead to the same simple NR effective theory [31]. In such a case, it is possible to describe the interaction using a NR effective potential with velocity-dependent or MD expansion parameters. Focusing on the MD scenario, the expansion parameter is given by

q/q_{ref} where $q = |\mathbf{q}|$ is the momentum transfer and q_{ref} is some large scale involved. The index n in equation (2.16) parameterizes the various microscopic situations, such as the exchange of a light mediator, the presence of a resonance, etc...

Combining equations (2.1), (2.8), and (2.16), the differential event rate becomes

$$\frac{dR}{dE_{nr}} = \left(\frac{q^2}{q_{ref}^2}\right)^n \frac{N_T \rho_{DM} M_A \sigma_p}{2 M_{DM} \mu_{ne}^2} \left(Z + \frac{f_n}{f_p}(A - Z)\right)^2 F_{SI}^2(E_{nr}) \eta(E_{nr}), \tag{2.17}$$

where we have defined $\eta(E_{nr})$ to be the integral over the allowed velocities, that is

$$\eta(E_{nr}) = \int_{v_{min}}^{\infty} \mathrm{d}^3 v \frac{f(\vec{v} + \vec{v_e})}{v}. \tag{2.18}$$

2.1.4 Detector isotopes

For a DM model consisting of IV couplings, the differential event rate will depend on the number of neutrons and protons in the scattering nuclei. As a result, it is crucial to include the possibility of multiple isotopes in a given detector. Furthermore, we must also consider whether a detector is composed of different element types. Let β_{ij} be the fractional abundance of isotope i corresponding to a detector element j. In this case, the differential event rate becomes a sum over i and j, and can be written as [26]:

$$\frac{dR}{dE_{nr}} = \sum_{i,j} \beta_{ij} \left(\frac{q_{ij}^2}{q_{ref}^2}\right)^n \frac{N_{T_j} \rho_{DMi} M_{A_{ij}} \sigma_p}{2 M_{DM} \mu_{ne}^2} \left(Z_j + \frac{f_n}{f_p}(A_{ij} - Z_j)\right)^2 F_{SI_{ij}}^2(E_{nr}) \eta(E_{nr}), \tag{2.19}$$

where the values of A_{ij} (the number of nucleons in isotope i of element type j) used in this paper, along with their corresponding fractional abundances, β_{ij}, are listed in Table 2.2.

Under the assumption that the DM-nucleon couplings be IC and taking into account the possibility of different isotopes, the DM-nucleus cross section becomes $\sigma_0 = \sum_{i,j} \kappa_j \eta_{ij} \frac{\mu_{A_{ij}}^2}{\pi} A_{ij}^2$, where $\kappa_j \equiv N_{T_j} / \sum_j N_{T_j}$ for the target material being considered. Here, it requires that we assume variations in the nuclear form factor with respect to element and isotope type are small. Thus using this result and equation (2.7) it is possible to define a cross section σ_p^{IC}, which is related to the true DM-nucleus cross section by (see reference [32]):

$$\sigma_p^{IC} \sum_{i,j} \kappa_j \eta_{ij} \frac{\mu_{A_{ij}}^2}{\pi} A_{ij}^2 \equiv \sigma_0^{SI}. \tag{2.20}$$

Therefore, inserting the generalized version of equation (2.6) into the previous result, it is possible to express the true DM-nucleon cross section in terms of the isospin invariant cross section. We have

$$\sigma_p^{SI} = \xi(f_n/f_p)\sigma_p^{IC}, \tag{2.21}$$

where the function $\xi(f_n/f_p)$ is given by

$$\xi(f_n/f_p) = \frac{\sum_{ij} \kappa_j \eta_{i,j} \mu_{A_{ij}}^2 A_{i,j}^2}{\sum_{i,j} \kappa_j \eta_{ij} \mu_{A_{ij}}^2 [Z_j + (A_{ij} - Z_j) f_n/f_p]^2}. \tag{2.22}$$

As it so happens, for a given target material there exists a value of f_n/f_p which maximizes the function $\xi(f_n/f_p)$ [32]. The result for elastic momentum-independent scattering is:

$$(f_n/f_p)_{critical} = -\frac{\sum_{i,j} \kappa_j \eta_{ij} \mu_{A_{ij}}^2 (A_{ij} - Z_j) Z_j}{\sum_{i,j} \kappa_j \eta_{ij} \mu_{A_{ij}}^2 (A_{ij} - Z_j)^2}. \tag{2.23}$$

Thus equation (2.23) determines the value of f_n/f_p which maximizes the true cross section σ_p^{SI} relative the IC one. In the case of Xe detectors and assuming a single isotope, the true cross section is maximized for $f_n/f_p = -0.70$, and consequently, this is the isospin violation ratio which yields the weakest bounds for xenon based detectors relative those published under an IC scenario.

Another useful property of the relationship expressed in equation (2.21) is that it allows us to determine bounds on IVDM from published bounds on standard IC DM through a simple rescaling. Although disadvantages to this “rescaling method” do exist,[1] it will allow us to compare predicted bounds on DM parameters from future experiments in the IV scenario.

[1]It is not possible to introduce inelastic or momentum-dependent couplings into a rescaling method analysis. Furthermore, astrophysical parameters such as the Galactic escape velocity are restricted to what value is used in the calculation of the bound that is being rescaled, and it does not take into account variations in the nuclear form factor for different isotopes.

Xe	Ge	Si	Ca	W	C
128 (1.9)	70 (21)	28 (92)	40 (97)	182 (27)	12 (99)
129 (26)	72 (28)	29 (4.7)	44 (2.1)	183 (14)	13 (1.1)
130 (4.1)	73 (7.7)	30 (3.1)		184 (31)	
131 (21)	74 (36)			186 (28)	
132 (27)	76 (7.4)				
134 (10)					
136 (8.9)					

TABLE 2.2: Number of nucleons A_{ij} for isotope i of element type j and their fractional abundances β_{ij} in percent. Only isotopes with $\eta_{ij} \geq 1\%$ are presented. Values are taken from [26]. Any unspecified fractional abundances are assumed to have an averaged value of A corresponding to the standard atomic mass.

2.2 Total number of DM events

The theoretical number of dark matter events expected in a given detector can be calculated by integrating equation (2.19) over the recoil energy range of interest. In general, the energy that is measured by the detector E' (in many circumstances denoted by E_{ee} in units of keV electron recoil equivalent or keVee) differs from the true nuclear recoil energy E_{nr} (with units referred to as keVnr) through a quenching factor, $E' = E_{nr}Q(E_{nr})$. As a result, there is ususally an energy response function associated with each specific detector, represented here as $A(E_{nr}, E')$, which incorporates both the quenching factor and energy resolution of the detector. Furthermore, experiments will contain an efficiency or cut acceptance as a function of E', which is commonly called $\epsilon(E')$. In experiments that measure photoelectrons, there will be an analogous situation relating the true nuclear recoil energy to the number of measured photoelectrons.

As a result, the number of DM events $\mathcal{N}$ expected in a specific energy range E'_1 to E'_2 is found to be

$$\mathcal{N} = \mathcal{E} \int_{E'_1}^{E'_2} \mathrm{d}E' \epsilon(E') \int \mathrm{d}E_{nr} A(E_{nr}, E') \frac{dR}{dE_{nr}}, \tag{2.24}$$

where $\mathcal{E}$ is the exposure of the detector in units of kg·days. The exact prescription for converting the quantity that is measured to the nuclear recoil energy varies between experiments. In Chapter 3 we outline these specific methods in detail.

2.3 DM halo velocity distribution

In this section, we discuss the form of the DM halo velocity distribution $f(\vec{v})$, and solutions to the velocity integral $\eta(E_{nr})$ of equation (2.18). In the simplest case, a Maxwell-Boltzmann velocity distribution in the Galactic frame is assumed which produces an isotropic and isothermal sphere for the distribution of DM within the halo. Such a model is referred to a the *standard halo model* (SHM). The corresponding velocity distribution is given by

$$f(\vec{v}) = \begin{cases} \frac{1}{N}\big(\exp\left(-v^2/v_0^2\right) - \exp\left(-v_{esc}^2/v_0^2\right)\big) & \text{if } v < v_{esc} \\ 0 & \text{if } v > v_{esc} \end{cases}, \tag{2.25}$$

where N is an overall normalization constant, $v_0 = (220 \pm 20)$ km/s is the local circular velocity, and v_{esc} is the Galactic escape velocity with a median likelihood of $v_{esc} = 544^{+64}_{-46}$ km/s [33]. The second term in equation (2.25) is manually inserted so as to ensure that the distribution function approaches zero smoothly as the velocity approaches the Galactic escape velocity.[2]

Given that we are interested in the distribution of velocities relative to Earth, the velocity that enters equation (2.25) is $\vec{v} + \vec{v_e}$. The Earth's speed as a function of time t in years is known to be

$$v_e = |\vec{v_e}| = v_0(1.05 + 0.07\cos\left(\frac{2\pi(t - t_{peak})}{1\text{yr}}\right), \tag{2.26}$$

where t_{peak} = June 2nd ± 3 days [34]. With the information provided, it is possible to compute exact solutions to the velocity integral of $\eta(E_{nr})$ as a function of nuclear recoil energy E_{nr}. See Appendix A for complete results.

The structure of DM in our Galaxy has been studied extensively using high-resolution N-body simulations [35–37]. The results paint a picture of the DM velocity distribution which is different from the SHM. Moreover, such simulations have shown large deviations from the SHM in cases where the DM is allowed to scatter inelastically [38–42].

Not suprisingly, a number of alternative models to the distribution function of DM in the Galactic halo have been proposed including: Tsallis model [39, 42], double-power law profiles [43], Navarro-Frenk-White (NFW) model [44], triaxial halo model [40, 41, 45], and Via

[2]It should be noted that not all analyses of DM differential event rates include a truncation of the velocity distribution at the Galactic escape speed. The solutions to $\eta(E_{nr})$ presented in Appendix A include a parameter which makes it possible to turn off the truncating term.

Lactea II halo model [35, 46, 47]. The various descriptions of the DM halo can be divided into two groups: isotropic and anisotropic models. The first three models are examples of isotropic scenarios and involve velocity distributions where $f(v)$ only depends on the magnitude of the velocity $|\vec{v}|$. The remaining two models are examples of anisotropic halo profiles in which the defining characteristic of a preferred direction for DM velocities at the position of the Earth is contained in an anisotropy parameter. The radially biased orbits which arise in numerical situations inspire these anisotropic models.

With such a wide array of models attempting to describe the distribution of DM in the Galactic halo, it would be extremely difficult to adequately incorporate the large number astrophysical uncertainties associated within the standard DM analysis. Thus a framework which is independent of assumptions made on the halo distribution is well-motivated, and we present the theory for such a formalism in Chapter 6.

Chapter 3

Direct Detection Experiments

As mentioned in the introduction, there exist a number of ground-based direct searches using sensitive, low-background particle detectors which aim to measure the recoil energy deposited by interacting DM particles. In the following chapter, we review the various direct detection experiments that are considered in our analysis of IVDM. More specifically, for each experiment we discuss the technique for measuring WIMP recoil energies, experimental results, outstanding criticisms, and the method that we employ in order to compute confidence intervals/levels for fitting DM models.

3.1 CoGeNT

The CoGeNT experiment aims to detect DM-nucleon scattering events in a low-background set-up at the Soudan Underground Laboratory. CoGeNT operates p-type point contact germanium detectors that sense only ionization charge from nuclear recoils [48]. The background achieved below 3 keVee (i.e. ionization energy) is one of the lowest reported by any DM detector. Recent data confirms an exponentially distributed excess of events in the 0.5 – 1.5 keVee energy interval which cannot be accounted for by any known background [49].

The CoGeNT collaboration also reports a modulating signal in the 0.5 – 3.0 keVee energy range. This result has come under scrutiny. A time-series analysis of the CoGeNT time-stamped data in reference [50] reveals that in the low energy region, the presence of an annual modulation signature can only be confirmed in the energy interval 1.6 – 3.0 keVee. As for the 0.5 – 1.6 keVee energy region, no statistically significant annual modulation is observed despite having tested a variety of procedures to remove the cosmogenic background. Furthermore, it is shown that the yearly modulation attains its peak earlier than that predicted from WIMP recoils, making a DM interpretation of the signal difficult. Since reference [50], CoGeNT has updated the fraction of events passing the pulsar cut which are misidentified surface events, showing that it is in fact larger than originally stated. As a result, the significance of a modulating signal against background noise will be further reduced, and it is for these reasons that we focus our analysis on the unmodulated component of the CoGeNT data.

To fit the unmodulated contribution, we perform a 0.05 keVee binning of the publically available data [51] in the energy range 0.5 - 3.0 keVee. The binned data is reweighted using the detector efficiency $f_{eff}(E)$ found in reference [49] and the fraction of events due to surface event contamination is removed using the correction factor $f_{surf}(E) = (1 - \exp(-1.21E/\text{keVee}))$. In the region of interest, cosmogenic L-shell electron capture events dominate the known background and can be modeled as a sum of decaying Gaussians [51, 52]. The total number of L-shell events expected in the detector are calculated using measurements of higher energy K-shell peak captures, as well as the ratio between L-shell and K-shell decays. The required parameters are found in the public release of CoGeNT data. Following Appendix A of [52], the cosmogenic background contribution in each bin can be calculated and subtracted from the binned data.

Since light DM models attempting to describe low energy signals predict essentially no events at higher recoil energies, a constant background of 2.565 cpd/kg/keVee is subtracted from the CoGeNT event spectrum. This background is simply the average event rate between 2 keVee and 3 keVee after cosmogenic background subtraction and efficiency corrections. Finally, the errors in each bin are computed by combining statistical errors on the raw binned CoGeNT event data, and the error associated with the number of atoms to decay via K-shell electron capture.

A χ^2 is constructed by fitting the theoretical event rate in each bin, R_i:

$$\chi^2 = \sum_{i=1}^{50} \left(\frac{R_i - \text{data}_i}{\delta \text{data}_i} \right)^2, \tag{3.1}$$

Bin (keVee)	Rate ($\text{cpd}^{-1}\text{kg}^{-1}\text{keVee}^{-1}$)	σ_{Rate}
2 – 2.5	0.016	0.004
2.5 – 3	0.026	0.005
3 – 3.5	0.022	0.005
3.5 – 4	0.008	0.005
4 – 4.5	0.011	0.004
4.5 – 5	0.005	0.004
5 – 5.5	0.009	0.003
5.5 – 6	0.004	0.003
6 – 14	0.000	0.000

Table 3.1: Energy bins, event rates, and uncertainties used to fit the DAMA modulated amplitude. The event rate displayed is an average taken over the exposure period.

where data_i and δdata_i are the experimental rate and uncertainty, respectively. CoGeNT also reports a quenching factor parametrized by $E_{ee}/\text{keVee} = Q(E_{nr}/\text{keVnr})^p$ with $Q = 0.2$ and $p = 1.12$, which relates the observed ionization energy to the true nuclear recoil energy.

3.2 DAMA

The DAMA collaboration has operated two detection experiements, DAMA/LIBRA [53] and the former DAMA/NaI [54], at the Gran Sasso National Laboratory in a suitable low-background set-up placed deep underground over the past decade and a half. Both projects strive to perform a direct detection of DM particles in the Galactic DM halo through the model independent annual modulation signature. DAMA uses highly radiopure NaI[Tl] scintillators as target matter which measure the fraction of energy that scattering DM particles deposit as scintillation.

The combined results of DAMA/NaI and DAMA/LIBRA support the presence of DM particles in the Galactic halo at 8.2σ CL [53]. The evidence is predominant in the lower energy bins, for example: in the 2.0 – 6.0 keVee interval the modulation amplitude is (0.0131 ± 0.0016) cpd/kg/keVee with a phase and period which favour June 2nd and one year, respectively.

Following the method of reference [55], a χ^2 is calculated using the data of Table 3.1. The theoretical rate is computed at the central energy point of the bin interval and an average of its value at maximum and minimum Earth velocity, v_e, is taken as the modulation amplitude. Furthermore, the Gaussian energy smearing of reference [55] is introduced with a finite detector resolution which is parametrized in terms of energy. The energy resolution is given by

$\sigma_{res}/\text{keV} = 0.448\sqrt{E/\text{keVee}} + 9.1 \times 10^{-3} E/\text{keVee}$.

Finally, we remark on the DAMA quenching factors.[1] Although the quenching factor of iodine, $Q_I = 0.09$, is well established, different groups report different values on the sodium quenching factor, Q_{Na} (see section 5.2 for more details). An accurate knowledge of the sodium quenching factor is important because larger values of Q_{Na} can relieve the tension between the DAMA and CoGeNT best-fit regions, as well as with the null experiments [55]. The sodium quenching factor is generally anticipated to be a function of recoil energy and a recent analysis has confirmed such a dependence [56] which we will investigate in Chapter 5. For this thesis, we adopt the conservative choice $Q_{\text{Na}} = 0.3 \pm 0.1$, unless stated otherwise.

3.3 CRESST-II

The CRESST-II cyrogenic DM experiment employs a number of 0.3 kg scintillating $CaWO_4$ crystals in its search for DM interactions [57–59]. The recoil energy deposited by interacting DM particles is converted into phonons and photons which are measured by a series of phonon and light detectors. While the phonon signal provides a measurement of the total event energy, the light signal is used to reduce the electron-photon backgrounds and for the nuclear recoils, it also provides some information on which nucleus is recoiling.

CRESST-II obtains after 730 kg·days of exposure a total of 67 events that satisfy all acceptance cuts [58]. As it turns out, estimates for the total background contribution do not appear to be able to explain all the observed events. The result is that CRESST-II reports an excess signal with statistical significance $> 4\sigma$.

Table 3.2 shows the CRESST-II data separated into 6 bins along with the estimated background in each bin.[2] To compute the estimated background in each bin B_i, we integrate, for the energy intervals of Table 3.2, the spectrum of each background source corresponding to the low-mass benchmark point in Figure 11 of reference [58]. A χ^2 test is performed by fitting the predicted number of dark matter events to the data summarized in Table 3.2. Also, we take into

[1] Quenching factor here means the fraction of the total recoil energy that goes into scintillation.

[2] The CRESST-II best-fit region is highly sensitive to the binning procedure. The energy bins of Table 3.2 are chosen to produce confidence intervals which are compatible to those published by CRESST-II, where a complicated maximum likelihood analysis is performed.

Bin (keV)	Total events	Estimated background
10.2 – 15	20	6.4
15 – 20	17	10.4
20 – 25	10	8.0
25 – 30	7	6.3
30 – 35	5	5.6
35 – 40	8	5.1

TABLE 3.2: Energy intervals, total number of events, and estimated background used to fit the CRESST-II unmodulated data.

account the individual energy thresholds of the 8 detector modules: 10.2, 12.1, 12.3, 12.9, 15.0, 15.5, 16.2, 19.0 keV. The χ^2 is calculated in the usual way:

$$\chi^2 = \sum_{i=1}^{6} \left(\frac{R_i + B_i - \mathrm{data}_i}{\delta \mathrm{data}_i} \right)^2, \tag{3.2}$$

where we define $\delta\mathrm{data}_i = \sqrt{\mathrm{data}_i}/2$. The theoretical number of events per bin is computed assuming detection efficiencies, ϵ, for the three target elements. These are taken to be: $\epsilon = 0.9$ for O,W and $\epsilon = 1.0$ for Ca, which take into account their acceptance region (following reference [60]). Furthermore, we introduce a Gaussian energy smearing defined by the detector resolution $\sigma_{res} = 0.3$ keV.

3.4 XENON100

The XENON100 (and XENON10) experiment uses liquid xenon as both WIMP target and detection medium, and measures simultaneously the scintillation (S1) and ionization (S2) signals produced by particle interactions in the fiducial volume [61–63]. The ratio S2/S1 is used to discriminate between WIMP (or neutron) and electromagnetic signals, thus making it possible to resolve the background contribution arising from gamma and beta interactions. The S1 signal is measured in terms of the number of photoelectrons (PE) captured by the detector.

XENON100's 2012 analysis of 224.6 live days $\times$ 35 kg exposure observes two candidate events in the pre-defined nuclear recoil energy range 6.6 – 30.5 keVnr (3 – 20 PE), one at 7.1 keVnr (3.3 PE), and at 7.8 keVnr (3.8 PE) [63]. The expected number of events due to background is 1.0 ± 0.2. The recoil energy deposited by interacting WIMPs is related to the number of PEs in the S1 signal through the response function $\mathcal{L}_{eff}$, that is:

$$S1 = \mathcal{L}_{eff}\frac{L_y S_{nr}}{S_{ee}}E_{nr}, \tag{3.3}$$

where the factors $S_{ee} = 0.58$ and $S_{nr} = 0.95$ describe the scintillation quenching due to the electric field. $L_y = (0.28 \pm 0.04)$ PE/keVee is the updated response to 122 keV gamma rays. A low mass DM interpretation of XENON100 is highly sensitive to the form of the response function [64, 65]. In this report, we use the central parametrization of $\mathcal{L}_{eff}$ in Figure 1 of reference [62], which has been logarithmically extrapolated to zero below 3 keVnr.

To determine bounds on light DM, we use the maximum gap method of reference [66]. This method involves partitioning the photoelectron search window (3 - 20 PE) into intervals or "gaps" which are separated by the observed events. In the present case, these intervals are found to be: 3 – 3.3, 3.3 – 3.8, 3.8 – 20 PE. For a given DM model, the predicted number of events in each gap is calculated taking into account both signal and background contributions in that gap. The background events are assumed to be uniformly distributed throughout the search region. Limits are set by singling out the interval in which the probability of observing no events is minimal. The Poissonian probability that more than 0 events should have been observed in this window is given by the function $C_0(x, \mu)$, that is:

$$C_0(x, \mu) = \sum_{k=0}^{m} \frac{(kx - \mu)^k e^{-kx}}{k!}\left(1 + \frac{k}{\mu - kx}\right), \tag{3.4}$$

where x is the total number of events in the maximum gap, μ the total number of events in the full PE range, and $m = \text{Floor}(\mu/x)$. As an example, the 95.4% CL is set by determining the value of the cross section which gives $C_0 = 0.954$.

The calculation of the number of events in any given gap involves a convolution of the DM matter rate with an acceptance function $A(E_{nr})$, which depends on quality cuts and S2/S1 energy resolution discrimination. A full discussion on $A(E_{nr})$ can be found in reference [67]. More explicitly, the number of events, $\mathcal{N}$, in the PE range S_a - S_b is:

$$\mathcal{N} = \int A(E_{nr})\frac{dR}{dE_{nr}}dE_{nr}, \tag{3.5}$$

where

$$A(E_{nr}) = \epsilon_2(E_{nr}) \int_{S_a}^{S_b} \left[\epsilon_1(S1') \sum_{N_{pe}=1} \text{Gauss}(S1'|N_{pe}) \times \text{Pois}(N_{pe}|\mu(E_{nr}) \right] dS1'. \tag{3.6}$$

In equation (3.6), the Gaussian functions have mean value N_{pe} with width $\sigma_{res} = 0.5\sqrt{N_{pe}}$, and $\mu(E_{nr})$ is the expected S1 signal at energy E_{nr} as determined using equation (3.3). Finally, the cut acceptances $\epsilon_2(E_{nr})$ and $\epsilon_1(S1')$ are given by the dashed red and a combination of the solid blue and dotted green curves, respectively, in Figure 1 of reference [63].

3.5 XENON10

A low-energy threshold analysis that is sensitive to light WIMPs is possible with XENON10 search data, if one considers only the S2 electron signal in measuring nuclear recoil energies [68]. By discarding the primary scintillation signal, lower threshold energies may be achieved however, this comes at the expense of compromising the ability to discriminate between incoming particle types. In total, XENON10 observes 26 events in the range of the S2 signal, that is S2 = 5 – 43 electrons.

The nuclear energy of each event crucially depends on the so-called Q_y parameter which relates nuclear recoil energy to the number of electrons in the S2 signal,

$$S2 = Q_y(E_{nr})E_{nr}. \tag{3.7}$$

At low recoil energies, the energy scale is calibrated purely in terms of the S2 signal since a low number of primary scintillating photons does not result in a measurable S1 signal. The exact form of the electronic response function Q_y has come into question. The Q_y that XENON10 reports has been criticised by references [69, 70] which propose an electronic response function with lower energy threshold cut-off. Figure 3.1 shows the competing forms of Q_y. For our purposes (as was done in [71]), we adopt the central curve of Figure 3.1 which takes the average between the results of XENON10 and the solid black curve in Figure 2 of reference [69]. The intermediate choice yields an energy threshold for XENON10 of E_{min} = 2.8 keV. As an upper

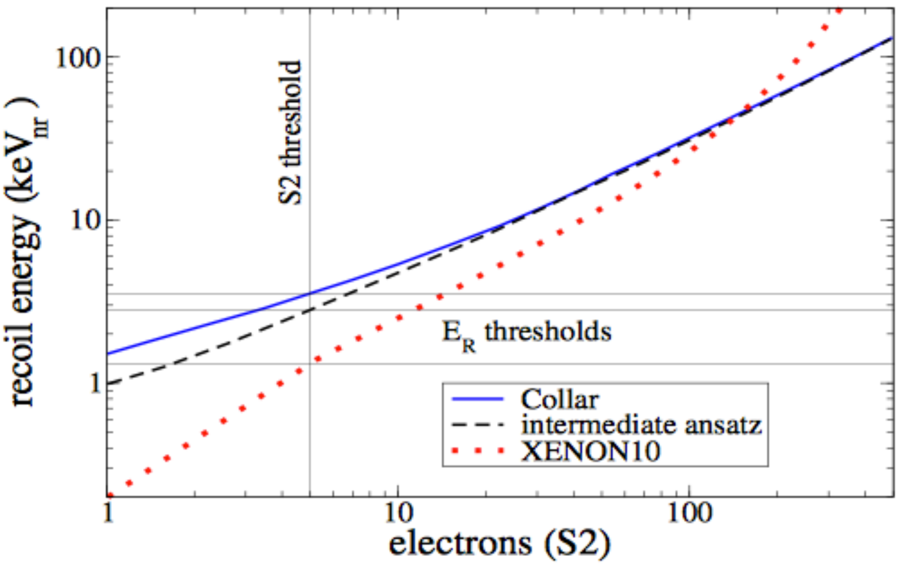

FIGURE 3.1: Forms of the electronic response function Q_y. The solid curve labelled Collar is from reference [69], dotted curve is that employed by XENON10 (see [68]), the dashed curve is the hypothetical intermediate ansatz. Figure taken from reference [71].

limit to the search window, we follow XENON10 in taking $E_{max} = 10$ keV.

Like the official XENON10 analysis, CLs are calculated using the p_{max} method of reference [66]. The p_{max} method is an extension of the maximum gap method appropriated to situations in which larger numbers of events are observed. Each event is assigned an energy according to equation (3.7) and energy intervals are defined to be between any two events. For a given cross section, one finds the interval that is most likely to contain more events than what was actually observed in that interval. The maximal probability over all possible intervals is then used to set limits on the cross section. Finally, in computing the expected number of events, Gaussian smearing is performed using the energy resolution of reference [72] which is parametrized by $\sigma_{res} = \sqrt{E_{nr}/Q_y(E_{nr})}$. This is the corrected version of the energy resolution from the one used in the official XENON10 analysis.

3.6 CDMS-Ge

The CDMS-II experiment, operating at the Soudan Underground Laboratory, consists of an array of germanium and silicon solid-state detectors which measure the energy deposited by particle interactions via ionization and athermal phonon signals [73–76]. CDMS-II rejects electronic backround based on the ratio of ionization to phonon signals, since backgrounds tend to deposit more energy in the form of ionization.

Our study of the germanium target material, referred to here as CDMS-Ge, takes into account data from the most recent low-threshold analyis of 19 germanium detectors [75]. The reported threshold of 2 keV has been disputed by reference [77] which favours 5 keV as a more realistic threshold. [77] argues that the ionization pulses which are used as references in defining the nuclear recoil energy scale, are poorly resolved against the electronic noise in the ionization channel below roughly 5 keV. Despite this, we take the threshold energy to be 2 keV, resulting in more stringent constraints.

Following reference [55], we restrict our analysis to the T1Z5 detector data which observes 34 events in the 2 keV to 20 keV search window with a corresponding exposure of 35 kg·days. The best sensitivity to low-mass WIMPs is obtained by the T1Z5 detector which displays the lowest threshold and greatest ability to discriminate between electron and nuclear recoils. Our analysis takes the conservative approach which assumes all of the observed events are DM induced recoils.

CLs are computed using the maximum gap method of reference [66] in the 2 – 20 keV energy range and assuming all 34 events observed are due to DM recoils. In order to calculate the number of events in each bin, we use the efficiency found in the inset of Figure 1 of reference [75].

3.7 CDMS-Si

Earlier this year, the CDMS-II experiment released an official analysis of its silicon detectors corresponding to 140.2 kg·days of data aquisition in its search for WIMPs [78]. Using the same experimental techniques as in the germanium detectors, the CDMS-Si data reveals three candidate DM events in the 7 – 100 keV energy range at recoil energies 8.2, 9.5, and 12.3 keV, with a predicted number of background events due to surface-event leakage of $0.41^{+0.20}_{-0.08}(\text{stat.})^{+0.28}_{-0.24}(\text{syst.})$. The CDMS collaboration claims that the probability of three or more events being produced by known backgrounds in the energy range of interest is 5.4%, indicating the existence of an excess signal that might be attributed to interacting DM.

An elastic SI DM interpretation of the excess signal results in the highest likelihood occurring for a DM mass of 8.6 GeV and WIMP-nucleon cross section of 1.9×10^{-41} cm^2. Reference [78] demonstrates the compatibility of their signal with that claimed by CoGeNT, however, show that it is at odds with other positive-signal experiments.

For our analysis, we test the CDMS-II silicon excess against a DM hypothesis only in the case of our halo-independent formalism. Following the official publication, we do however employ the maximum gap method in the 7 – 100 keV energy range in order to set upper limits on the DM-nucleon cross section using CDMS-Si data. The nuclear recoil efficiency of Figure 1 of reference [78] is inserted into the calculation of silicon event rates.

3.8 SIMPLE

The SIMPLE experiment operates 15 C_2ClF_5 superheated droplet detectors. The event-by-event analysis searches for particle-induced bubble nucleations of the superheated liquid droplets which can transition to the gas phase [79]. One requirement for nucleation of the gas phase is that the energy deposited by incident particles be greater than a thermodynamic minimum. As a result, it is possible to precisely set the threshold energy which, for the relevant data, turns out to be 8 keV.

Following [55] we consider only the results of the recent Stage 2 data which reports one recoil event, consistent with the number of estimated background neutrons over an effective exposure of 6.71 kg·days. The latest results provide better neutron shielding and a more rigorous analysis of the individual detector run signals, sensitivities, and bubble nucleation efficiency.

To compute CLs, a χ^2 is constructed out of the Poissonian likelihood defined by

$$\mathcal{L} = e^{-\mathcal{N}_{tot}}, \tag{3.8}$$

where $\mathcal{N}_{tot}$ is the total theoretical number of dark matter events. This method results in conservative bounds which are compatible with those obtained by SIMPLE.

As a final remark, we comment on criticisms regarding the observation of acoustic discrimination, SIMPLE's reported sensitivity to low-mass DM, and the longevity of the SIMPLE modules. References [80, 81] both raise concerns over the fact that the SIMPLE analysis does not employ the same parent acoustic distribution for the neutron calibration data set and events in the physics data identified as coming form neutrons. It is argued that using different distributions in the calibration and physics data directly affects the resulting WIMP sensitivity. Additionally, [80] calls into question the credibility on the claim by SIMPLE that it has achieved improved limits on low-mass WIMPs. The main argument relies on reports that the SIMPLE detectors are not able to contain target mass diffusion or gas leakage and therefore, suffer from a poor "shelf-life". Reference [80] contends that based on past experience with superheated droplet detectors, a relaxation in the sensitivity of SIMPLE detectors is expected.

3.9 EDELWEISS-II

A search for low-energy WIMP-induced nuclear recoils is presented in the recent EDELWEISS-II paper which analyses a restricted data set from the results of ten heat-and-ionization detectors [82]. Selected on the basis of threshold and background performance, the results of four germanium detectors, corresponding to an exposure of 113 kg·days, is used to achieve a low-background sensitivity to nuclear recoils down to 5 keV. Accordingly, measured recoil energies are limited to < 20 keV.

Measurements of the heat energy allow for an evaluation of the nuclear recoil energy E_r. Furthermore, signals from the ionization channels are used to reject the main backgrounds of nonfiducial interactions such as surface beta radioactivity, gamma-ray-induced interactions in the fiducial volume, and ionizationless events. The result is an efficiency loss for fiducial events as a function of ionization energy described by the equation:

$$\epsilon_{ion} = 0.95\big[1 - \exp\left(-1.87(E_{ion} - 1.25)\right)\big], \tag{3.9}$$

where E_{ion} is in keVee. Additionally, at low energy there is an efficiency loss caused by the online trigger. The trigger efficiency as a function of recoil energy is given by

$$\epsilon_{online} = 0.5\left[1 + \mathrm{Erf}\left(\frac{E_r - E_{thresh}}{\sqrt{2}\sigma}\right)\right], \tag{3.10}$$

with E_{thresh} the recorded trigger threshold and σ the measured resolution. EDELWEISS-II reports that the average trigger efficency for the selected data is 78% at 5.0 keVnr and 90% at 6.3 keVnr. Therefore, given the available data, we make the approximation $E_{thresh} = 3.03$ keV and $\sigma = 2.55$ keV.

Taking into consideration the measured resolutions of fiducial ionization energy $\sigma_i = 0.7$ and heat energy $\sigma_r = 0.8$, it is possible to calculate the DM signal density:

$$\begin{aligned}\rho(E_r, E_i) &= \frac{\epsilon_{online}(E_r)\epsilon_{ion}(E_i)}{2\pi\sigma_r\sigma_i} \\ &\times \int dE \frac{dR}{dE}(E) \exp\left(-\frac{(E_r - E)^2}{2\sigma_r^2} - \frac{(E_i - Q_n E)^2}{2\sigma_i^2} \right),\end{aligned} \tag{3.11}$$

where the integral is over all E (the true recoil energy), and the parameterization $Q_n = 0.16(E_r/\text{keV})^{0.18}$. To compute the expected number of DM events, the signal density is integrated over the E_r search region, that is $5 - 20$ keV, and over all ionization energies.

The data shows no evidence for an exponential distribution of low-energy nuclear recoils that could be attributed to standard DM scattering. The Poissonian likelihood of equation (3.8) is used to compute upper limits on the DM scattering cross section with results that are in agreement with EDELWEISS-II.

Chapter 4

Isospin-Violating Dark Matter: A Review

In this chapter, we review the origin and evolution of the isospin-violating dark matter paradigm with a focus on important results as they apply to direct detection experiments. Additionally, an update on IVDM is provided along with a discussion on the results of various extentions to the standard DM model. To conclude the chapter, a review of phenomenological findings of prominent halo-independent analyses is given. In subsequent chapters, we will refer to the body of content laid out here in order to give straightforward comparisons between the results of this research and those of previous studies.

4.1 From Dirac neutrinos to generalized IV couplings

In 1985, Goodman and Witten released a seminal paper [83] which would soonafter initiate the search for weakly interacting dark particles in ground-based detectors. Inspired by the potential for possible dark matter candidates to be detected by a then recently proposed neutral-current neutrino detector [84],[1] a prescription for computing dark matter event rates was outlined. In addition to analysing spin-dependent and strong interactions, Goodman and Witten considered the case in which the unknown halo particle contained vector couplings to Z bosons and thus could scatter with nuclei via Z exchange. It could be shown that the DM-nucleon elastic scattering cross section satisfied the following relation:

$$\sigma \propto [N - (1 - 4\sin^2\theta)Z]^2, \tag{4.1}$$

where N and Z are the number of neutrons and protons in a target nucleus, respectively. Equation (4.1) resembles the spin-independent DM-nucleon cross section of Chapter 2 since $N = A - Z$. Although equation (4.1) represents a model containing vector couplings, it is clear that isospin violation naturally arises in a theory where the dark matter candidate has coherent weak interactions since we may deduce the relation $f_p/f_n = -(1 - 4\sin^2\theta)$. In fact, if the Galactic halo is dominated by a heavy standard Dirac neutrino then $\theta = \theta_W$ is simply the Weinberg angle.

Motivated by the concepts of Goodman and Witten, the first limits on WIMP-nucleon cross sections would be computed by Ahlen *et* al. in 1987 using the results from then already existing Ge double-beta decay experiments [85]. The predicted rate of recoils were computed using Dirac neutrino dark matter as the dominant halo component for both the SI vector and SD axial-vector interactions. Not before long, other groups [86, 87] would utilise double-beta decay experiments in order to compute limits on dark matter cross sections under the heavy Dirac neutrino assumption. Over the next decade, a number of experiments dedicated to dark matter searches were constructed and tested against various DM hypotheses including: Baksan [88], COSME [89], DAMA-NaI [90, 91], DEMOS [92], Heidelberg-Moscow [93, 94], and UKDMC [95], among others. However, by the mid-nineties heavy Dirac neutrinos were ruled out by a combination of collider searches, cosmological considerations, and direct detection experiments. The key reason is the following: if a Dirac neutrino with mass $\gtrsim 1$ GeV were made to yield the correct relic abundance, its elastic cross section with SM nuclei induced by Z-exchange would be sufficiently

[1]The neutral-current neutrino detector originally proposed by Drukier and Stodolsky, relied on the ionization by neutrinos of grains of superconducting material embedded in a non-conducting material and in a magnetic field. Upon ionization, the grain would no longer be superconducting hence, a change in the magnetic field would occur which would create a measurable signal. Interestingly enough, their detector was never constructed.

large that it should have been seen at direct detection experiments.

With Dirac neutrinos out of the picture, efforts shifted towards models consisting of scalar and axial-vector DM. One of the first scalar spin-independent DM candidates to be considered was the well-favoured, theoretically motivated neutralino. Neutralinos arise in the *minimal supersymmetric standard model* (MSSM) as the lightest supersymmetric particle. For early papers which compute limits on neutralino-nucleon elastic cross sections see references [96, 97]. It is possible to show that the neutralino-nucleon spin-indpendent cross is given by:

$$\sigma_0^{SI} = \frac{8G_F}{\pi} m_Z^2 \mu_N^2 A^2 \frac{\alpha_H^2}{m_h^4}, \tag{4.2}$$

where m_Z is the mass of the Z^0 boson, m_h the mass of the Higgs boson, and α_H an expression which depends on the neutralino-quark couplings mediated by Higgs bosons and squarks [98, 99]. Notice in equation (4.2) the A^2 dependence of the WIMP-nucleon cross section. As it so happens, α_H depends on parameters which are independent of the target material and the mass of the neutralino. Therefore, the spin-independent WIMP-proton cross section of Chapter 2 can be related to α_H under an IC scenario as follows:

$$\sigma_p^{SI} = \frac{8G_F \mu_p^2}{\pi} \frac{m_Z^2}{m_h^4} \alpha_H^2. \tag{4.3}$$

Hence, equation (4.3) demonstrates that an analysis of DM which evokes the σ_p^{SI} cross section of Chapter 2, can serve as an effective theory to more fundamental interactions between DM and SM nuclei (in this case interactions between neutralinos and nuclei). By the new millennium, the computation of upper limits on DM cross sections started to concentrate less on the specifics of neutralino physics, and more on general effective models of SI DM interacting via scalar couplings. Even so, the assumption that scalar DM be IC was an established theme which, despite the knowledge of more extensive forms of the DM-nuclei cross section containing distinct DM-neutron and DM-proton couplings [16], woud not be broken in favour of a general IV analysis of direct detection for some time.

4.2 Early results for IVDM

In 2003, Kurylov and Kamionkowski released the first generalized analysis of direct detection searches in which the parameter f_n/f_p was allowed to vary [100]. At the time, DAMA-NaI was the only detector reporting an excess signal compatible with DM-nucleon scattering, and null bounds were placed using data from the following experiments: DAMA-Xe, EDELWEISS, and ZEPLIN-I. Results were presented in the σ_n^{SD}-M_{DM} plane for purely SD dark matter (assuming $a_p/a_n = 0$) and the $\sigma_{p(n)}^{SD}$-σ_p^{SI} plane for combined DM (assuming $a_n/a_p(a_p/a_n) = 0$). Kurylov and Kamionkowski were able to conclude:

- Compatibility of all the data can be achieved with a predominantly SD DM-proton interaction.
- Almost purely SI interacting DM is allowed for heavier WIMPs of ~ 50 GeV provided that $-0.77 \lesssim f_n/f_p \lesssim -0.75$ and that the SI cross section statisfy $\sigma_p^{SI} \approx 0.0035$ pb.

The prospect of a negative ratio between DM-proton and DM-neutron couplings of order unity being able to accomodate the DAMA best fit region was further supported by Giuliani [101]. Reference [101] showed that in a fully isospin-dependent interaction scenario, that is one where $f_n = -f_p$, constraints on the DAMA *region of interest* (ROI) that arise from null experiments are $1 - 2$ orders of madnitude less stringent.

The first published results from CoGeNT's initial run of their ultra low noise germanium detector brought about a new period in DM direct detection. Kopp, Schwetz, and Zupan were the first group to interpret the 2010 CoGeNT results in terms of a positive signal DM scenario [102]. Amidst a time of uncertainty regarding the form of the CoGeNT background, Kopp *et* al. demonstrated a clear incompatibility between the CoGeNT and DAMA best fit regions under a SI IC DM model, not to mention across the board tensions with null bounds. On the other hand, the addition of a positive mass splitting parameter was seen to reduce the conflict between the DAMA ROI and excluded areas of parameter space for both SI and SD cases.

Shortly after CoGeNT's results were published, Chang *et* al. demonstrated that the introduction of generalized SI DM couplings, in particular taking $f_p \approx -f_n$, strengthens the overall agreement between CoGeNT and DAMA, and positive-signals with null constraints [103]. Additionally, MD scattering was shown to further improve the situation.

These attempts to explain direct detection of DM failed to provide a quantitave analysis of the models employed and, in the case of IV analyses, failed to account for the possibility of isotopes in the target material. In 2011, Feng *et* al. explored the latter of these points by introducing the abundunces of nuclei with multiple isotopes into their research on IV couplings [26]. Reference [26] was able to conclude that for $-0.72 < f_n/f_p < -0.66$, there exists marginal agreement between the CoGeNT and DAMA ROIs, and both can be brought into consistency with the XENON100 bound due to a reduction in its sensitivity to WIMPs. It was pointed out that for such values of f_n/f_p there occurs almost complete destructive interference between the proton and neutron content of the isotopes in the WIMP-xenon cross section, resulting in xenon's diminished sensitivity to DM. On the other hand, the CoGeNT constraint was found to marginally exclude the overlaping region, and since CoGeNT utilizes Ge, the tension between CoGeNT and CDMS-Ge could not be alleviated by isospin violation alone. A similar conclusion was reached by Frandsen *et* al. [104] however, inelastic scattering of mass-splitting ~ 15 keV was shown to improve the universal fit for IVDM. Working in the σ_n^{SI}-M_{DM} plane, another important discovery was that larger values of $Q_{\rm Na}$ were seen to reduce tensions between DAMA and null experiments.

Arguably, the most robust analysis of IVDM and its possible extensions was carried out in late 2011 by Farina *et* al. [55] where, in addition to IV interactions, inelastic couplings, MD couplings, velocity suppressed interactions, resonant scattering, and possible astrophysical and experimental uncertainties were all expoited (individually and in some cases combined) in order to unearth a successful fit to the data. A nominal feature of reference [55]'s study of a DM interpretation of direct detection data, was their quantitative approach in introducing a chi-squared value corresponding to the sum of chi-squareds of the positive signal experiments. By minimizing an appropriate chi-squared statistic, benchmark values for parameters of the theory could be deduced, in contrast to the approach of predecessors whereby parameter values were chosen on an *ad hoc* basis. The results of Farina *et* al. are summarised as follows:

- Allowing f_n/f_p to float results in an improvement in the compatibility of CoGeNT and

DAMA. Also, tuning the isospin violation ratio such that the neutron and proton components cancel eachother weakens the tension of positive-signal results with null experiments. For an IVDM model with $v_0 = 220$ km/s, $v_{esc} = 500$ km/s, and $Q_{\rm Na} = 0.4$, the benchmark value for the isospin violation ratio is $f_n/f_p = -0.65$.

- Larger values of $Q_{\rm Na}$ result in better agreement between DAMA and CoGeNT.

- For MD scattering, q^{2n} form factors with $n > 0$ have the effect of causing an increase in the separation between DAMA and CoGeNT ROIs, given that such form factors are seen to enhance the CoGeNT signal relative DAMA's. However, taking $f_n/f_p \sim -0.66$ for q^2 and q^4 scattering mends this problem resulting in an overall fit which is only somewhat more consistent than the q^0 case. Form factors q^{2n} where $n < 0$ are not seen to improve the global fit with respect to the $n = 0$ case.

- Velocity-dependent elastic scattering is introduced by inserting form factors into the differential rate which go like v^2/v_0^2 or v^4/v_0^4 for some mean velocity v_0. A small improvement in the overall fit is realised for DM-nucleon coupling ratios in the range $-0.6 < f_n/f_p < -0.56$.

- An inelastic coupling is found to improve the overall fit for both endothermic, and exothermic DM models. For up-scattering, the benchmark parameters are $f_n/f_p \approx -0.66$ and $\delta \approx 11$ keV, and for exothermic DM they are $f_n/f_p \approx -0.68$ and $\delta \approx -10$ keV.

Despite these improvements, the authors concluded that despite the use of many additional parameters in the SI DM scenario, the prospect of providing a simultaneous explanation to all the data is a difficult task. The authors also entertain the idea that one or possibly both of the positive-signal experiments is/are seeing some phenomenon unrelated to DM.

By 2012, the CRESST-II collaboration had published results that claimed to see a significant excess of events compatible with a DM hypothesis. Shortly thereafter, Kopp *et* al. performed (separately) a SI inelastic and IV analysis of the CRESST-II data, making comparisons to the DAMA ROI, and testing CRESST's robustness against null constraints [105]. For the inelastic case, a larger than usual value of the mass splitting (90 keV) was used causing DM scattering to occur exclusively on W. The results displayed an incompatibility in the CRESST-W and DAMA-I ROIs, as well as tension with the XENON100 bound. For an elastic SI IV scenario with $f_n/f_p = -0.7$, Kopp *et* al. found that although IV couplings were able to achieve clear improvement over the IC case, a low probability of consistency from their parameter goodness of fit test was achieved for a CRESST + CDMS-Ge + XENON100 hypothesis.

4.3 In light of new experimental results

Since the meaningful conclusions of Farina *et* al., a collection of new experimental findings have come to light which significantly alter the DM picture of direct detection. As mentioned in Chapter 3 these are: the 2012 release of XENON100's 225 live days of direct detection data, an updated analysis on surface event contamination in the results of CoGeNT, a correction to the energy resolution in the XENON10 analysis, and the publishing of official silicon detector data by the CDMS-II experiment. In this section, we review the effects that some of these new results have on the DM parameter space.

Immediately following the release of XENON100's 2012 results, Jin, Miao, and Zhou published a paper which gave an IV interpretation of the data [32]. For a WIMP mass of 10 GeV, the 2012 XENON100 limit on the DM-proton cross section for IVDM with $f_n/f_p = -0.7$ turned out to be $\sim 3.6\times$ stronger than the 2011 bound. Accordingly, the new constraint was discovered to rule out almost all positive-signal ROIs. In a subsequent version of Jin *et* al.'s paper, the updated surface event contamination in CoGeNT data was joined to their analysis. The result being a worsening in the compatibility between the DAMA and CoGeNT signals to the extent that no overlap is observed at the 3σ level. Conversely, a small improvement was seen for IVDM in the tensions that null limits impose on the CoGeNT ROI.

An alternative assesment of DM signals in direct detection searches by Arina, employs Bayesian statistics as a method of comparing various experiments [106]. An advantage to this method of analysis is that it marginalises over experimental systematics and astrophysical uncertainties. Taking into account both the 2012 XENON100 result and surface event contamination at CoGeNT,[2] the outcome between elastic IC and IV scattering was determined to be inconclusive at odds of 2 : 1, while inelastic scattering was found to be disfavoured with the odds of 1 :

[2]Reference [106] employs a version of the surface event contamination function from J. I. Collar's talk given at the International Dark Matter Conference in Chicago, 2012. This version postulates a smaller fraction of surface events in the data than the one presented in the official CoGeNT release which appeared after this talk.

32. Consequently, it is argued in the conclusion of reference [106] that since the data does not support extra free parameters, positive-detection regions are best left to be described by elastic IC DM scattering. It should be noted that the low energy analyses of XENON10 and CDMS are not considered, in addition to the absence of a combined inelastic, IV hypothesis.

In reference [107], Yang investigates the compatibility between CoGeNT (2012) and DAMA along with bounds from XENON100 and PICASSO in terms of IV SI and SD DM in f_n-f_p and a_n-a_p space, respectively. The findings of Yang's SI IVDM analysis are similar to those of previous works. On the other hand, results are shown to constrain the SD couplings in such a way that requires $|a_n| < 0.6$ and $|a_p| < 1.0$, for cross sections $\sigma_n^{SD} < 5.6 \times 10^{-38}$ cm^2 and $\sigma_p^{SD} < 5.6 \times 1.6^{-37}$ cm^2. It is also demonstrated that SI IVDM fails to reconcile the XENON100 constraint with the DAMA and CoGeNT ROIs. However, this analysis is contrained to a WIMP candidate of mass 10 GeV and it is not explored whether or not other values of the mass change the results of an overall fit to the data.

Moving on, the possibility of an excess signal in CDMS-Si data is given an isospin-violating treatment in reference [108] by Feng *et* al. The analysis demonstrated that by using an isospin violation ratio of $f_n/f_p = -0.64$, the positive-signal ROIs corresponding to the excess signals at CDMS-Si and CoGeNT could be made to agree. Furthermore, large portions of the CDMS-Si claimed signal are able to evade the stringent XENON100 constraint in the IVDM picture. However, compatibility between the CDMS-Si region and that of DAMA or CRESST-II is not observed, and the analysis does not consider CDMS-Si data as an upper limit.

4.4 Results from halo-independent analyses

Perhaps the greatest challenge facing the comparison of direct detection results are the various uncertainties that permeate the data. In particular, the exact structure of the DM halo in our Galaxy is subject to a number of possible uncertainties. Some models of the DM distribution within the halo predict isotropic profiles whereas others favour anisotropic profiles. Furthermore, the possibility of DM streams, local overdensities, sub-halos, and halo rotation are known to significantly alter expectations for the DM event rate.

In recent months, there has been a surge in the number of halo-independent analyses, all of which whose aim is to compare the results of DM direct detection in a way that removes assumptions regarding the distribution of DM in our Galaxy. In the method proposed by Fox, Lui and Weiner, observations of one experiment were mapped directly into another, thus circumventing astrophysical uncertainties arising from the DM halo profile [109]. As argued in their paper, interpreting the data in $\eta(v_{min})$-M_{DM} space over σ_p^{SI}-M_{DM} space is advantageous because it readily demonstrates the relationships between the regions of v_{min}-space probed by different experiments, and allows for an easy method of discerning the existence of possible tensions in the data. Their IC analysis shows that for a comparison of XENON10 and CoGeNT, the excess signal observed by CoGeNT is compatible with null results in $\eta(v_{min})$-M_{DM} space provided that low values of $\mathcal{L}_{eff}$ in XENON10 are chosen. On the other hand, constraints placed by XENON10 on the excess signal predicted by DAMA show that for most choices of the DM mass, the modulation fraction[3] is too small for a consistent description with elastically scattering WIMPs. Nevertheless, it is found that constraints on lower modulation fractions are weakened for sufficiently larger values of the sodium quenching factor. Finally, their analysis reveals that an elastic DM interpretation of the excess of events reported by the CRESST collaboration is highly unlikely due to the severity of the CDMS-Si and XENON10 constraints.

The method of Fox, Lui, and Weiner suffers from a key disadvantage: comparisons between different experiments become difficult to make when the regions of v_{min}-space probed are not the same. In reference [110], Frandsen *et* al. address this problem by making the astrophysical unknowns explicit, thereby causing an assessment of their impact within the framework of various DM models to become more apparent. To achieve this, Frandsen *et* al. mapped all experimental results into v_{min}-space and inferred from the usual DM analysis the best estimate of the DM mass. Focusing on the 6 - 15 GeV mass range, they established that there exists a particular anisotropic choice of $\eta(v_{min})$ which enables a consistent description of CoGeNT, CRESST, and DAMA. However, bounds from XENON10/100 and CDMS-Ge/Si are shown to remain in tension with the regions of v_{min}-space probed by positive-signal experiments. On the contrary, the employment of IV couplings with $f_n/f_p \approx -0.7$ resolved the conflict with the XENON and CDMS-Ge constraints, although this scenario was also seen to enhance the upper limits set by

[3]The modulation fraction is defined by [109] to be $(S-W)/(S+W)$, where S and W are the summer and winter event rates, respectively.

SIMPLE, CDMS-Si and the CRESST-II commisioning run. Moreover, Frandsen *et* al. show explicitly how the specific choice of DM halo profile can widely affect the form of $\eta(v_{min})$, and hence its influence on ROIs and upper limts in σ_p^{SI}-M_{DM} space for both standard and IV DM. As a result, the importance of carrying out a halo-independent analysis is further solidified.

A crucial pitfall to the analysis performed in reference [110] is its inability to fully incorporate the efficiencies, resolutions, and/or additional acceptance factors associated with the individual experiments. Gondolo and Gelmini confront this problem in reference [111] in which they extend the halo-indpendent analysis to include energy resolutions and efficiencies with arbitrary energy dependence. Their conclusions are similar to that of [110] in that the XENON100 and CDMS bounds tightly restrict the positive-signal measurements of $\eta(v_{min})$ in the elastic IC SI model, and that the possibility of IV couplings at low energies remains plausible. Furthermore, the CRESST-II signal in v_{min} is found to be incompatible with the DAMA and CoGeNT modulation signals.

Early this year, Nobile *et* al. presented a halo-independent analysis [112] which incorporates: the new CDMS-Si results both as a bound and excess signal, the updated surface event contamination at CoGeNT, and the possibility of energy dependent quenching factors in NaI crystals. They test the halo-independent hypothesis for various values of the WIMP mass, for IC DM, and IV scenarios with $f_n/f_p = -0.7$ using the techniques of [111]. The results are summarised as follows:

- For low values of $Q_{\rm Na}$ and hence those probed by the energy-dependent quenching factor, it is not possible to explain the DAMA modulation data given a reasonable choice of escape velocity for $\mathcal{O}(10)$ GeV WIMPs. In addition, the DAMA measurments of $\eta(v_{min})$ are found to be excluded by several null constraints.

- Taking $f_n/f_p = 1$, only the lower energy bins of the CoGeNT (and DAMA for sufficiently large $Q_{\rm Na}$) modulation data are able to circumvent XENON10, XENON100 and CDMS-Ge modulation bounds.

- For IV couplings with $f_n/f_p = -0.7$, CDMS-Si bounds are strengthened leading to the exclusion of all central values of the CoGeNT data, except at the points corresponding to the lowest energy bins.

- The central values of the CDMS-Si unmodulated signal is in apparent conflict with upper limits placed by XENON100 in the IC case. For the IV scenarios, the CDMS-Si signal is allowed. However, the predicted unmodulated rate becomes lower than the modulated ones favoured by CoGeNT and DAMA, which is a problematic contradiction if the unmodulated and modulated components are to arise from the same DM candidate.

In a similar paper, Frandsen *et* al. [113] test a halo-independent DM interpretation of the CDMS-Si excess signal against XENON10 and XENON100 bounds but with some key differences. Firstly, [113] employs a constant energy resolution whereas Nobile *et* al. use a method which accounts for the energy dependence of the resolution. Secondly, for the CDMS-Si excess signal, reference [113] uses a 3 keV bin width everywhere, except in Figure 2 of that paper where they use the same 2 keV bin width as reference [112]. Other than in Figure 2, which yields comparable results to those obtained by Nobile *et* al., the two analyses cannot be compared since they employ different binning strategies. Frandsen *et* al. demonstrate that the CDMS-Si data points are not entirely excluded by XENON10/100 bounds in the IC case. However, disagreement is still found to exist between the CDMS-Si measurements and the XENON100 constraint which is independent of uncertainties in the distribution of DM in the halo. As it so happens, IV couplings are found to reduce these tensions.

The techniques of a halo-indpendent analysis were extendend by Bozorgnia *et* al. to include the possibility of inelastic couplings in order to test the compatibility of the DAMA modulation signal with the XENON100 unmodulated constraint [114]. As will be made clear in Chapter 6, the introduction of inelastic couplings to a halo-independent analysis is a non-trivial procedure because there no longer exists a unique relationship between the nuclear recoil energy and v_{min}. In order to avoid astrophysical uncertainties in an inelastic framework, reference [114] devises three halo-independent tests, the most important being their so-called “shape-test”. In a sense, the “shape-test” quantifies deviations between the results obtained in converting to v_{min}-space for the two possible nuclear recoil energies corresponding to a particular value of v_{min}. Bozorgnia *et* al. were able to conclude that an inelastic DM interpretation of the DAMA modulation signal is in strong contention with constraints placed by XENON100. Unfortunately, a DM hypothesis which contains both inelastic and IV couplings was not considered.

Finally, we briefly mention a generalized halo-independent description of direct detection data formulated by Nobile *et* al. which extends the analysis to any type of WIMP-nucleon interaction [115]. The method is applied to DM with magnetic moment interactions. It should be noted however that this analysis does not allow for inelastic WIMP-nucleon scattering because it assumes a trivial relation between v_{min} and the nuclear recoil energy E_{nr}. The main purpose of their generalization was to provide a halo-indpendent analysis of models whose DM interactions depend on arbitrary functions of the DM particle velocity and the nuclear recoil energy, as is the case for magnet dipole and anapole DM.

Chapter 5

Searching the Dark Matter Parameter Space

The main purpose of direct detection experiments is two-fold: to confirm the existence of a DM particle, and to determine the values of parameters (mass, cross section, etc. . .) in the relevant model. Naturally, one might ask the following questions: how do we extract and establish the presence of an interacting DM particle from the tentative signals arising at possibly multiple detection experiments, and what procedure do we impose on the data in order to assign values to the various parameters of the theory?

Typically, tests on the compatibility of WIMP searches are done within the confines of parameter space plots. For standard models of dark matter with or without minimal extensions, this usually involves evaluating each experiment separately and displaying the resulting contours in a single σ-M_{DM} plot. Such an analysis will be referred to as the standard formalism. In the standard formalism, the robustness of a model is judged qualitatively (essentially "by-eye") on two factors: whether ROIs for competing positive-signals exhibit marginal overlap, and whether these regions elude null constraints. As is suggested in [109], such a procedure is less than ideal because it fails to address the key question regarding the existence of DM, which inherently requires an assesment of the astrophysical uncertainties involved. Moreover, given the substantial amount of processing that enters parameter space plots, it is complicated to judge the impact that astrophysical unknowns have on experimental findings, as well as uncertainties arising from nuclear, atomic, and particle physics. To complicate matters further, a misunderstanding of background sources and noise in a detector can negate the claim of an excess signal [50, 116] and/or significantly alter theoretical predictions.

Despite these downsides, parameter space plots are a crucial first step in understanding the direct detection of dark matter. For example, a halo-independent analysis requires knowledge of parameter values (except for the WIMP-nucleon cross section) in order to test the regions of v_{min}-space probed by DM experiments. Furthermore, a standard formalism analysis may be improved by better quantifying the values of model parameters through the introduction of a chi-squared test. As it turns out, the standard formalism is convienent not only because it allows for the determination of parameter values, but because it makes manifest the model-dependencies of the different experimental results. Consequently, the standard and halo-independent formalisms should be viewed as complements to one another.

In the following chapter, we aim to investigate the results of direct detection experiments under the DM hypothesis through a series of parameter space plots. By minimizing an appropriate chi-squared statistic, our goal is to better quantify the "goodness" of a number of DM models including: SI, SD and combined, IC and IV, elastic and inelastic, MD, and possible combinations of these. Also, we plan to determine the best-fit values of the various parameters and wish to explore the effects of varying astrophysical parameters such as the Galactic escape velocity v_{max}, the Sun's circular velocity v_0, and the local DM density ρ_{DM}.

Chapter 5 is layed out as follows. An overview of the plot definitions and method used to obtain benchmark points in the parameter space for various models is outlined in section 5.1. We proceed in section 5.2 by reviewing the results for standard SI and SD DM. In section 5.3 we explore the effects of varying the various astrophysical parameters on the positive-signal regions of interest and exclusion curves. Sections 5.4 - 5.6 test the DM hypothesis under extensions of the standard model, the most important being the introduction of IV couplings.

5.1 Methodology

A standard minimization scheme on the total χ^2 value for positive-signal data is performed in order to determine benchmark points of various phenomonological scenarios. The plots will focus

Object	Label	Description
	DAMA	ROI for DAMA
	CoGeNT	ROI for CoGeNT
	CRESST	ROI for CRESST-II
	Xe10	95.4% and 99.7% upper limits for XENON10
	Xe100	95.4% and 99.7% upper limits for XENON100
	CDMS-Ge	95.4% and 99.7% upper limits for CDMS-Ge
	CDMS-Si	95.4% and 99.7% upper limits for CDMS-Si
	SIMPLE	95.4% and 99.7% upper limits for SIMPLE
	EDEL	95.4% and 99.7% upper limits EDELWEISS
		benchmark point

TABLE 5.1: Definitions for the objects of the parameter space plots including the colour scheme, and labels. The solid (dashed) lines correspond to the 95.4% (99.7%) CL.

on parameter space in the σ_p^{SI}-M_{DM} plane for which we investigate the effects of SI, SD, elastic, inelastic, IV, IC, and momentum dependent couplings.

In the plots to follow, the exclusion curves of null experiments are represented by solid (dashed) lines corresponding to 95.4% (99.7%) CL. The best- fit regions for the positive-signal experiments are indicated by three solid contours corresponding to 68.3%, 95.4% and 99.7% confidence intervals with $<$ 68.3% CL filled in by the lightest shade of the appropriate colour. Table 5.1 organizes the colour scheme, label, and description for the objects in the plots of this chapter.

Our total chi-squared statistic χ^2_{tot} is defined as the sum of χ^2s corresponding to the positive-signal experiments being analysed. For example, if our analysis includes DAMA, CoGeNT and CRESST, then $\chi^2_{tot} = \chi^2_{DAMA} + \chi^2_{CoGeNT} + \chi^2_{CRESST}$. The total χ^2 is minimized in order to fix values of the parameters not included in the phase space of the plot. Confidence levels and contours are then computed using the individual χ^2 or upper limit methodologies reported in Chapter 3. Lastly, each plot includes a legend which displays the values of Galactic escape velocity, local circular velocity, DM density and sodium quenching factor used, as well as the values of additional model parameters and that of χ^2_{tot}. For cases which involve a MD coupling, the value of n appearing in the form factor $(q^2/q_0^2)^n$ is included, otherwise it is assumed to be zero.

5.2 Standard dark matter

Firstly, consider fitting the direct detection data in terms of elastic, IC ($f_n = f_p$) SI DM scattering. Figure 5.1 shows the results in σ_p^{SI}-M_{DM} space where we have taken mean values for the astrophysical parameters, and a constant sodium quenching factor of $Q_{\rm Na} = 0.3$. A minimization of the total chi-squared yields a benchmark point of $M_{DM} = 8.7$ GeV and $\sigma_p^{SI} = 3.3 \times 10^{-41}$ cm^2 with $\chi^2_{tot} = 167.9$. Since a combined fit for DAMA, unmodulated CoGeNT, and CRESST involves 64 data points, a two parameter model implies an optimal total chi-squared of $\chi^2_{opt} \sim 62$. As a result, the gross discrepancy in chi-squared values leads to the conclusion that standard SI DM provides a poor model fit to all the data.

Furthermore, a qualitative analysis reveals a number of difficulties in the standard DM framework. First off, all positive-signal ROIs are excluded by one or more null experimental constraints by (at the very least) the 95.4% CL. On the compatibility of positive-signal experiments, there is no overlap between the favoured regions of DAMA and CoGeNT, CoGeNT and CRESST, and only marginal agreement between DAMA and CRESST. Additionally, the benchmark point misrepresents the DAMA and CRESST best-fit points, and is excluded by both XENON100 and CDMS-Ge. The strongest constraint arises from XENON100 which essentially excludes all parameter space relevant for low-mass direct detection in the standard scenario, that is $M_{DM} > 8$ GeV and $\sigma_p^{SI} > 10^{-41.3}$ cm^2.

Figures 5.2 and 5.3 investigate standard elastic, SD DM scattering as an explanation for experimental data. Unlike the case of SI DM, "standard" here does not mean that the spin-dependent WIMP-nucleon couplings (a_n and a_p) are assumed to be equal. In the literature, standard in this context means that we either assume a purely protonic spin interaction by setting $a_n = 0$ ($a_p = 1$), or a purely neutronic spin interaction by setting $a_p = 0$ ($a_n = 1$). Since SD interactions between nuclei and DM are only possible for nuclei that carry spin, a CRESST ROI is not present given that none of its nuclei contain any odd spin. As mentioned in section 2.1.2, we use the structure functions $S_{00}(q^2)$, $S_{01}(q^2)$, and $S_{11}(q^2)$ of reference [29]. For nuclei where multiple groups have published results on the strucutre functions, we implement the results of Russel and Dean for ^{23}Na and ^{131}Xe, and Russel *et* al. for ^{29}Si and ^{73}Ge. Also, for ^{129}Xe the

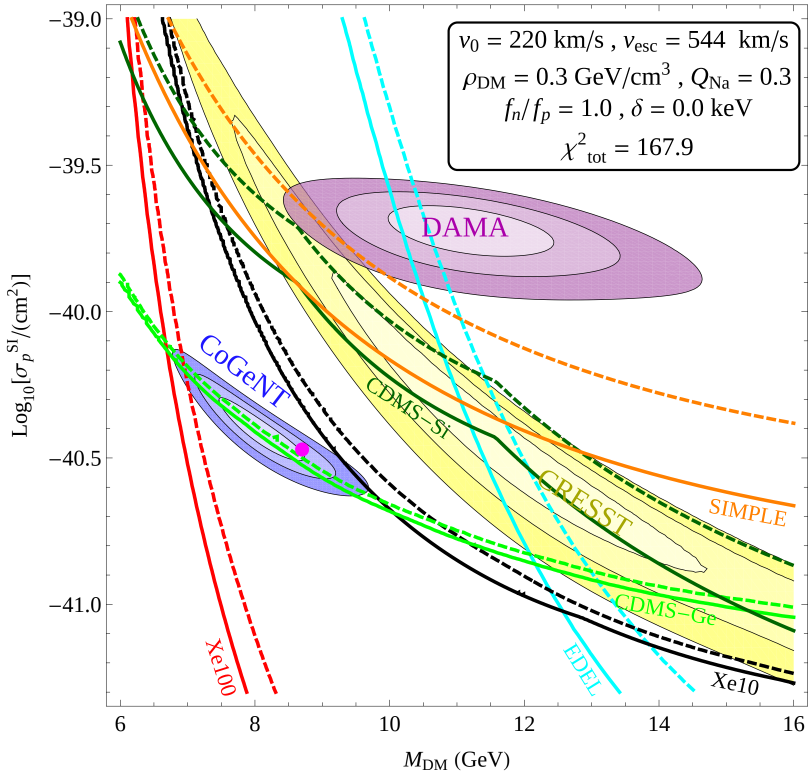

FIGURE 5.1: Elastic isospin-conserving spin-independent DM fit to the experimental data in the σ_p^{SI}-M_{DM} plane with $f_n/f_p = 1.0$ and $\delta = 0.0$ keV.

structure functions that contain the full parameterizations for the Bonn A potential are used.[1]

One of the lightest target medium, ^{19}F, is the isotope that has the greatest sensitivity to spin-dependent DM-nucleon couplings. The reason being that its spin matrix element is not quenched, and the various isospin channels add coherently [118], whereas for example, the spin matrix elements of ^{23}Na and ^{29}Si are somewhat suppressed. Despite fluorine-19 amounting to only a small percentage of the total SIMPLE target medium, Figure 5.2 clearly demonstrates its role as the most constraining null experiment under SD interactions ruling out at the 95.4% CL $\sigma_p^{SD} > 10^{-37}$ cm^2 for $M_{DM} = 10$ GeV.

We find the benchmark point for protonic spin-dependent DM to be $M_{DM} = 11.2$ GeV and $\sigma_p^{SD} = 7.4 \times 10^{-37}$ cm^2. As is the case with SI DM, there is no compelling evidence that SD couplings alone are capable of explaining the experimental picture, since in this case $\chi^2_{opt} \sim 56$ and we obtain a total chi-squared of $\chi^2_{tot} = 226.9$. The qualitative picture is also similar. The DAMA and CoGeNT ROIs are in disagreement showing no overlap, and are excluded entirely by

[1]Computation of the structure functions rely on residual nuclear interactions which require knowledge of the nucleon-nucleon potential. In reference [117], Ressell and Dean consider two such possibilities in their analysis: the Bonn A and the Nijmegen II potential. Results show that the difference between structure functions which use the Bonn A and Nijmegen-II based nuclear Hamiltonians is small.

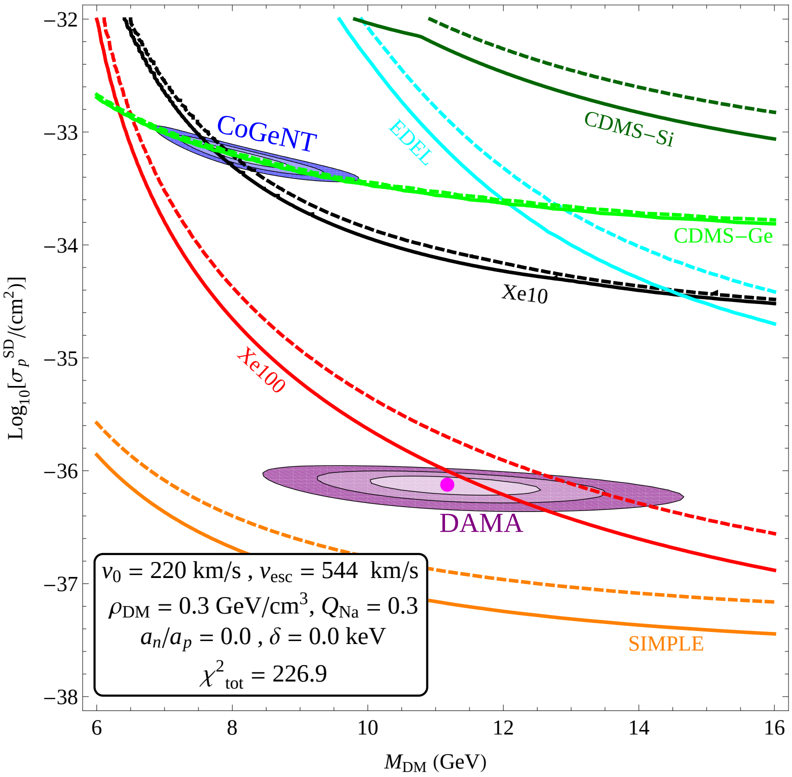

FIGURE 5.2: Elastic purely protonic spin-dependent DM fit to the experimental data in the σ_p^{SD}-M_{DM} plane with $a_n = 0.0$, $a_p = 1.0$ and $\delta = 0.0$ keV.

one or more null constraints. In fact, the CoGeNT best-fit point corresponds to a cross section which is approximately three orders of magnitude larger than that of DAMA.

On the other hand, an analysis of neutronic spin-dependent interactions reveals a more favourable scenario. For $a_p = 0$, a fit to DAMA and CoGeNT data yields a benchmark point of $M_{DM} = 8.0$ GeV and $\sigma_n^{SD} = 7.6 \times 10^{-36}$ cm^2, corresponding to a total chi-squared of $\chi^2_{tot} = 138.5$. The improvement in the total chi-squared over purely protonic SD scattering is substantial however, it remains significantly larger than the optimal chi-squared value of 56 indicating that the model does not fully encapsulate the data. Again, null constraints exclude all positive-signal ROIs. In contrast to protonic SD DM, Figure 5.3 demonstrates that purely neutronic interactions result in a relative weakening of the SIMPLE upper limit compared to constraints placed by the XENON and CDMS-II collaborations. Figures 5.2 and 5.3 clearly show how a change in the DM couplings to protons and neutrons can significantly alter the experimental picture in the σ_p^{SD}-M_{DM} plane. One might surmise the possibility that the DAMA and CoGeNT ROIs might be brought into agreement in the SD scenario through a tuning of SD couplings. We perform such an investigation in section 5.5.

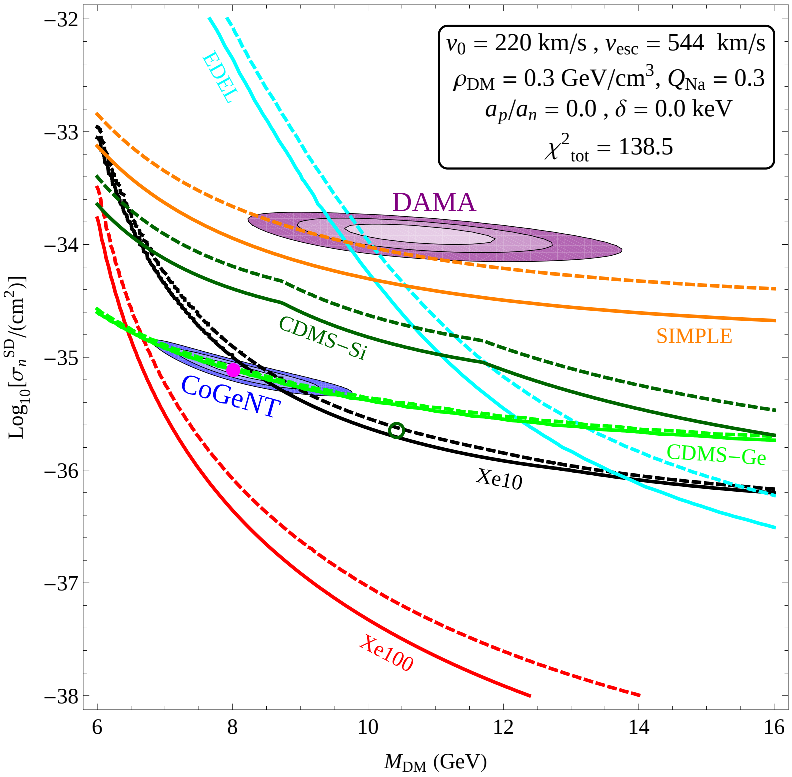

FIGURE 5.3: Elastic purely neutronic spin-dependent DM fit to the experimental data in the σ_p^{SD}-M_{DM} plane with $a_n = 1.0$, $a_p = 0.0$ and $\delta = 0.0$ keV.

5.3 Astrophysical uncertainties

Let us examine the uncertainties surrounding astrophysical parameters, and the effects that varying them have on the DM parameter space. Considered here are the following quantities that enter into the calculation of DM event rates: the Galactic escape velocity v_{esc}, the Sun's circular velocity with respect to the Galactic rest frame v_0, and the local DM density ρ_{DM}. The arguments here are in a similar vein to those discussed in reference [119].

First off, perhaps the most detailed determination of v_{esc} comes from the RAVE survey [33] which places a 90% confidence interval of $495 < v_{esc} < 608$ km/s on the escape velocity with median likelihood value 544 km/s.[2] Our knowledge on the distribution of mass outside the solar vicinity in terms of a local dynamical quantity comes entirely from the Galactic escape velocity. Furthermore, v_{esc} has immediate consequences for the number of events expected at a given direct detection experiment. Qualitatively speaking, lower values of the Galactic escape velocity correspond to a smaller number of DM particles in the halo available for scattering. As a result,

[2]After the bulk of this work was completed, the RAVE survey released an update on the Galactic escape velocity [120]. A best estimate of the Galactic escape velocity is reported to be 537^{+59}_{-43} km/s.

in order to produce the same number of events at an experiment requires that the DM-nucleon cross section be larger.

Figure 5.4 shows the 95.4% CL exclusion curves and positive-signal contours in σ_p^{SI}-M_{DM} space under standard elastic DM for escape velocities 495 km/s (dashed) and 608 km/s (solid). The benchmark point corresponding to v_{esc} = 498 km/s is represented by an unfilled, dashed, magenta circle. Evidently, the qualitative predictions are consistent with phenomenological results: for a fixed value of the DM mass, a weakening of upper limits occurs as we move to lower values of the Galactic escape velocity . Further observation reveals that the change in σ_p^{SI} required to produce the correct number of events becomes greater as we move to smaller values of M_{DM}. The explanation for this is rather straightforward and relies on the fact that a signal's characteristics depends chiefly on the recoil energy deposited. If we increase the Galactic escape velocity, then the average speed of the WIMPs in the halo will also increase. In principle the nuclear recoil energy will depend on the intial kinetic energy of the DM particle in a simple manner. Therefore, in order to hold the kinetic energy fixed as the average speed of the WIMPs increases requires a shift to smaller DM masses. However, since the Maxwell-Boltzmann velocity distribution is exponentially suppressed at high velocities, the effect of this increase will be negligible unless v_{min} is close to v_{max}, which is the case for light DM (see equation (2.9)). Thus the resulting shift in exclusion curves is exaggerated at smaller DM masses. For the same reasons as light DM, inelastic DM will cause larger shifts in the exclusion curves since increasing the mass splitting δ has the effect of bringing v_{min} closer to v_{esc}.

A slight shift to lower masses is also observed in the positive-signal ROI as we move to larger values of v_{esc}. Interestingly, a small decrease in the total chi-squared value ($\Delta\chi^2_{tot} \sim 2$) occurs as we increase v_{esc} however, this improvement comes at the cost of a relative strengthening of the null constraints. As a result, we conclude that variations in the Galactic escape velocity have little effect on the global fit to direct detection data, and although it is possible to weaken upper limits by decreasing v_{esc}, the relief this provides at the one sigma level in v_{esc} leaves the overall tension unchanged.

Next, we consider uncertainties associated with the Sun's circular velocity which takes on a fiducial value of v_0 = 220 km/s. Attempts to determine the rotational speed of the local standard of rest are numerous and have produced an array of results. Some of these methods

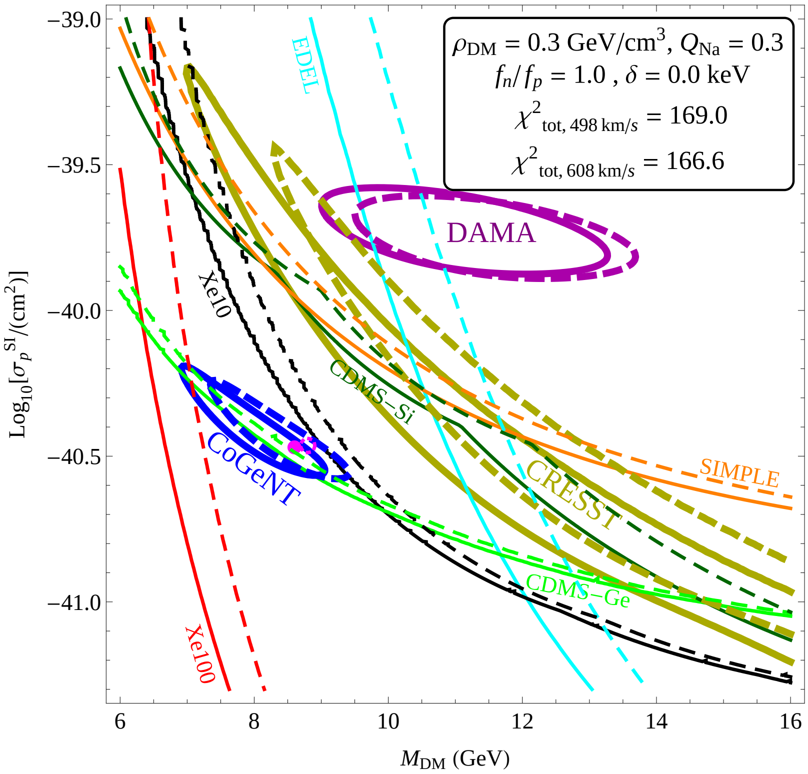

FIGURE 5.4: Elastic isospin-conserving spin-independent DM fit to the experimental data in the σ_p^{SI}-M_{DM} plane for different values of the Galactic escape velocity, v_{esc}. Solid (dashed) contours correspond to $v_{esc} = 608$ (498) km/s.

include: extracting v_0 from measurements on the apparent motion of Sgr A* (the compact radio source at the centre of our Galaxy), measurements of Galactic parameters for masers in high mass star-forming regions, and an analysis of the GD-1 stellar stream. Reference [119] combines the known results for v_0 to obtain a limit on the Sun's circular velocity of 195 km/s $< v_0 <$ 255 km/s, which we implement here.

Figure 5.5 demonstrates, in the standard elastic σ_p^{SI}-M_{DM} parameter space, the dependence of the 90% confidence intervals on the Sun's circular velocity for values $v_0 = 195$ km/s (dashed) and $v_0 = 255$ km/s (solid). Immediately, we see that generally the effects of varying v_0 are more pronouced than in the case of the Galactic escape velocity which, as we shall see, is to be expected. A decrease in the Sun's circular velocity results in an a shift to larger values of the WIMP mass and consequently, a worsening in the tension between null constraints and positive-signal ROIs. Again, we obtain only small variations in the total chi-squared when changes in v_0 are applied.

v_0 enters into the calculation of DM event rates in two ways. Firstly, it relates the Galactic frame to the Earth frame through the equation $\vec{v}_e = (\vec{v}_0 + \vec{v}_{\circledast}) + \vec{v}_{\oplus}$, where $\vec{v}_{\odot} = \vec{v}_0 + \vec{v}_{\circledast}$ is

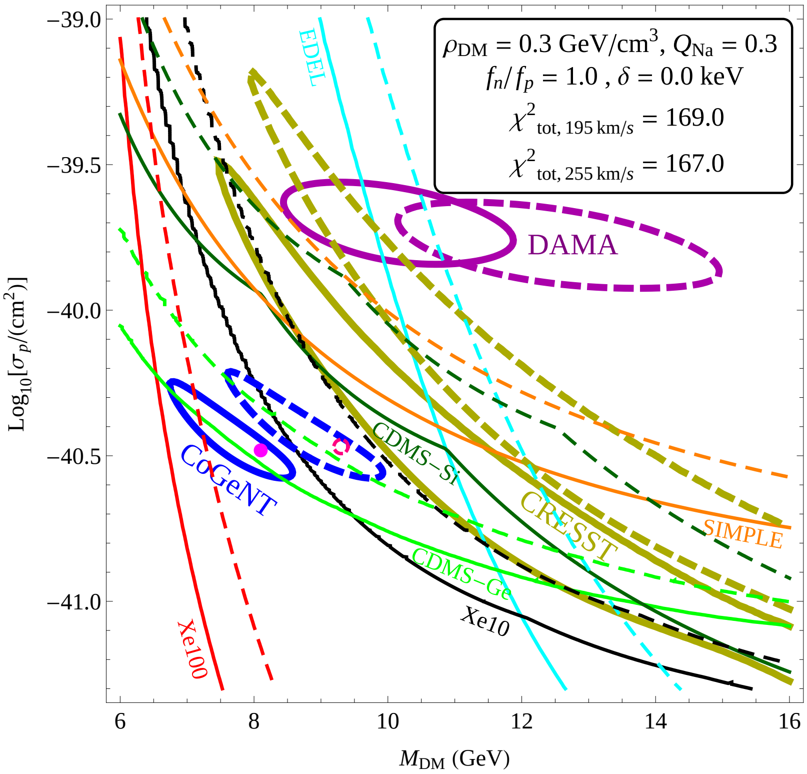

FIGURE 5.5: Elastic isospin-conserving spin-independent DM fit to the experimental data in the σ_p^{SI}-M_{DM} plane for different values of the Sun's circular velocity, v_0. Solid (dashed) contours correspond to $v_0 = 255$ (195) km/s.

the total velocity of the Sun about the centre of the Galaxy with $\vec{v}_{\circledast}$ the Sun's peculiar velocity, and $\vec{v}_{\oplus}$ is the Earth's velocity relative to the Sun's rest frame. Since the velocity that enters the halo distribution is $\vec{v} + \vec{v}_e$, increasing v_0 has the effect of increasing the number of WIMPs with speeds above v_{min} and therefore capable of scattering. The cross-section must decrease in order to compensate for this in the predicted DM rates. Secondly, it enters into the DM velocity distribution as a dispersion relation. A larger v_0 means an increase in the range of velocites allowed in the halo and thus increases the number of potential scattering WIMPs. Because changes in v_0 affect the entire velocity distribution, as opposed to just the exponential tail in the case of v_{esc}, we expect larger variations with respect to v_0.

Finally, we comment on the local DM density in our Galaxy whose value is usually taken to be $\rho_{DM} = 0.3$ GeV/cm^3. A wide range of values for ρ_{DM} (sometimes with large uncertainties) exists in the current literature. For instance, Weber and de Boer in their study [127] discover that $\rho_{DM} = 0.3 \pm 0.1$ GeV/cm^2. The most precise claim to date comes from an analysis by Catena and Ullio [121] where it is reported that $\rho_{DM} = (0.389 \pm 0.025)$ GeV/cm^2. More recently, Nesti and Salucci [122] find that $\rho_{DM} = (0.43 \pm 0.11 \pm 0.10)$ GeV/cm^2. In reference [123], Bidin *et* al. assert the claim that the solar vicinity is absent of any DM, at odds with all other measurements.[3] Despite this perplexing picture, varying the local dark matter density does not affect the compatibility between positive-signal ROIs with eachother or null constraints since ρ_{DM} is independent of experiment specific quantities. Given that the DM density and cross section enter the DM event rate as $\rho_{DM} \times \sigma_{n,p}^{SI,SD}$, increases (decreases) in DM density are offset by decreases (increases) in cross-section equally for all experiments.

5.4 Spin-independent isospin-violating dark matter

The common assumption that DM-nucleon couplings be isospin-conserving is neither well-motivated in certain cases, nor a generic feature of theories involving WIMPs. For example, in the constrained minimal supersymmetric model, it is the result of a number of non-trivial coincidences that a spin-independent (largely) isospin-conserving scattering matrix arises [108]. Furthermore, the realisation of a low mass ($<$ 100 GeV) DM candidate within this framework, and those similar to it, is difficult to achieve.

In contrast, the argument that DM be IV is supported by an abundance of models in which isospin violation naturally occurs. Fermionic (Dirac or Majorana) and scalar (complex or real) DM that interacts with SM particles through the quark portal will generally break isospin symmetry, since the quark operator matrix elements will be different for up and down quarks [125]. Additionally, DM interactions which are mediated by new gauge bosons under a hidden U(1) gauge symmetry will violate isospin if there exists a small kinetic mixing with the SM hypercharge [126].

Given that we are interested in a general model of DM irrespective of the underlying microphysical theory, the DM-nucleon couplings ratio f_n/f_p is treated as a free parameter whose value we assign through a confluence of the data. Prior to computing confidence intervals for the IVDM phase space, let us try to better understand how a particular choice of f_n/f_p can affect the predicted DM event rate in a given target material. Recall that the DM-nucleus SI cross

[3]This null DM density conclusion has come under intense scrutiny, in particular by Bovy and Tremaine [124], where it is pointed out that a number of arbitrary assumptions afflict Bidin *et* al.'s result.

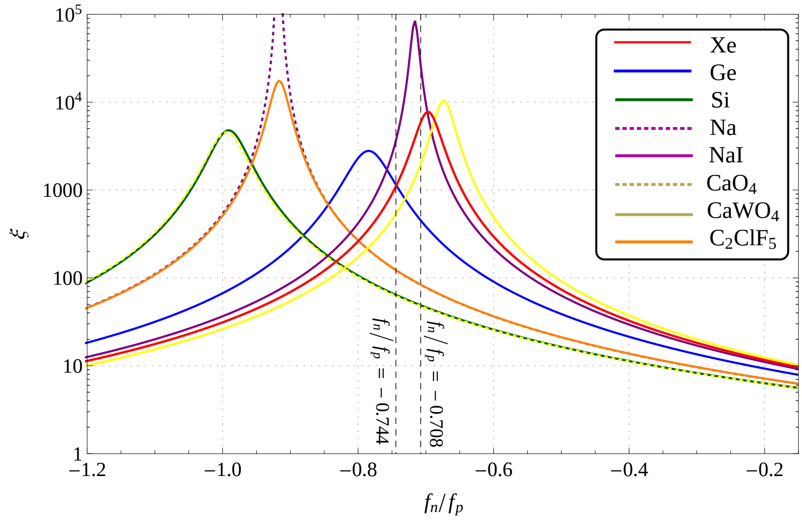

FIGURE 5.6: Graphing the function $\xi(f_n/f_p)$ of equation (2.22) for various target material and for DM mass $M_{DM} = 10$ GeV. Vertical dashed lines correspond to the elastic SI benchmark value of the isospin violation ratio $f_n/f_p = -0.708$, and the value $f_n/f_p = -0.744$ for which larger f_n/f_p weaken the XENON100 bound relative the CoGeNT ROI.

section σ_0^{SI} is proportional to the following expression:

$$\begin{aligned} \sigma_0^{SI} &\propto \frac{\left(f_p Z + f_n(A-Z)\right)^2}{f_p^2} \\ \Longrightarrow \sigma_0^{SI} &\propto \left(Z + \frac{f_n}{f_p}(A-Z)\right)^2, \end{aligned} \tag{5.1}$$

which captures the cross section's sensitivity towards the different number of protons and neutrons comprising the nucleus. Evidently, for a carefull choice of f_n/f_p it is possible for the DM-proton and DM-neutron components to completely cancel one another. Under the assumption that the nucleus has no additional isotopes, the predicted event rate for that nucleus would be zero. Of course, since most nuclei have known isotopes, and many detectors are composed of multiple element types, for real world scenarios it is not possible to tune the coupling parameters so that a particular detector predicts zero WIMP events. On the other hand, it is conceivable that minor cancellations might be possible for the right choice of isospin-violation ratio at a given experiment, a result which could greatly weaken constraints since a higher DM-nucleon cross section would be required to produce the observed number of events.

Figure 5.6 explores the interplay between various experiments for different values of f_n/f_p, and the amount to which varying f_n/f_p can amplify the SI DM-proton cross section under an IV hypothesis relative the IC case for various target medium. This is accomplished by plotting the proportionality factor which appears in equation (2.22) as a function of f_n/f_p for a WIMP mass of $M_{DM} = 10$ GeV. It is found that changes in $\xi(f_n/f_p)$ for different low WIMP masses are negligible.

In order to alleviate the tensions posed by standard SI DM using IV couplings, the cancellations within the DM-nucleus cross section must boost the various σ_p^{SI} relative the standard case in such a way that procures compatibility. Thus an ideal f_n/f_p would be one that causes large upwards σ_p^{SI} shifts in the CoGeNT ROI and even more so in the XENON exclusion curves relative that experienced by DAMA. For multi-element detectors where large mass differences between nuclei exist, event rate predictions are largely influenced by the lighter masses. Hence for DAMA and CRESST, it is more appropriate to consider the $\xi(f_n/f_p)$ functions for Na and CaO_4 in place of NaI and $CaWO_4$, respectively. Unfortunately, for experiments which use identical target material, or ones which produce similar ξ functions, it is not possible to improve existing conflicts via isospin violation alone, as is the case for CoGeNT and CDMS-Ge, DAMA and SIMPLE, and CRESST-II and CDMS-Si. Figure 5.6 shows that in the range $-0.744 < f_n/f_p \lesssim -0.5$, $\xi(f_n/f_p)$ satisfies the minimal criteria for possible agreement. Moreover, since $\xi(f_n/f_p)$ for xenon attains its maximum near $f_n/f_p = -0.7$ and within the optimal range of values, we expect IVDM to find its benchmark value around $f_n/f_p = -0.7$.

Figure 5.7 plots the confidence levels for elastic IV SI DM in the σ_p^{SI}-M_{DM} plane for DM-nucleon coupling ratio $f_n/f_p = -0.708$. The benchmark values for the WIMP mass and cross section are found to be $M_{DM} = 8.0$ GeV and $\sigma_p^{SI} = 1.7 \times 10^{-38}$ cm^2 corresponding to a total chi-squared of $\chi^2_{tot} = 97.4$. Improvements to the global fit of experimental data can be summarised as follows:

- a large reduction in the total chi-squared relative the IC case is observed ($\Delta\chi^2_{tot} = 70.5$),
- marginal overlap is created between CoGeNT and DAMA ROIs,
- CoGeNT is brought into better agreement with CRESST,
- a weakening of the XENON100 bound creates allowed regions of phase space for positive-signals at the 99.7% CL, and supports the benchmark point and a majority of the CoGeNT ROI at the 95.4% CL,

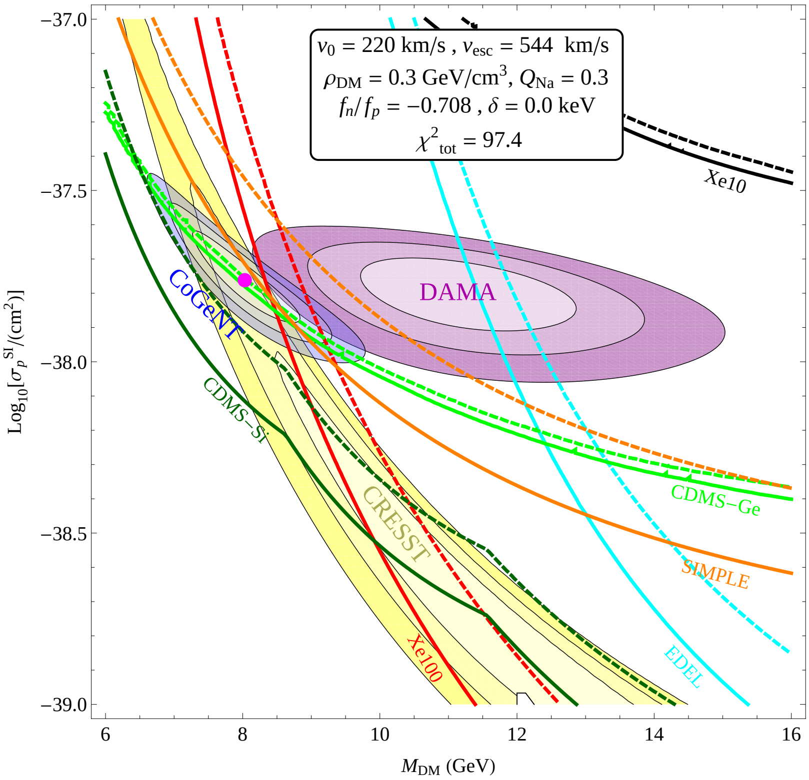

Figure 5.7: Elastic isospin-violating spin-independent DM fit to the experimental data in the σ_p^{SI}-M_{DM} plane with $f_n/f_p = -0.708$ and $\delta = 0.0$ keV.

- the XENON10 constraint is substantially reduced in comparison to other experiments.

In spite of all this, the lower mass region supported by DAMA fails to cohere to the CRESST ROI for this particular choice of f_n/f_p. Additionally, a lack of improvement in the CDMS-Si exclusion curve makes it the most constraining null experiment for IVDM ruling out entirely the CoGeNT and DAMA signals at the 3σ level. Such a result is anticipated since in Figure 5.6, silicon takes on the smallest value of $\xi(f_n/f_p)$ when $f_n/f_p = -0.708$ and resultingly, undergoes the smallest shift to larger DM-proton cross sections.

Before we test further extensions of the DM model on direct detection data, consider varying the sodium quenching factor. It is widely known that larger values of $Q_{\rm Na}$ have the effect of pushing the DAMA ROI to lower WIMP masses, thus improving the fit. The reason for this being that the combination $Q_{\rm Na}M_{DM}$ remains essentially constant. Figure 5.8 investigates SI IV DM in the σ_p^{SI}-M_{DM} plane for an upper limit saturated sodium quenching factor of $Q_{\rm Na} = 0.4$. The benchmark point for this scenario corresponds to $M_{DM} = 8.1$ GeV, $\sigma_p^{SI} = 1.6 \times 10^{-38}$ cm^2, and $f_n/f_p = -0.705$ with a total chi-squared of $\chi^2_{tot} = 83.1$. By setting $Q_{\rm Na} = 0.4$, one

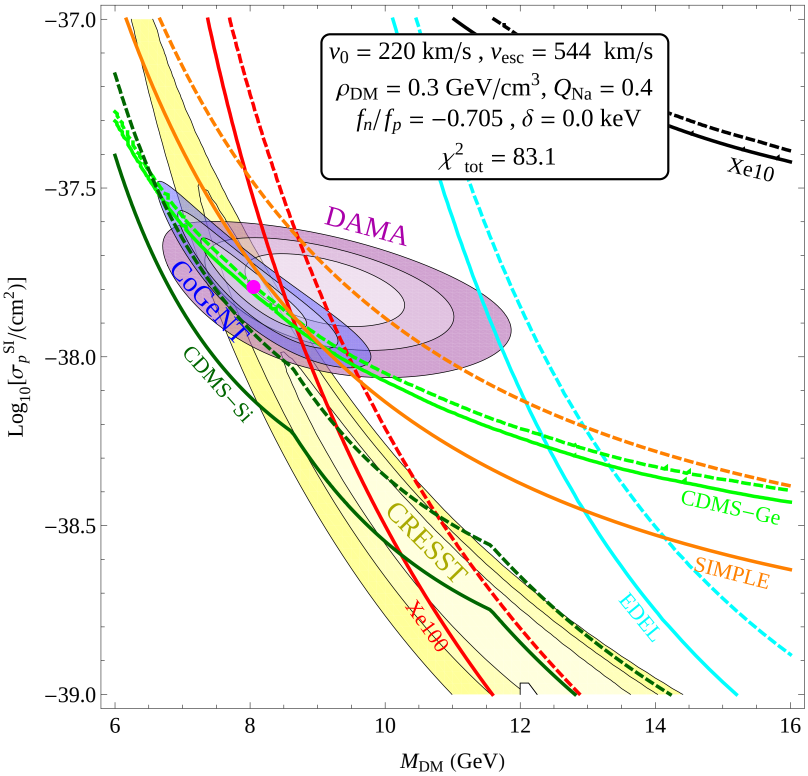

FIGURE 5.8: Elastic isospin-violating spin-independent DM fit to the experimental data in the σ_p^{SI}-M_{DM} plane for the upper limit value of the sodium quenching factor, $Q_{\rm Na} = 0.4$, with $f_n/f_p = -0.705$ and $\delta = 0.0$ keV.

obtains remarkable consistency between CoGeNT and DAMA, a mutually compatible region within the 95.4% confidence intervals of all three positive-signal experiments, and parts of the DAMA claim which extend to regions of parameter space allowed by CDMS-Si. The first two points are reflected in the further reduction of the total chi-squared value.

5.4.1 Inelastic scattering

As mentioned in Chapter 4, studies have shown that the introduction of inelastic couplings to the DM model might serve as a way to help alleviate tensions concerning the DAMA and CoGeNT best-fit regions. Such a scenario involves, via up-scattering, the excitation of the DM particle χ to a state χ^* with mass difference $\delta = M_{\chi^*} - M_\chi$. In priciple, first investigated in reference [128], it is possible instead for down-scattering to occur in which case the mass splitting parameter satisfies $\delta < 0$. For clarity, we refer to the up-scattering and down-scattering cases as endothermic DM and exothermic DM, respectively.

Early results for inelastic DM focused on large mass splittings $\mathcal{O}(100)$ keV comparable to the kinetic energy of the incoming DM particle. However, such models favour large WIMP masses and are heavily constrained by null bounds [129, 130]. In the same spirit as Farina *et* al. [55], our analysis of inelastic DM concentrates on mass splittings $\mathcal{O}(10)$ keV.

In an inelastic scattering scenario, elastic scattering is assumed to be forbidden or highly suppressed. As a result, the change in scattering kinematics alters on a fundamental level how inelastic DM particles are detected in ground-based experiments. Recall the minimum velocity requirement of equation (2.2). In the endothermic case, a simple kinematic argument reveals that WIMPs with speeds less than $\sqrt{2\delta/\mu_N}$ are not capable of scattering whatsoever since the insufficient amount of kinetic energy will prevent excitations to the more massive state. In that case, the range of velocities available for heavier target material will be greater compared to lighter nuclei and consequently, there will be a larger fraction of WIMPs in the halo available for scattering. Furthermore, endothermic scattering results in a differential event rate which reaches its peak at higher nuclear recoil energies, as opposed to the charateristic exponetially decaying spectrum of elastic DM. For that reason, signals are suppressed at low recoil energies. Finally, signals which support an annual modulation are significantly enhanced.[4]

As for exothermic DM, v_{min} is minimized for recoil energies E_{nr} on the order of δ/M_N. Accordingly, experiments with light nuclei and low thresholds will be more sensitive to exothermic inelastic scattering.

The results for allowing the mass splitting parameter δ to float are presented in Figure 5.9 for IVDM in the σ_p^{SI}-M_{DM} plane. A minimized total chi-squared of $\chi^2_{tot} = 96.2$ is obtained for the benchmark point $M_{DM} = 8.6$ GeV, $\sigma_p^{SI} = 3.0 \times 10^{-38}$ cm^2, $f_n/f_p = -0.715$, and $\delta = 3.25$ keV. Relative the elastic IV model, a small improvement in the likeness between the CoGeNT, CRESST, and DAMA regions is realised. By the same token, there exists a triangular section slightly below the benchmark point which is accomodated by every 3σ exclusion curve (with the exception of the CDMS-Si bound) and simultaneosly explains all the positive-signal data. Furthermore, the upper bound placed by SIMPLE is moderately weakened, and part of the

[4] In the inelastic scenario, modulation signals may be enhanced due to the fact that a higher velocity component of the DM velocity distribution is probed, and in this region quantities undergo drastic changes as a function of velocity.

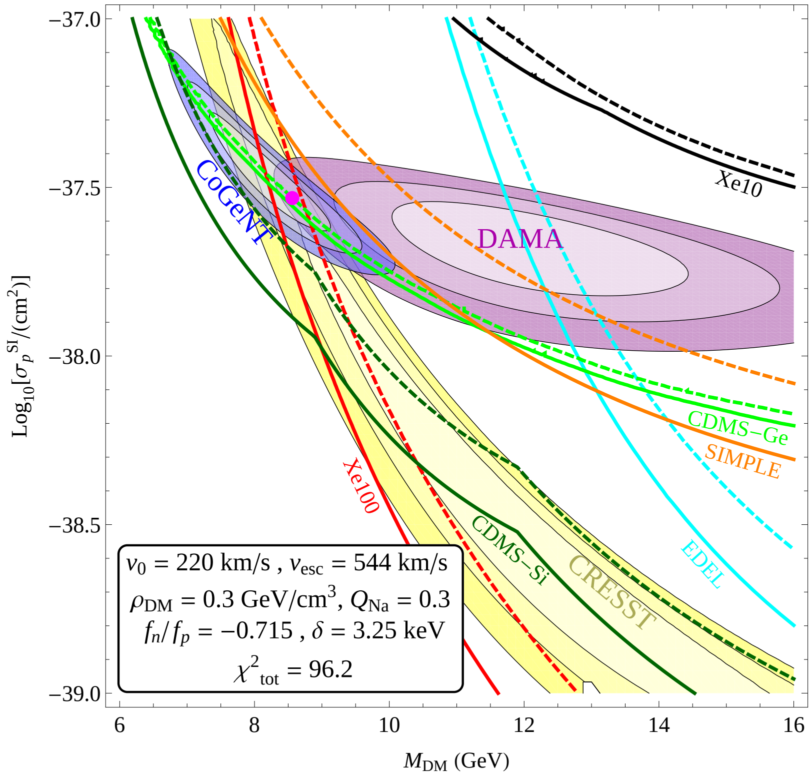

FIGURE 5.9: Inelastic isospin-violating spin-independent DM fit to the experimental data in the σ_p^{SI}-M_{DM} plane with $f_n/f_p = -0.715$ and $\delta = 3.25$ keV.

CoGeNT claim no longer comes into conflict with the CDMS-Si 99.7% CL. Unfortunately, a relative strengthening of the XENON100 bound has lead to the benchmark point and large areas of CoGeNT and CRESST becoming excluded.

Given that the reduction in total chi-squared is only of order unity, one might raise the following concern: is adding a mass splitting parameter even justifiable in the first place? After calculating the Bayesian information criterion (BIC) for models with and without inelastic couplings, we find that the insertion of a mass splitting parameter into the differential event rate results in overfitting of the data.[5] Thus inelastic scattering is not favoured under a new understanding of surface event contamination at CoGeNT. This supports the conclusion of reference [106]. For those interested in the effects that a larger, non-trivial value of the mass splitting, or exothermic scattering has on the data, please turn to Appendix B (though the resuts are

[5] The Bayesian Information Criterion is defined for a specific model as follows:

$$BIC = \chi^2 + k \cdot \log n, \tag{5.2}$$

where χ^2 is the minimized value of the models chi-squared, k the number of free parameters to be estimated, and n the number of data points in the observation. In comparing two models, the one that attains a smaller BIC value, is the more favourable model.

not overly enlightening). Also, in Appendix B one can view an inelastic IV SI DM fit to the experimental data in f_n/f_p-δ space where it is evident that for most values of f_n/f_p, there is a corresponding δ that provides a good fit to the CoGeNT data.

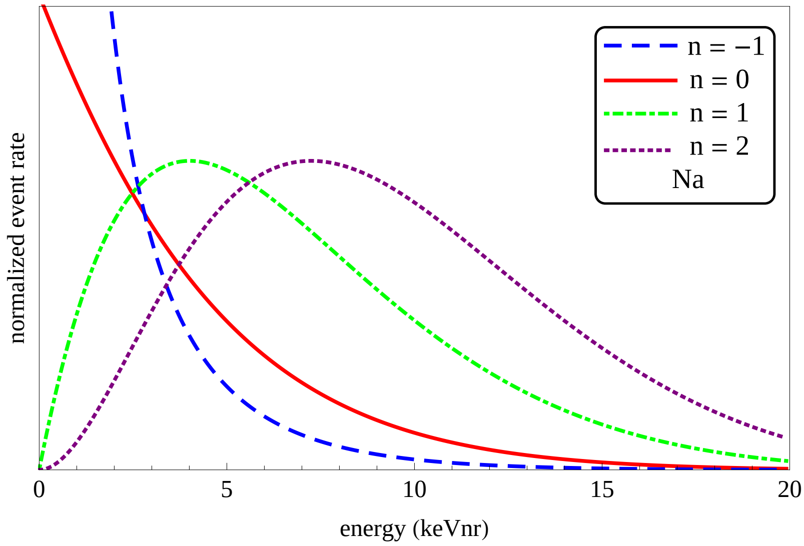

FIGURE 5.10: Differential event rate for momentum-dependent DM scattering on sodium nuclei for DM mass $M_{DM} = 10$ GeV, and with arbirtrary normaliztion. The dashed blue, solid red, dot-dashed green, and dotted purple curves correspond to momentum-dependent scattering with $n = -1$, $n = 0$, $n = 1$, and $n = 2$, respectively.

5.4.2 Momentum-dependent scattering

The motivation and theory behind momentum-dependent scattering in the context of WIMPs was outligned in Chapter 2. A past analysis of DM event rates with generalized IV MD and velocity suppressed form factors revealed marginal improvement over the standard IC and elastic IV cases [55]. In this section, we study the effects of MD scattering in combination with both IV and inelastic couplings.

Before continuing, let's briefly discuss the expectations for a momentum dependent form factor. Figure 5.10 demonstrates the differences between the sodium DM event rate for various MD scattering scenarios in the standard SI model, with arbitrary normalization, and $M_{DM} = 10$ GeV. The results are comparable to that of inelastic DM in that positive powers of q^2 have the effect of suppressing the event spectra at low recoil energies while causing enhancement at higher ones. Analogously, a dependence of the form $1/q^2$ produces an event rate reminiscent of exothermic DM with a larger spectrum at lower recoil energies and a faster decay. As opposed to inelastic DM, the crest in the differential event rate for MD scattering is generated without the tuning of any parameters. Also, MD form factors have the effect of broading the event spectrum over a large range of recoil energies, thereby avoiding the possibility of sharp peaks.

Another interesting feature of $n > 0$ MD scatterng is that increasing the DM mass shifts the event spectrum to higher recoil energies. Thus for experiments that probe higher values of q^2, such as XENON100, a strengthening of the bounds is expected for positive values of n and a weakening in the case of $n = -1$. On the other hand, since CoGeNT explores a higher region of q^2 compared to DAMA, $n > 0$ MD DM has the ability to enhance the CoGeNT ROI relative the DAMA signal. This is an alluring property of MD couplings given that in light of a better understanding of surface event contamination in the CoGeNT data, CoGeNT prefers a WIMP-proton cross section which is smaller than that favoured by DAMA. This is in contrast to observations made prior to the updated surface event acceptance factor (as was the case at the time [55] was published). As a result, the possibility of such an enhancement is highly intriguing.

Figures 5.11, 5.12, and 5.13 show the limts on MD interactions under an inelastic IV scenario for $n = -1$, $n = 1$, and $n = 2$ scattering, respectively. Here, f_n/f_p and δ are enabled to float so as to minimize the total chi-squared corresponding to the positive-signal experiments. The benchmark points and minimized values of chi-squared for the considered models are as follows: for $n = -1$ we obtain a benchmark point of $M_{DM} = 10.5$ GeV, $\sigma_p^{SI} = 1.4 \times 10^{-39}$ cm^2, $f_n/f_p = -0.706$, and $\delta = 8.4$ keV with $\chi^2_{tot} = 101.1$, for $n = 1$ we have $M_{DM} = 7.8$ GeV, $\sigma_p^{SI} = 5.0 \times 10^{-36}$ cm^2, $f_n/f_p = -0.808$, and $\delta = 4.0$ keV with $\chi^2_{tot} = 94.7$, and for $n = 2$ the benchmark values are $M_{DM} = 6.6$ GeV, $\sigma_p^{SI} = 2.5 \times 10^{-35}$ cm^2, $f_n/f_p = -0.73$, and $\delta = -2.8$ keV with $\chi^2_{tot} = 90.1$.

Overall, our *a priori* expectations are verified. As indicated by the relative reduction in total chi-squared, greater overlap between the DAMA and CoGeNT ROIs is achieved by increasing the powers of q^2 in the MD scattering form factor. With respect to the XENON constraints, MD DM with $1/q^2$ dependence results in a weakening of the limits relative the purely inelastic IV case, whereas the bounds become noticably stronger for the $n > 0$ form factors (especially in the case of XENON10 which probes a lower range of recoil energy and hence is more susceptible

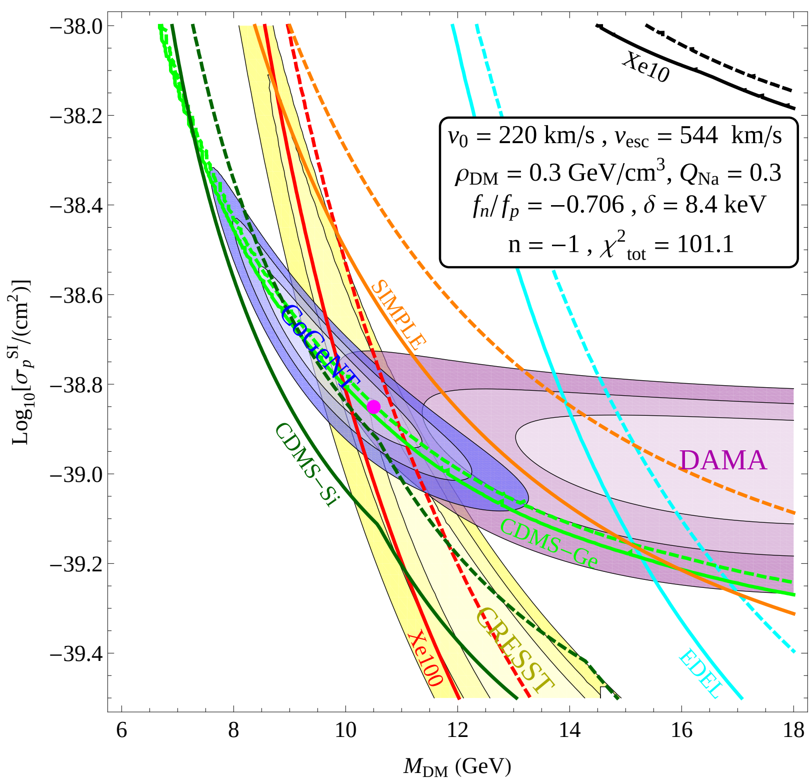

FIGURE 5.11: Momentum-dependent inelastic isospin-violating spin-independent DM fit to the experimental data in the σ_p^{SI}-M_{DM} plane with $n = -1$, $f_n/f_p = -0.706$ and $\delta = 8.4$ keV.

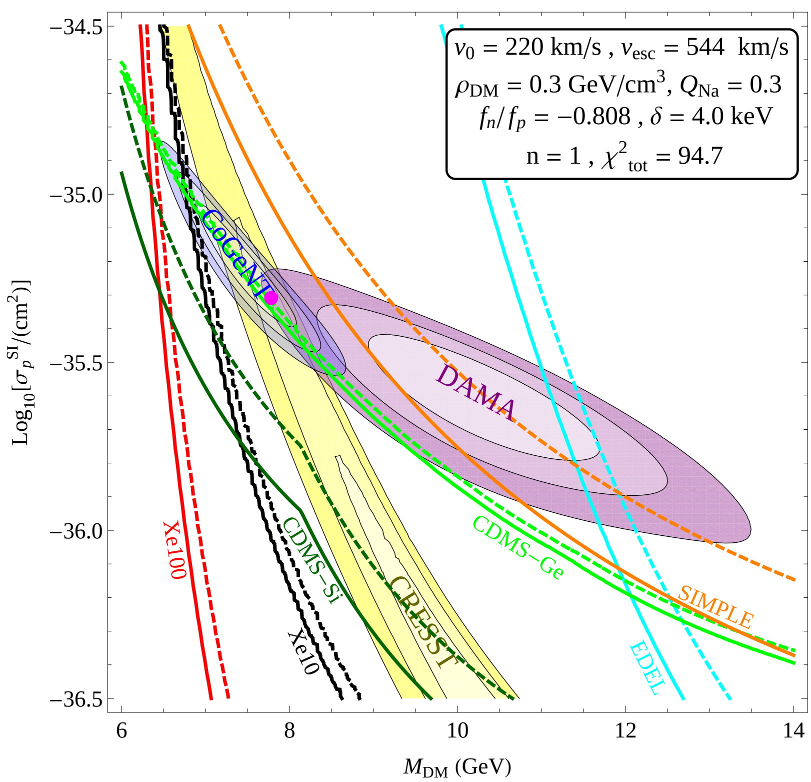

FIGURE 5.12: Momentum-dependent inelastic isospin-violating spin-independent DM fit to the experimental data in the σ_p^{SI}-M_{DM} plane with $n = 1$, $f_n/f_p = -0.808$ and $\delta = 4.0$ keV.

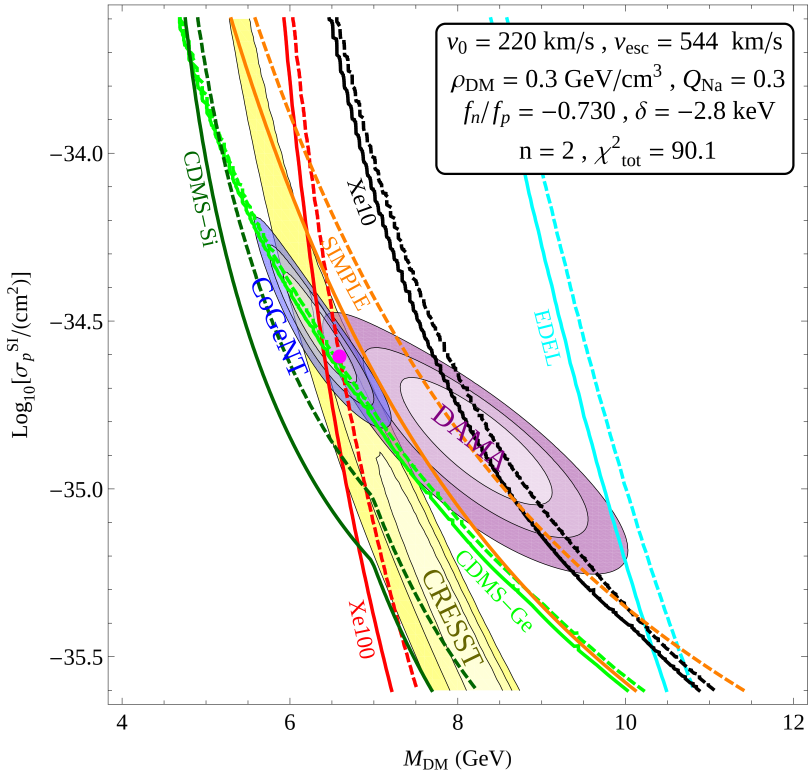

FIGURE 5.13: Momentum-dependent inelastic isospin-violating spin-independent DM fit to the experimental data in the σ_p^{SI}-M_{DM} plane with $n = 2$, $f_n/f_p = -0.730$ and $\delta = -2.8$ keV.

to the broadening of the event spectra). However, in the case of q^2 scattering, the isospin violation ratio required to minimize the total chi-squared deviates from the optimal value of -0.7 to the extent that the CoGeNT ROI is completely excluded by XENON100, and almost entirely by XENON10. As for q^4 scattering, the value of f_n/f_p at the benchmark point is such that a significant portion of the CoGeNT signal is able to evade the XENON100 95.4% CL. Unfortunately, in all the MD scattering scenarios considered here, it remains that the CDMS-Si exclusion curves forbade any fully mutual overlap between positive-signal ROIs.

5.4.3 Energy dependent DAMA quenching factors

A recent experimental determination of the quenching factor for nuclear recoils in NaI[Tl] is performed in reference [56]. The result confirms expectations that Q_{Na} depends on the nuclear recoil energy deposited by incident particles. Reference [56] reveals a propensity for the quenching factor to diminish with decreasing sodium recoil energy. This is in contrast to previous evaluations of the sodium quenching factor which all suggest a quenching factor which is constant with

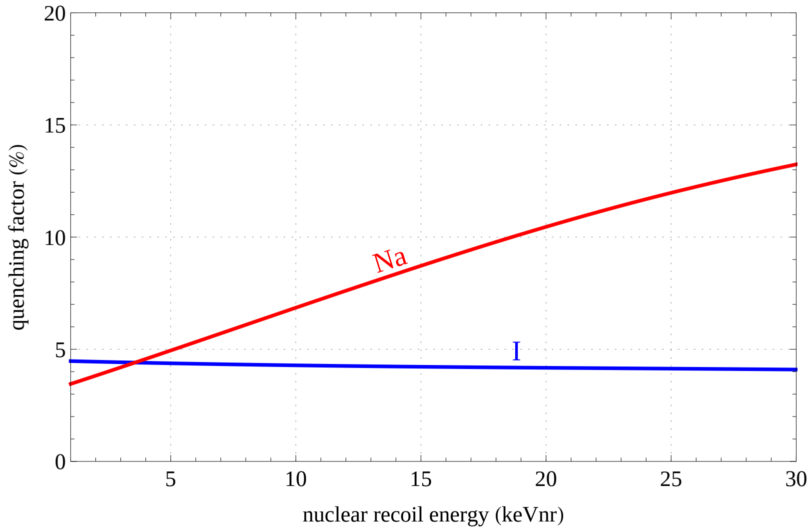

FIGURE 5.14: Forms of the sodium (Na) and iodine (I) energy dependent quenching factors of this thesis in percent, as interpolated using the original results in Figure 9 of reference [56].

nuclear recoil energy and $\gtrsim 0.15$. However, reference [56] argues that at past measurements, an inadequate light yield mixed with an insufficient control of systematics close to threshold could falsely produce constant or increasing quenching factors with decreasing recoil energy.

The implications of these results is most crucial for low-mass DM which deposits small amounts of nuclear recoil energy and hence, most affected by a diminishing quenching factor. By interpolating the values of the quenching factor found in Figure 9 of [56], it is possible to fit the DAMA data to energy-dependent quenching factors. For the iodine quenching factor, we take Q_I to be constant below the energy corresponding to the first data point, and logarithmically extrapolate the line connecting the final two data points to higher values of E_{nr}. The results of our interpolation of the sodium and iodine quenching factors as a function of nuclear recoil energy are plotted in Figure 5.14.

Figure 5.15 reveals the results of fitting DAMA using energy-dependent quenching factors. The result is a deterioration in the agreement between DAMA and the other positive-signal experiments for both standard and non-standard models. Even with the substantial amount of isospin-violation and mass splitting required to minimize the total chi-squared, the DAMA ROI strongly disagrees with all other experimental observations. As a result, with these new values of the NaI[Tl] quenching factors, the possibility of using IVDM to ameliorate the tensions posed by DAMA is ruled out. An analysis of inelastic IVDM with these energy dependent quenching factors arrives at the same conclusion.

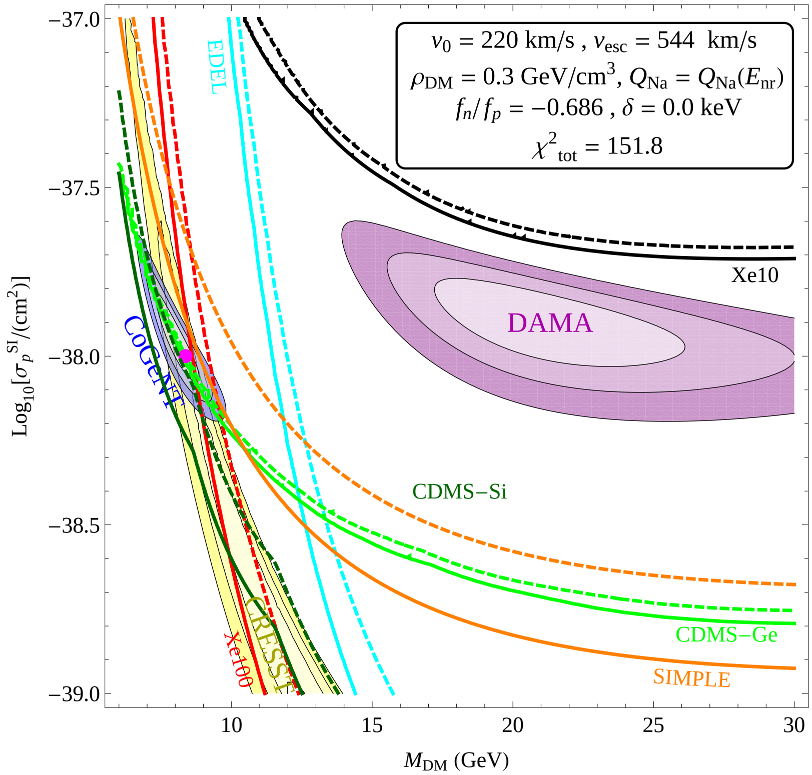

FIGURE 5.15: Elastic isospin-violating spin-independent DM fit to the experimental data in the σ_p^{SI}-M_{DM} plane with $f_n/f_p = -0.686$, $\delta = 0.0$ keV and using the energy dependent quenching factors of Figure 5.14 for DAMA target material.

5.4.4 Expectations for XENON1T

Currently, the XENON collaboration is finalizing technical designs for the next generation detector XENON1T, which plans to employ a dual-phase time projection chamber containing 3 tonnes of liquid xenon (corresponding to a fiducial mass of 1 tonne) in its search for WIMPs [131, 132]. Through combination of an increased fiducial volume, and reduction in the expected background by a factor of 100, XENON1T's sensitivity for 50 GeV WIMPs is estimated to fall to 2×10^{-47} cm^2 in the standard SI model. If XENON1T fails to detect any signal compatible with DM, the prospect of $\mathcal{O}(10)$ GeV WIMPs providing an explanation for positive-signal experiments will be deeply challenged.

However, using the method surronding equation (2.21), it is possible to forecast how strongly IVDM will be constrained by XENON1T data by rescaling the IC results of reference [132]. Figure 5.16 shows the evolution of the XENON upper limit including the 2011 and 2012 XENON100 results, as well as the 90% CL 2017 projection for XENON1T under an elastic SI IV DM model.

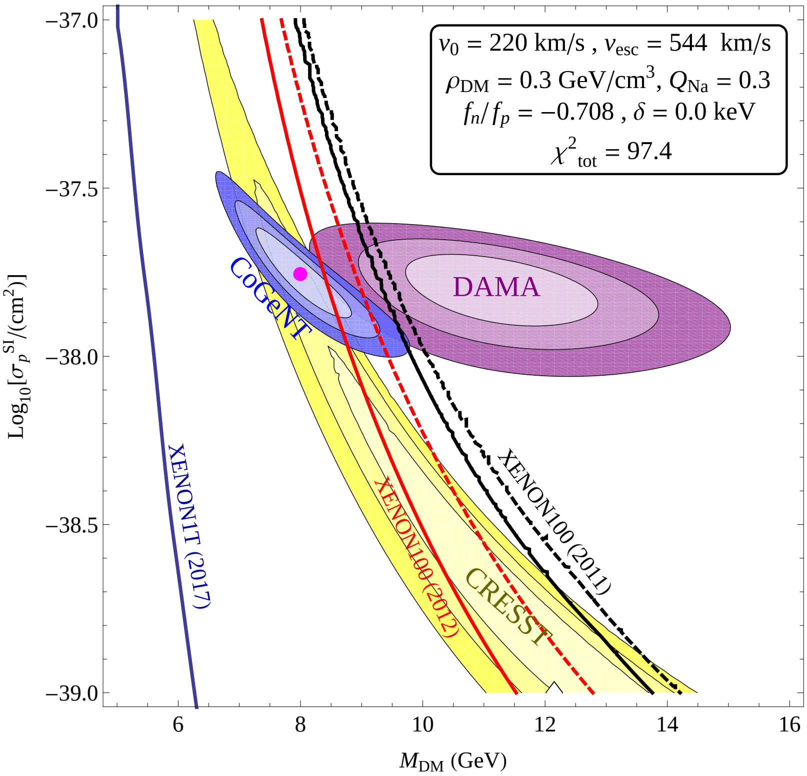

FIGURE 5.16: Expectations for XENON1T on elastic isospin-violating spin-independent DM. An IVDM fit to the positive-signal data is also plotted. The 2011 XENON100 constraint is shown in black, the 2012 XENON100 constraint is shown in red, and the projected 2017 XENON1T 90% CL is shown in blue.

As usual, f_n/f_p is chosen to minimize the total chi-squared. The results show that in the absence of a DM signal at XENON1T, an elastic IVDM framework fails to simultaneously explain the null and positive signal experiments. On the other hand, given that inelastic DM has the potential to weaken the XENON100 exlusion curve relative CoGeNT, it is conceivable that in light of XENON1T, inelastic IVDM might be able to provide a consistent explanation to the CoGeNT data only.

5.5 Spin-dependent isospin-violating DM

In parallel with our analysis of SI IV DM, the SD WIMP-nucleon coupling ratio a_n/a_p is treated as a free parameter which is allowed to float. As mentioned in Chapter 4, the only study to have considered a generalized elastic SD interpretation of DM was carried out in reference [107] whereby the compatibility of CoGeNT and DAMA signals in light of XENON100 and PICASSO constraints was tested within the $a_n - a_p$ phase space for fixed DM mass. In contrast to [107], we assess the viability of SD DM as a possible explanation for the experimental data through a series of σ_p^{SD}-M_{DM} space plots where a_n/a_p is fixed by minimizing the total chi-squared representing the unmodulated CoGeNT and DAMA data. Furthermore, for the first time, inelastic and MD couplings are introduced within the SD framework.

Unlike the SI case, it is not possible to relate the IV WIMP-proton cross section to the one which would be observed under the assumption of isospin conservation via a rescaling factor. The reason being that the SDSFs $S(q)$ depend too strongly on the SD WIMP-nucleon couplings ratio. On the other hand, by taking the limit of zero momentum transfer in the SD WIMP-nucleus cross sections for IV and IC DM, it can be shown that

$$\sigma_p^{IV} \sim \xi^{SD}(a_n/a_p)\sigma_p^{IC}, \tag{5.3}$$

where

$$\xi^{SD}(a_n/a_p) = \frac{\sum_{i,j} \kappa_j \beta_{ij} \mu_{A_{ij}} \frac{J_{ij}+1}{J_{ij}} \langle S_p \rangle_{ij}^2}{\sum_{i,j} \kappa_j \beta_{ij} \mu_{A_{ij}} \frac{J_{ij}+1}{J_{ij}} (\langle S_p \rangle_{ij} + a_n/a_p \langle S_n \rangle_{ij})^2}. \tag{5.4}$$

In the above equation, $\langle S_p \rangle_{ij}$ and $\langle S_n \rangle_{ij}$ are the proton and neutron spin matrix elements for nuclei A_{ij}, respectively. Similar to section 5.3, by using equation (5.4) it should be possible to gain qualitative insight into the effects that varying the SD IV ratio has on the ROIs and exclusion curves of Figure 5.2.

Figure 5.17 plots ξ^{SD} as a function of a_n/a_p for a WIMP mass of 10 GeV and for the various target material relevant to SD DM. Again, for the relevant WIMP masses, the DM-nucleon scattering will be dominated by the lighter nuclei in detectors that are composed of multiple element types. Relative the standard protonic SD scenario, a favourable value of a_n/a_p is one that amplifies the DAMA ROI with respect to the CoGeNT claim by about three orders of magnitude. Figure 5.17 demonstrates that this occurs for two values of the couplings ratio, once at $a_n/a_p \sim -2$, and again at $a_n/a_p \sim 3$. In fact, our analysis confirms the existence of two minima in the total chi-squared for DAMA and CoGeNT which are in excellent agreement with the predictions mentioned here, with the global minimum occuring at $a_n/a_p = 2.93$. Notwithstanding this result, the findings of Figure 5.17 extinguish the possibility of weakening both the XENON100 and SIMPLE constraints with respect to DAMA, since neither have ξ^{SD} functions which are

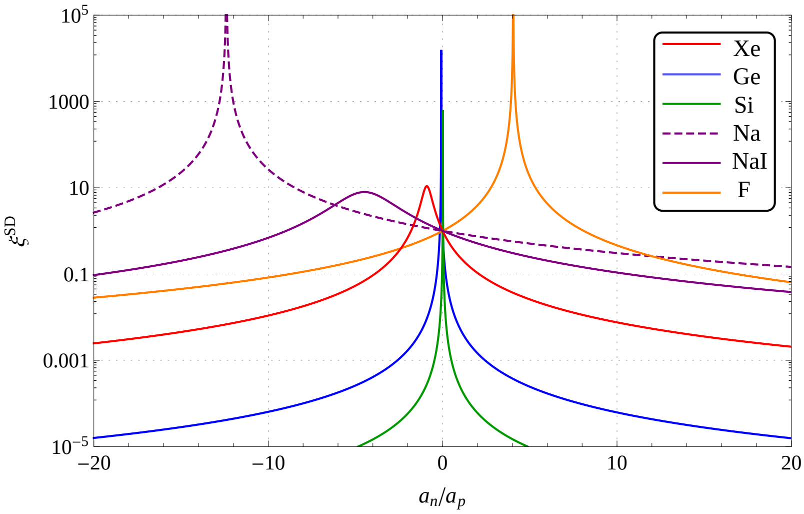

FIGURE 5.17: Graphing the spin-dependent function $\xi^{SD}(a_n/a_p)$ of equation (5.4) for various target material and for DM mass $M_{DM} = 10$ GeV.

simultaneously greater than that of sodium. Additionally, only for the larger benchmark value of a_n/a_p where agreement between CoGeNT and DAMA arise, does the SIMPLE ξ^{SD} function surpass sodium's. Hence, we focus on this region of parameter space.

Figure 5.18 shows the ROIs and exclusion curves for elastic SD DM under a general IV scenario. The benchmark point with $\chi^2_{tot} = 80.6$ corresponds to parameter values $M_{DM} = 8.9$ GeV, $\sigma_p^{SD} = 6.9 \times 10^{-37}$ cm^2, and $a_n/a_p = 2.93$. Fair overlap between the CoGeNT and DAMA claimed regions is obtained however, both are excluded by the 99.7% XENON100 and SIMPLE CL's. Moreover, the benchmark point is also ruled out by the XENON10 and CDMS-Ge bounds. Conversely, a substantial improvement in the goodness of fit over the purely protonic and neutronic SD models is observed with reductions in the total chi-squared value of $\Delta\chi^2_{tot} = 146.3$ and 57.9, respectively.

5.5.1 Inelastic and momentum-dependent couplings

The introduction of inelastic couplings to a SD model of DM scattering will incur the same effects as those observed for SI DM that is, a non-zero mass splitting parameter will alter the range of recoil energies probed by scattering DM particles. In a SD scenario, exothermic scattering will be the preferred mode of interaction for the following reasons: sodium is much lighter than germanium and hence a negative mass splitting parameter would cause greater shifts to lower

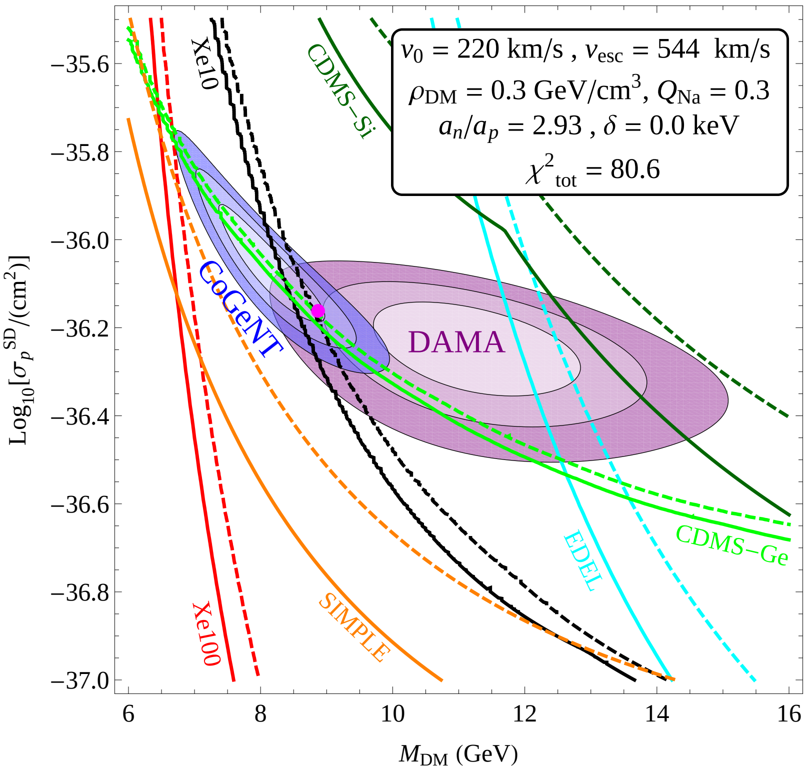

FIGURE 5.18: Elastic isospin-violating spin-dependent DM fit to the experimental data in the σ_p^{SD}-M_{DM} plane with $a_n/a_p = 2.93$ and $\delta = 0.0$ keV.

DM masses in DAMA than in CoGeNT, and since CRESST is absent from the analysis, the cost of increases in χ^2_{CRESST} that would arise in trying to optimize the fit between DAMA and CoGeNT is not present. Therefore, the relative shift in the DAMA ROI can be optimized with the correct choice of δ without an unwanted increase in χ^2_{tot} due to CRESST.

Figure 5.19 plots the experimental results for inelastic IV SD DM in the σ_p^{SD}-M_{DM} phase space for best-fit values $M_{DM} = 6.9$ GeV, $\sigma_p^{SD} = 4.9 \times 10^{-37}$ cm^2, $a_n/a_p = 1.84$, and $\delta = -14.7$ keV with corresponding total chi-squared $\chi^2_{tot} = 63.7$. As anticipated, the benchmark parameter values are in agreement with the previously stated predictions. Evidently, there exists overwhelming consistency in the overlap between the DAMA and CoGeNT ROIs, and given that the corresponding optimal chi-squared value is $\chi^2_{opt} = 54$, this substantiates the construction of an inelastic SD IV model of DM.[6] What's more is that compatibility is achieved using the fiducial value of for the sodium quenching factor, that is, $Q_{\text{Na}} = 0.3$. In fact, even when the lower limit value of $Q_{\text{Na}} = 0.2$ is assigned to the quenching factor, a_n/a_p and δ can be chosen such that strong overlap in the DAMA and CoGeNT signals is attainable — a feature not possible with

[6] An analysis of a SI inelastic IVDM model that considers only CoGeNT and DAMA data results in a total chi-squared value of $\chi^2_{tot} = 65.2$, revealing that the SD scenario is indeed the more favourable DM scheme.

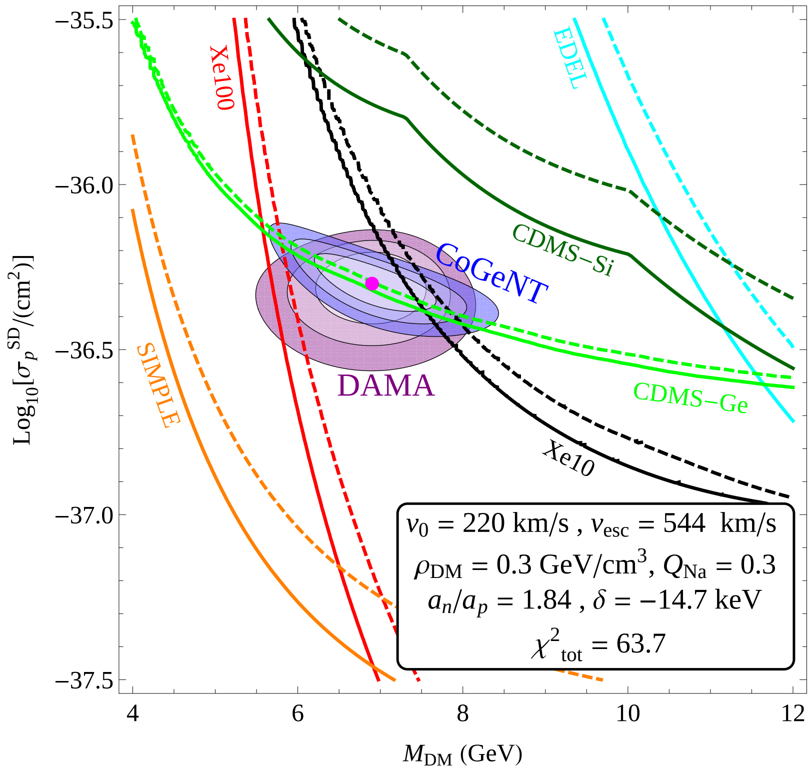

FIGURE 5.19: Inelastic isospin-violating spin-dependent DM fit to the experimental data in the σ_p^{SD}-M_{DM} plane with $a_n/a_p = 1.84$ and $\delta = -14.7$ keV.

SI DM, and desirable since the quenching factor is expected to take on such lower values.

Nonetheless, aspiration for a global fit to all the data is once again stifled by the persistent tensions posed by null constraints. In section 5.4.2, MD scattering with a form factor $\propto 1/q^2$ (n = -1 case) was shown to considerably weaken both the XENON100 and SIMPLE exlusion limits hence, one might conjecture its advantageous impact on the pertinent SD model. Figure 5.20 investigates the effects that a $n = -1$ MD coupling has on the σ_p^{SD}-M_{DM} phase space plot for inelastic IV SD DM. For parameter values $M_{DM} = 8.6$ GeV, $\sigma_p^{SD} = 2.4 \times 10^{-38}$ cm^2, $a_n/a_p = 1.76$, and $\delta = -10.36$ keV, a slightly larger chi-squared statistic of $\chi^2_{tot} = 67.0$ is obtained however, there is excellent agreement between the CoGeNT and DAMA ROIs, and the SIMPLE exclusion curve is, for the most part, entirely evaded at the 95.4% CL. Regardless, the XENON100 constraint remains strong and rules out all regions of mutual compatability.

With almost all of the phenomenological avenues contained herein exhausted in our attempt to reconcile direct detection data, it remains to combine the SI and SD components of the DM event rate.

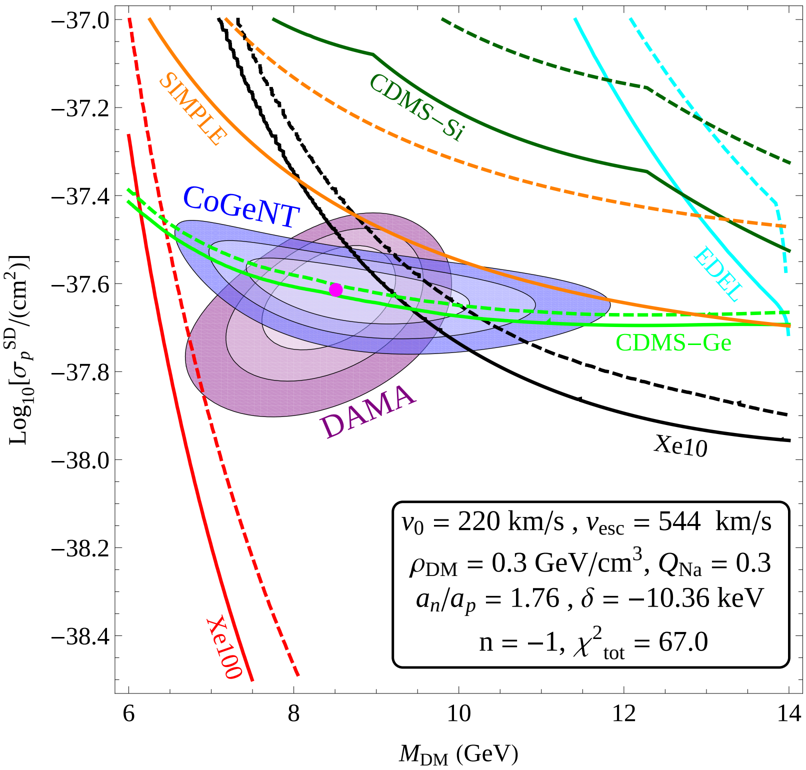

FIGURE 5.20: Momentum-dependent inelastic isospin-violating spin-independent DM fit to the experimental data in the σ_p^{SD}-M_{DM} plane with $n = -1$, $a_n/a_p = 1.76$ and $\delta = -10.36$ keV.

5.6 Combined isospin-violating DM

Recall from Chapter 2 that the DM event spectrum is comprised (independently) of a SI and a SD component. Typically, it is assumed that either the scalar or axial-vector current dominates the differential event rate; interactions contain purely SI or SD couplings. This assumption is not well justified since in the most general case there is no *a priori* reason to set one of the operators in the DM-nucleon interaction to zero. Although phenomenological models which aim to describe the microphysical DM interactions tend to focus on only the SI or SD component, it is conceivable that such a combined model of DM might be formulated. For example, in the case of slow-moving Majorana neutralinos, the two terms that remain in the interaction Lagrangian in the non-relativistic limit are the SI and SD components [100]. As a result, we employ a generalized scenario, referred to here as combined DM, which incorporates the following parameters as a final attempt to fit direct detection data: M_{DM}, σ_p^{SI}, f_n/f_p, σ_p^{SD}, a_n/a_p, and δ.

A clear advantage to mixed DM is that it allows for a fit to the CRESST-II data while taking into consideration possible SD effects arising in interactions with nuclei that contain spin. In

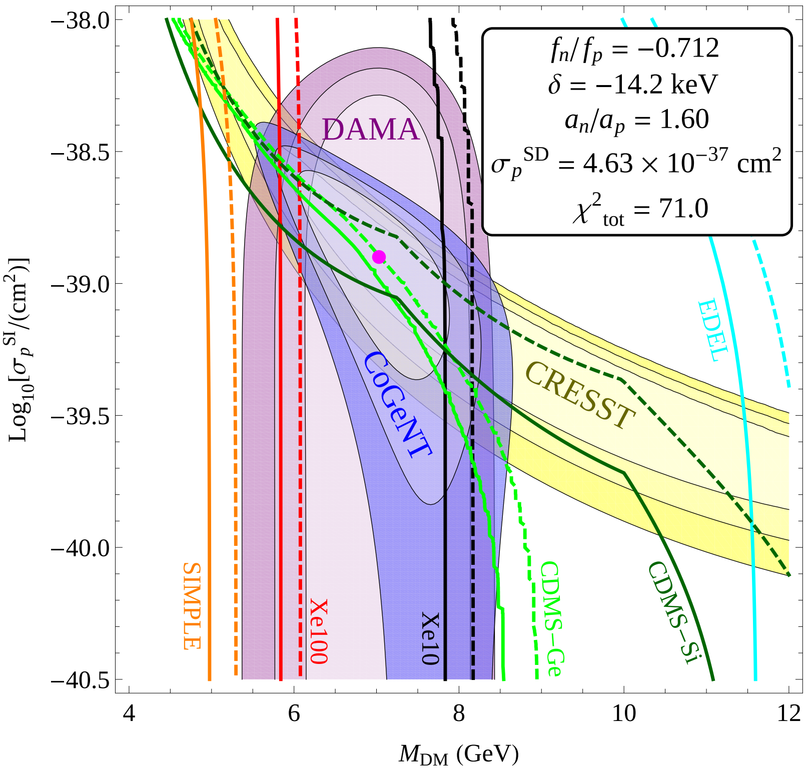

FIGURE 5.21: Inelastic isospin-violating combined DM fit to the experimental data in the σ_p^{SI}-M_{DM} plane with $f_n/f_p = -0.712$, $a_n/a_p = 1.60$, $\sigma_p^{SD} = 4.63 \times 10^{-37}$ cm^2 and $\delta = -14.2$ keV. Fiducial values of v_{esc}, v_0, ρ_{DM}, and Q_{Na} are used.

an effort to provide a comprehensive fit to all the data, we advance straightaway to the case of inelastic DM thereby utilizing all the available parameters of the general theory. First, consider the results of Figure 5.21 which plots the experimental findings of inelastic combined IVDM. The minimum value of the total chi-squared $\chi^2_{tot} = 71.0$, is achieved for the benchmark point $M_{DM} = 7.1$ GeV, $\sigma_p^{SI} = 1.2 \times 10^{-39}$ cm^2, $f_n/f_p = -0.712$, $a_n/a_p = 1.60$, $\sigma_p^{SD} = 4.6 \times 10^{-37}$ cm^2, and $\delta = -14.2$ keV. Given that the corresponding optimal chi-squared value is $\chi^2_{opt} = 58$, the results of this universal model illustrate that even when we employ a large number of parameters, it is a Sisyphean task to provide a consistent DM explanation to all the data. On an aside, it is verified that the addition of two extra parameters is justified under the Bayesian information criterion. For the three parameter elastic IV SI model $BIC = 109.8$, and for the inelastic IV combined model $BIC = 95.9$, indicating that the additional parameters are indeed justified.

Qualitatively speaking, the universal model of DM demonstrates that mutual overlap amongst the three positive-signal ROIs is possible. Furthermore, there exists a small triangular region of compatibility which bypasses all 99.7% exclusion curves except for that posed by SIMPLE. This is encouraging since no model of CoGeNT, CRESST, and DAMA considered

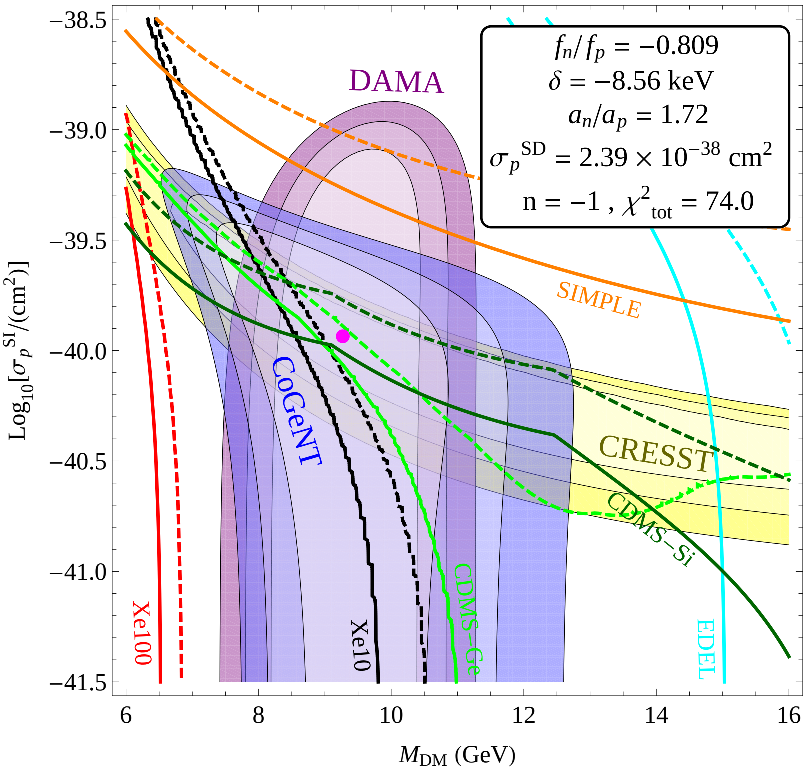

FIGURE 5.22: Inelastic isospin-violating combined DM fit to the experimental data in the σ_p^{SI}-M_{DM} plane with $n = -1$, $f_n/f_p = -0.809$, $a_n/a_p = 1.72$, $\sigma_p^{SD} = 2.39 \times 10^{-38}$ cm^2 and $\delta = -8.56$ keV. Fiducial values of v_{esc}, v_0, ρ_{DM}, and $Q_{\rm Na}$ are used.

thus far has been able to simultaneously evade the XENON100 and CDMS-Si bounds — bounds which are most constraining for IVDM. As for SIMPLE, it remains plausible that due to the vast number of unknowns associated with the SIMPLE modules, the officially purported limit might be over exaggerated. As a result, it is premature to entirely rule out the most general inelastic combined IVDM scenario.

In the same manner as the previous section, we introduce $n = -1$ MD scattering as a means to reduce the tensions between the positive-signal claimed regions, and SIMPLE and XENON100. Figure 5.22 discovers that the introduction of a $1/q^2$ form factor has the same effects as in the inelastic IV SD case that is, there is an extensive weakening of the SIMPLE constraint at the cost of a slight increase in the total chi-squared value, and a small enhancement in the region excluded by XENON100. The benchmark point for the $n = -1$ model is $M_{DM} = 9.3$ GeV, $\sigma_p^{SI} = 1.1 \times 10^{-40}$ cm^2, $f_n/f_p = -0.809$, $a_n/a_p = 1.72$, $\sigma_p^{SD} = 2.4 \times 10^{-38}$ cm^2, and $\delta = -8.56$ keV. Consequently, we conclude that there is little basis to favour MD couplings over the standard case for general combined DM.

Chapter 6

A Halo-Independent Analysis

Perhaps the greatest challenge facing the interpretation of direct detection data is developing an understanding of the uncertainties associated with the distribution and dynamics of DM within the Galactic halo. In section 5.2, we investigated how variations in the Galactic escape velocity and Sun's circular velocity affect the experimental data. The results of this analysis were highly dependent on the mass of the target nucleus, and the range of nuclear recoil energies probed by the respective experiments. Furthermore, although simulations have shown that the SHM provides a satisfactory approximation to the distribution of DM in our Galaxy, we pointed out a number of more sophisticated models which together, produce a range of theoretical predictions for light DM scattering.

As a result, the formulation of an analysis of DM detection which is independent of the astrophysical and halo uncertainties is well motivated. Although several different methods for a halo-indpendent analysis are available, we employ the one first developed by Fox, Lui, and Weiner as extended by Gondolo and Gelmini [111]. The approach involves converting the experimental results into v_{min}-space using the fact that each experiment, for a given model of DM, should in theory measure the same integral of the velocity distribution in the differential event rate. Since the velocity integral includes all the necessary information on the astrophysical parameters and distribution of DM in the Galaxy, by assuming that all the direct detection experiments are observing the same DM particle, the experimental event rates should combine to yield a consistent velocity integral as a function of v_{min}. The advantage of the Gondolo and

Gelmini method, is that it readily includes energy resolution and efficiency with arbitrary energy dependence, making it more adept in treating experimental results.

Additionally, we will show how the halo-independent analysis can be extended to include inelastically scattering DM. In contrast to reference [114] which tests inelastic DM in a halo-independent way via their "shape-test", we develop a method that allows a presentation of inelastic scattering models in the $\tilde{\eta}$-v_{min} phase space plots common to the literature. Also for the first time, we generalize the halo-independent method to account for the possibility of momentum- and spin-dependent scattering.

6.1 Theory: Converting to v_{min}-space

To convert the experimental results to v_{min}-space, we follow the method of reference [111], and then extend their analysis to include spin-dependent, inelastic and momentum-dependent scattering. Recall the differential event rate of equation (2.19) but with each term divided by the total mass of the corresponding element to obtain units of [counts/keV/kg/day]:

$$\frac{dR}{dE_{nr}} = \sum_{i,j} \kappa_j \beta_{ij} \left(\frac{q_{ij}(E_{nr})^2}{q_{ref}^2} \right)^n \frac{\rho_{DM}\sigma_p}{2M_{DM}\mu_{ne}^2} \left(Z_j + \frac{f_n}{f_p}(A_{ij} - Z_j) \right)^2 F_{SI_{ij}}^2(E_{nr}) \eta(v_{min}, t), \tag{6.1}$$

where we have inserted κ_j (the fraction of target material composed of element j), and have left all other definitions unchanged. One might consider the possibility of inferring the velocity distribution directly from the experimental data. Since any WIMP which has an incoming velocity larger than the minimum velocity required to produce a particular nuclear recoil energy has the potential to create an event with that energy, performing such an inference would be burdensome (see for instance references [133, 134]). As a result, the quantity that is more readily probed by the various experiments will be the integral of the velocity distribution. Since we can relate the nuclear recoil energy to the minimum velocity for scattering through equation (2.2), it should be possible to convert equation (6.1) to v_{min}-space and use experimental results for dR/dE_{nr} to determine values of η as a function of v_{min}. Furthermore, depending on the range of recoil energies accessed by a particular experiment, different experiments will probe different regimes of v_{min}-space and in principle, this should result in the inferred function of η.

To account for the dynamics of the Galactic DM halo, it is desirable to separate the velocity distribution into a time-independent and time-dependent component. The time dependence of the velocity distribution integral, due to the Earth's revolution around the Sun, can be approximated by the first term of a harmonic series as such:

$$\eta(v_{min}, t) = \eta_0(v_{min}) + \eta_1(v_{min}) \cos\left[\frac{2\pi(t - t_0)}{1\text{yr}}\right]. \tag{6.2}$$

As a result, we can gain knowledge on the static and temporal amplitudes $\tilde{\eta}_0$ and $\tilde{\eta}_1$ using unmodulated and modulated experimental data. Furthermore, notice how the combination $\tilde{\eta}(v_{min}, t) \equiv (\sigma_p^{SI}\rho_{DM}/M_{DM})\eta(v_{min}, t)$ is common to all experiments. Hence, it is possible to remove any assumptions regarding the DM-proton cross section and local DM density from the halo-independent analysis.

We mentioned in Chapter 2 that experimental results are usually quoted in terms of the electron recoil equivalent energy (keVee) as opposed to the true recoil energy (keVnr). The detected energies E', are subject to measurement uncertainties and fluctuations which are encapsulated in the energy response function $A(E_{nr}, E')$. In addition, detectors had specific efficiency or acceptance cuts which were contained in the function $\epsilon(E')$.

Introducing the energy response function and efficiency to equation (6.1), one obtains the experimental differential event rate:

$$\begin{aligned} \frac{dR}{dE'} &= \epsilon(E') \int_0^\infty \mathrm{d}E_{nr} \sum_{i,j} \kappa_j \beta_{ij} \left(\frac{q_{ij}(E_{nr})^2}{q_{ref}^2}\right)^n \frac{\rho_{DM}\sigma_p}{2M_{DM}\mu_p^2} \left(Z_j + \frac{f_n}{f_p}(A_{ij} - Z_j)\right)^2 F_{SI_{ij}}^2(E_{nr}) \\ &\quad \times A(E_{nr}, E')\eta(v_{min}, t), \end{aligned} \tag{6.3}$$

In order to convert to v_{min}-space, we must differentiate equation (2.2) and solve for $\mathrm{d}E_{nr}$ in terms of v_{min}. It is easy to show that for an isotope with atomic mass number A_{ij},

$$\mathrm{d}E_{nr} = \frac{4M_{A_{ij}}v_{min}}{(M_{A_{ij}}/\mu_{A_{ij}})^2 - (\delta/E_{nr})^2}\mathrm{d}v_{min}, \tag{6.4}$$

where E_{nr} is given by

$$E_{nr}^{\pm} = \frac{\mu_{A_{ij}}}{M_{DM}}\left(\mu_{A_{ij}} v_{min}^2 - \delta \pm v_{min}\sqrt{\mu_{A_{ij}}(\mu_{A_{ij}} v_{min}^2 - 2\delta)}\right). \tag{6.5}$$

For an elastic scenario, $\delta = 0$ and there is a one-to-one correspondence between v_{min} and E_{nr}. Thus for every range of energies there is a unique range of velocities, and vice versa. If $\delta \neq 0$, then there is an ambiguity in that there may be two possible solutions to E_{nr}. This complication is addressed in section 6.1.1.

Combining these results, the average expected event rate in the energy range $[E_1', E_2']$ can be written as:

$$\bar{R}_{[E_1',E_2']}(v_{min}, t) = \int_0^\infty \mathrm{d}v_{min} \Gamma^{SI}_{[E_1',E_2']}(v_{min}) \tilde{\eta}(v_{min}, t), \tag{6.6}$$

where $\Gamma^{SI}_{[E_1',E_2']}(v_{min})$ is a response function which takes the form

$$\begin{aligned} \Gamma^{SI}_{[E_1',E_2']}(v_{min}) &= \sum_{i,j} \kappa_j \beta_{ij} \left(\frac{q_{ij}(E_{nr})^2}{q_{ref}^2}\right)^n \frac{2M_{A_{ij}} v_{min}}{\mu_p^2 (E_2' - E_1')[(M_{A_{ij}}/\mu_{A_{ij}})^2 - (\delta/E_{nr})^2]} \\ &\quad \times \left(Z_j + \frac{f_n}{f_p}(A_{ij} - Z_j)\right)^2 F^2_{SI_{ij}}(E_{nr}) \int_{E_1'}^{E_2'} \mathrm{d}E' \epsilon(E') A(E_{nr}, E'). \end{aligned} \tag{6.7}$$

As discussed in reference [111], by mapping the energy interval $[E_1', E_2']$ into the range of velocities $[v_{min,1}, v_{min,2}]$, it is possible to calculate the v_{min}-weighted average of the velocity integral:

$$\overline{\tilde{\eta}_{[E_1',E_2']}} = \frac{\int_{v_{min,1}}^{v_{min,2}} \mathrm{d}v_{min} \Gamma^{SI}_{[E_1',E_2']}(v_{min}) \tilde{\eta}(v_{min}, t)}{\int_{v_{min,1}}^{v_{min,2}} \mathrm{d}v_{min} \Gamma^{SI}_{[E_1',E_2']}(v_{min})}, \tag{6.8}$$

which we rewrite as

$$\overline{\tilde{\eta}_{[E_1',E_2']}} = \frac{\hat{R}_{[E_1',E_2']}}{\mathcal{B}^{SI}_{[E_1',E_2']}}, \tag{6.9}$$

where $\mathcal{B}^{SI}_{[E_1',E_2']}$ is defined as the denominator of equation (6.8).

Note that the average event rate in the energy interval $[E_1', E_2']$ can be represented by a static and temporal component: $\hat{R}_{[E_1',E_2']} = \hat{R}_0 + \hat{R}_1 \cos\left[\frac{2\pi(t-t_0)}{1\mathrm{yr}}\right]$. Therefore, it is possible to make predictions on the functions $\overline{\tilde{\eta}_0}(v_{min})$ and $\overline{\tilde{\eta}_1}(v_{min})$ along with their associated uncertainties using experimental unmodulated and modulated measurements of $\hat{R}_0 \pm \Delta R_0$ and $\hat{R}_1 \pm \Delta R_1$, respectively. Furthermore, by evaluating $\overline{\tilde{\eta}_{0,1}}$ in all the energy bins of a given experiment, one may determine $\overline{\tilde{\eta}_0}$ and $\overline{\tilde{\eta}_1}$ as functions of v_{min}. In fact, for a particular experiment, the energy intervals are those given by the binning of the respective data along with any corresponding energy resolution $\sigma(E')$ evaluated at the endpoints of the bin. Therefore, for an energy range $[E'_1 - \sigma(E'_1), E'_2 + \sigma(E'_2)]$, the corresponding v_{min} interval is given by $[v_{min,1}, v_{min,2}] = [v_{min}(E_{nr}(E'_1 - \sigma(E'_1))), v_{min}(E_{nr}(E'_2 + \sigma(E'_2)))]$. This interval is taken as the uncertainty in v_{min} for the corresponding value of $\overline{\tilde{\eta}_{0,1}}$.

Carrying out a similar anaylsis using the spin-dependent WIMP-nucleus cross section, one can derive the η functions under a spin-dependent interpretation of the experimental data. The analogous SD response function of the halo-independent analysis is found to be

$$\begin{aligned}\Gamma^{SI}_{[E'_1,E'_2]}(v_{min}) &= \sum_{i,j} \kappa_j \beta_{ij} \left(\frac{q_{ij}(E_{nr})^2}{q^2_{ref}}\right)^n \frac{8\pi M_{A_{ij}} v_{min}}{3\mu_p^2(2J+1)(E'_2 - E'_1)[(M_{A_{ij}}/\mu_{A_{ij}})^2 - (\delta/E_{nr})^2]} \\ &\times \left(Z_j + \frac{f_n}{f_p}(A_{ij} - Z_j)\right)^2 \tilde{S}_{SD_{ij}}(E_{nr}) \int_{E'_1}^{E'_2} \mathrm{d}E' \epsilon(E') A(E_{nr}, E'), \end{aligned} \tag{6.10}$$

where $\tilde{S}_{SD_{ij}}(E_{nr}) = S_{00} + S_{01} + S_{11} + 2(a_n/a_p)(S_{00} - S_{11}) + (a_n/a_p)^2(S_{00} - S_{01} + S_{11})$ with the SDSFs corrseponding to isotope i of element j, and E_{nr} given by equation (6.5).

6.1.1 Inelastic halo-independent analysis

We now address complications associated with converting a range of nuclear recoil energies to a unique range of minimum velocities in the case of inelastic scattering. Our discussion follows a similar vein to that of reference [114]. Since a given value of v_{min} can correspond to up to two values of E_{nr}, it is conceivable that for some energy range $[E_1, E_2]$, the minimum value of v_{min} is found for an energy other than E_1. Furthermore, it is possible that $v_{min}(E_2)$ is not the true maximum value of v_{min} in the energy range considered. Thus the integral bounds appearing in equation (6.8) are not (necessarily) the range $[v_{min}(E_1), v_{min}(E_2)]$, but the range $[u_{min}, u_{max}]$ where u_{min} and u_{max} are the minimum and maximum values of v_{min}, respectively, in the energy range of interest. As a result, depending on whether u_{max} lies to the right or left in recoil energy of u_{min}, one must choose the solution E^+_{nr} or E^-_{nr}, respectively, in equation (6.5).

As an example, consider Figure 6.1 which plots v_{min} as a function of E_{nr} for some arbitrary nucleus mass, WIMP mass, and mass splitting $\delta > 0$. The minimum value of v_{min}

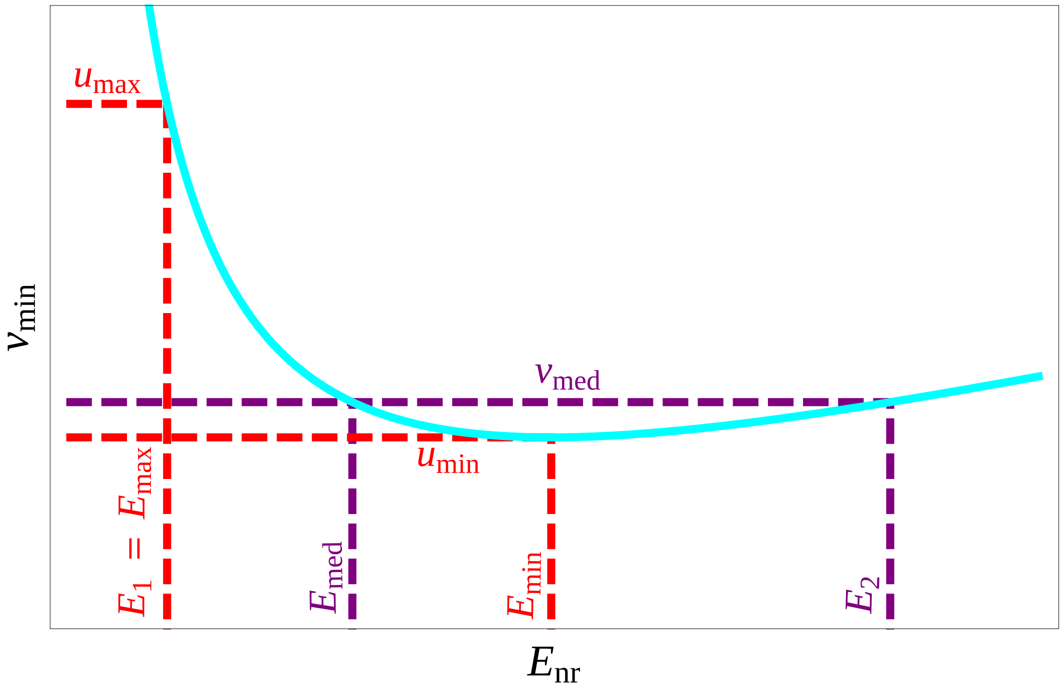

FIGURE 6.1: Plotting v_{min} as a function of E_{nr} for arbitrary nucleus mass, WIMP mass, and mass splitting $\delta > 0$. For a nuclear recoil energy range $[E_1, E_2]$, the corresponding range of minimum velocities $[u_{min}, u_{max}]$ is shown. The velocity v_{med} demonstrates how one value of v_{min} can arise from two values of E_{nr}.

is $u_{min} = \sqrt{2\delta/\mu_{A_{ij}}}$ at a recoil energy of $E_{min} = \mu_{A_{ij}}\delta/M_{A_{ij}}$. Suppose we are interested in converting the energy range $[E_1, E_2]$ into v_{min}-space. In this case, $E_1 < E_{min} < E_2$ and $v_{min}(E_1) > v_{min}(E_2)$. Accordingly, the range of velocities that the energy range $[E_1, E_2]$ probes is not $v_{min}(E_1)$ to $v_{min}(E_2)$, but the range u_{min} to u_{max} and it is the latter range which we integrate over for the energy interval $[E_1, E_2]$ in equation (6.8). Moreover, we realise that since we are integrating over velocities which correspond to energies less than E_{min}, we choose the E^-_{nr} solution in equation (6.5). Thus it is the energies corresponding to the range u_{min} - u_{max} which determine the particular solution of equation (6.5).

As another example, suppose $v_{min}(E_1)$ and $v_{min}(E_2)$ are both greater than E_{min}. In that case $u_{min} = v_{min}(E_1)$, $u_{max} = v_{min}(E_2)$, and we choose the E^+_{nr} solution in equation (6.5). Of course, other possibilities exist depending on the mass splitting and energy range under consideration however, we leave it to the reader to work out all scenarios.

As a final point, consider splitting the integral of our first example into the intervals $[u_{min}, u_{med}]$ and $[u_{med}, u_{max}]$. Then, there are two energy intervals that correspond to the velocity range

$[u_{min}, u_{med}]$, that is: $[E_{min}, E_{med}]$ and $[E_{min}, E_2]$. Reference [114] argues that both energy intervals will yield the same value of the velocity integral provided that the inelastic model being analysed is in fact correct. [114] tests inelastic DM as an interpretation of the data by determining whether or not the two energy intervals produce the same value of the velocity integral within experimental errors. This is what is meant by "shape-test". In our halo-independent study of inelastic scattering, an optimistic approach is taken in that we assume the inelastic DM hypothesis to be correct and consequently, that both energy intervals produce the same velocity integral result.

6.1.2 Determining upper limits in $\tilde{\eta}$-v_{min} space

For null experiments, we would like to be able to compute upper limts in v_{min}-space. A method for doing so was first presented by Fox, Lui, and Weiner in reference [109]. Since $\tilde{\eta}(v_{min})$ is a monotonicaly decreasing function, the following inequality holds for all v_{min}:

$$\tilde{\eta}(v_{min}) \geq \tilde{\eta}^*(v^*)\Theta(v^* - v_{min}), \tag{6.11}$$

where v^* is a fixed velocity and $\Theta(v)$ is the Heaviside function. Consequently, the $\tilde{\eta}$-function that predicts the smallest event rate with $\tilde{\eta} = \tilde{\eta}^*$ and $v_{min} = v^*$ is that given by $\tilde{\eta}(v_{min}) = \tilde{\eta}^*\Theta(v^* - v_{min})$. For this reason, the average event rate that is predicted in an energy interval $[E_1', E_2']$ using the above form of the velocity integral will be the most conservative, and is given by

$$\bar{R}_{[E_1',E_2']}(v_{min}, t) = \eta^* \int_0^{v^*} \mathrm{d}v_{min} \Gamma^{SI}_{[E_1',E_2']}(v_{min}) \tag{6.12}$$

By using the respective technique of a given experiment to compute upper limits, one simply increases η^* in equation (6.12) at each and every value of v^* until the event rate corresponding to a particular confidence level is reached. For example, in the prescription of the maximum gap method, the number of events are computed in the energy intervals corresponding to each gap, and $\tilde{\eta}^*$ is increased until the desired value of $C_0(x, \mu)$ is obtained.

Let us make another remark regarding the conversion of a range of energies into a unique range of minimum velocities. If a target material is composed of different element types or contains different isotopes, then there will not be a unique range of minimum velocities corresponding to some energy interval since the different elements and isotopes will have different masses. To deal with the possibility of multiple isotopes, we compute $\tilde{\eta}$ by adding up the $\tilde{\eta}_i$ for each isotope weighted by their respective fractional abundance. For detectors with different elements, variations in the element-dependent quatities are too large to perform a simple fractional abundance weighted sum. In the following section, we give references to the methods that are used here in order to deal with multi-element experiments.

6.2 Methodology

In this section, we briefly outline the methodologies for computing the $\tilde{\eta}(v_{min})$ values and/or upper limits for the experiments being examined in our halo-independent analysis.

CoGeNT To analyse the CoGeNT data, we calculate and employ event rates and uncertainties corresponding to the first 8 energy bins between 0.5 - 3.0 keVee using a 0.1 keVee binning, taking into account the quenching factor, efficiency cut, surface event acceptance, and background due to cosmogenic L-shell electron capture as outlined in section 3.1. Unlike reference [112] which considers a DM + background hypothesis, we follow Chapter 3 in subtracting a constant background from the data, which in this case is 2.35 cpd/kg/keVee. As in Chapter 3, we do not consider an energy resolution.

DAMA: For DAMA, we consider the same 8 energy bins and values of the modulated rate plus uncertanties as in Table 3.1. Since low mass WIMP-nuclei scattering is dominated by the Na nuclei, we follow references [110–112] and ignore the iodine scattering component for our halo-independent analysis of DAMA. We employ the same resolution as in section 3.2.

CRESST-II: In order to deal with the multiple detector elements at CRESST, we ignore scattering off W, and use method 2 of Appendix A in reference [110] in order to deal with scattering off both O and Ca. In their method, the energy bins and therefore the event rate that are used depend on the DM mass being considered. The energy intervals, event rates, and upper and lower limits on the event rate for the WIMP masses considered here are given in Table 3 of reference [110]. Our halo-independent analysis uses the same efficiencies and resolution as in section 3.3, and takes into account each module's energy threshold.

XENON10/100: For both XENON10 and XENON100 we implement the same events, backgrounds, efficiencies, and acceptance functions as outlined in Chapter 3. However, for simplicity, we use the maximum gap method instead of the p_{max}-method to compute XENON10 bounds.

CDMS-II Again, the same events, expected background, and efficiencies of Chapter 3 are used in our analysis of CDMS-Ge and CDMS-Si. However, for the halo-independent analysis we follow reference [112] in introducing an energy resolution to both CDMS experiments: $\sigma(E)/\text{keV} = \sqrt{0.293^2 + 0.056^2 E/\text{keV}}$. Since the CDMS-Si experiment has not measured the energy resolution in its detectors, we assume it to be the same as that used by CDMS-Ge.

For the analysis of the unmodulated CDMS-Si excess, the recoil spectrum is binned using a 2 keVnr bin width. The resulting bins contain either 0 or 1 event. Assuming zero background, the Poisson central confidence interval of $(0.173, 3.30)$ expected events may be used to determine the 1σ error bars in the bins containing 1 event.

SIMPLE: For SIMPLE, we employ the method of Frandsen *et* al. [110] in order to deal with the multiple detector elements in the context of an upper limit. The maximum gap method is performed using the same efficiency as in section 3.8, and we take into account the one observed event and expected backround of 2.2 $\pm$ 0.3.

EDELWEISS-II: We do not consider a halo-independent analysis of EDELWEISS-II since it was consistently found to give weak upper bounds in the phase space plots of Chapter 5.

6.3 Defining consistency in v_{min}-space

Before displaying any results, let us address the following question: what are the characteristics of a consistent fit in $\tilde{\eta}$-v_{min} space for a halo-independent analysis? There are a number of criteria that the results of a model must satisfy in order for a fit in v_{min}-space to be deemed sensible. Firstly, since our plots contain results from DAMA, which probes values of $\tilde{\eta}_1$, and CoGeNT, CDMS-Si and CRESST-II, which probe values of $\tilde{\eta}_0$, then the region favoured by DAMA should be considerably lower in $\tilde{\eta}$-space than that favoured by experiments which pertain to unmodulated event rates. This relies on the fact that any reasonable model of the Galactic halo should have η_1 sufficiently smaller than η_0, seeing as it appears at a higher order in the expansion of η.

Secondly, predictions for both $\tilde{\eta}_0$ and $\tilde{\eta}_1$ should be monotonically decreasing with larger values of v_{min} since any realistic halo model has a positive-definite velocity distribution, $f(v) \geq 0$, which means increasing the lower integral bound will decrease the resulting integral for a fixed upper limit. Furthermore, we expect the form of this decreasing η-function to be comparable to that of known Galactic halo models. Qualitatively speaking in a logarithmic plot, it is a non-linear function of v_{min}. Figure 4 of reference [110] shows η-functions corresponding to some well-known models of the Galactic halo.

Also, experiments which probe the same region of v_{min} should yield $\tilde{\eta}_0$ values which are consistent with one another within experimental uncertainty. Finally, the exclusion curves provided by null experiments should be compatible with the $\tilde{\eta}$ values favoured by positive-signal experiments.

6.4 Spin-independent results

For both the SI and SD halo-independent analyses, the values of M_{DM}, f_n/f_p, a_n/a_p, and δ are chosen such that they correspond to the benchmark point in the $\sigma_p^{SI,SD}$-M_{DM} plots of the standard analysis for the particular model under consideration (excluding contributions to χ^2_{tot} from the CDMS-Si signal). In that sense, it is apparent how the standard analysis in terms of the DM mass and DM-nucleon cross section are complementary to the halo-independent analysis. This is in contrast to all previous studies of halo-independent DM which choose parameter values based on qualitative inferences from the standard formalism literature. Unless stated otherwise, the sodium quenching factor in our analysis of DAMA data is taken to be $Q_{\mathrm{Na}} = 0.3$.

Figure 6.2 presents the results in $\tilde{\eta}$-v_{min} space for the standard SI model of WIMP scattering where $M_{DM} = 8.7$ GeV, $f_n/f_p = 1.0$, and $\delta = 0$ keV. The unmodulated measurements of $\tilde{\eta}_0$ are shown for CoGeNT, CDMS-Si, and CRESST-II, along with measurements by DAMA on the modulated component $\tilde{\eta}_1$ against the most constraining bounds arising from null experiments. The standard SI model fails to meet almost all criteria outlined in the previous section. The unmodulated CoGeNT measurements are for practical purposes, entirely excluded by the CDMS-Ge 95.4 % C.L. In addition, the XENON100 exclusion curve greatly constrains the regions of v_{min}-space favoured by DAMA, CDMS-Si, and CRESST-II, leaving only the lowest energy events of each experiment not entirely ruled out. Although the DAMA $\tilde{\eta}_1$ signal is smaller than the

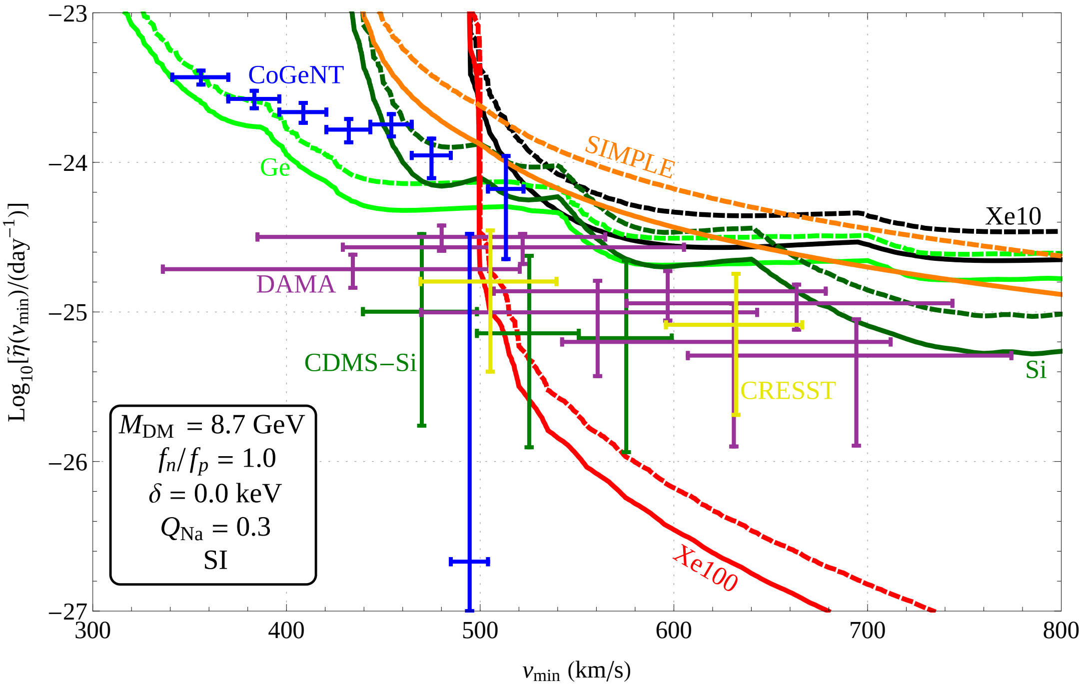

FIGURE 6.2: Elastic isospin-conserving spin-independent halo-independent DM fit to the experimental data in $\tilde{\eta}$-v_{min} space with $M_{DM} = 8.7$ GeV, $f_n/f_p = 1.0$, and $\delta = 0.0$ keV.

$\tilde{\eta}_0$ signal at CoGeNT, it is in gross conflict with the unmodulated measurements claimed by CDMS-Si and CRESST-II. On the other hand, the CDMS-Si and CRESST-II data suggest some degree of compatibility.

Introducing IV couplings, Figure 6.3 investigates the effects in v_{min}-space of setting $f_n/f_p = -0.708$. As anticipated, there is a substantial weakening of the XENON100 exclusion bound along with a strengthening in the CDMS-Si constraint. No relief in the tension between CoGeNT and CDMS-Ge is observed given that they are both composed of the same target material. In contrast, it is seen that the CDMS-Si and CRESST-II unmodulated measurements are mutually compatible and consistent with all null constraints. However, these measurements are in conflict with the region favoured by CoGeNT, and claim regions of $\tilde{\eta}$ space which are for the most part smaller than that observed by DAMA. Interestingly enough, the DAMA modulated data points are all consistent within their respective uncertainty with each null experiment upper limit.

Figure 6.4 considers a DM interpretation of elastic IV SI DM for the energy dependent sodium and iodine quenching factors of Figure 5.14. In this scenario, $M_{DM} = 8.36$ GeV, $f_n/f_p = -0.686$ and $\delta = 0$ keV. The qualitative results of all experiments other than DAMA remain unchanged.

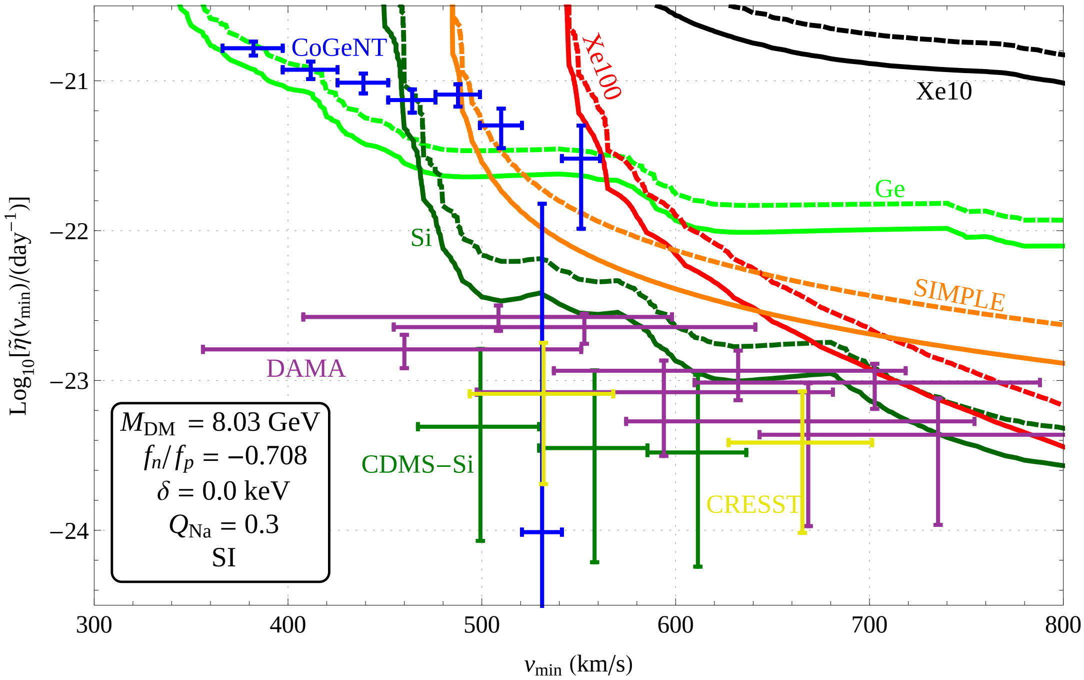

FIGURE 6.3: Elastic isospin-violating spin-independent halo-independent DM fit to the experimental data in $\tilde{\eta}$-v_{min} space with $M_{DM} = 8.03$ GeV, $f_n/f_p = -0.708$, and $\delta = 0.0$ keV.

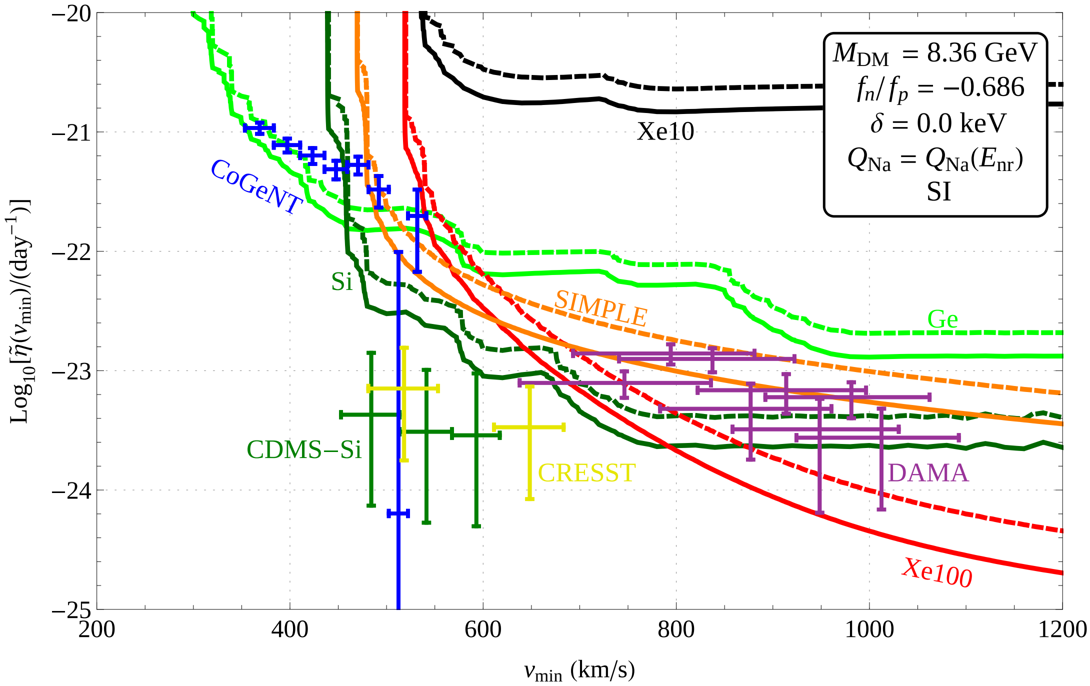

FIGURE 6.4: Elastic isospin-conserving spin-independent halo-independent DM fit to the experimental data in $\tilde{\eta}$-v_{min} space for energy dependent DAMA quenching factors with $M_{DM} = 8.36$ GeV, $f_n/f_p = -0.686$, and $\delta = 0.0$ keV.

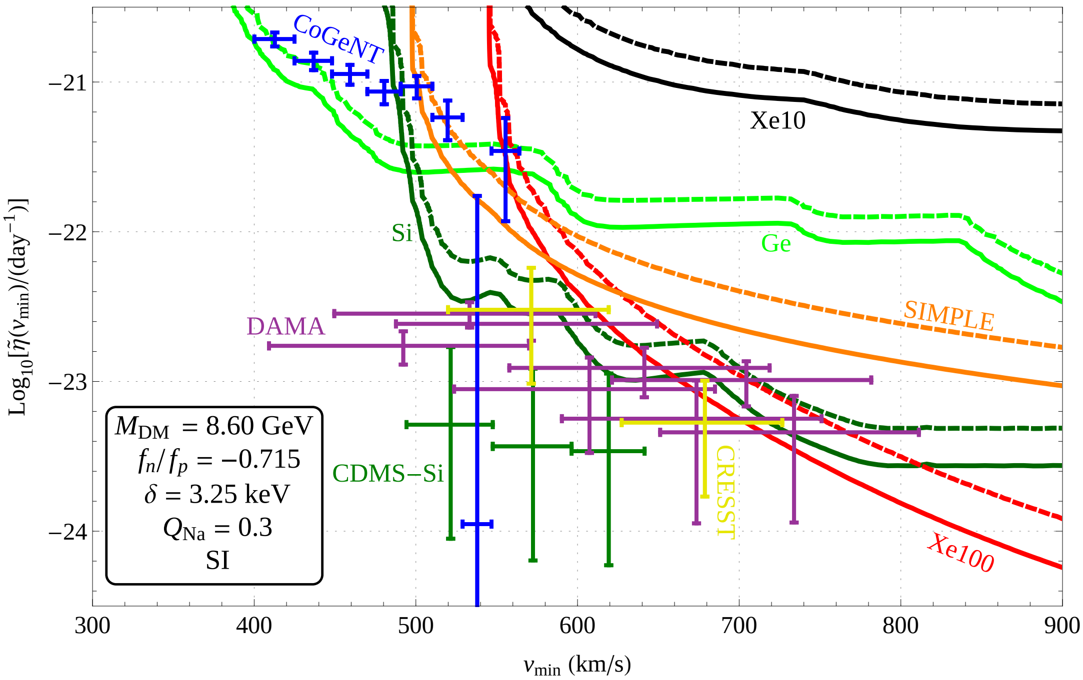

FIGURE 6.5: Inelastic isospin-violating spin-independent halo-independent DM fit to the experimental data in $\tilde{\eta}$-v_{min} space with $M_{DM} = 8.60$ GeV, $f_n/f_p = -0.715$, and $\delta = 3.25$ keV.

With energy dependent quenching factors, the DAMA measurements of the modulated $\tilde{\eta}_1$ function are all excluded by a combination of the XENON100 and to a lesser extent the CDMS-Si exclusion curves. This is expected since the energy dependent quenching factors produce larger values of the nuclear recoil energy E_{nr} which in turn, result in DAMA probing larger regions of v_{min}-space. Under this scenario, DAMA is irreconcilable with null constraints.

In Chapter 5, the addition of a mass splitting parameter to the SI IV DM model results in a benchmark point for the relevant halo-independent parameters of $M_{DM} = 8.60$ GeV, $f_n/f_p = -0.715$, and $\delta = 3.25$ keV. However the reduction in the total chi-squared value is not enough to make favourable the inclusion of an inelastic coupling. Figure 6.5 considers this scenario in $\tilde{\eta}$-v_{min} phase space nevertheless. For positive-signal experiments, there is a small shift to larger values of v_{min} for the data points corresponding to lower recoil energies. The incompatibility between CoGeNT and other unmodulated measurements of $\tilde{\eta}_0$ remains unresolved, not to mention the deterioration in the agreement between the CDMS-Si and CRESST values of $\tilde{\eta}_0$ relative the elastic case. Also, DAMA remains in conflict with the CDMS-Si and CRESST-II unmodulated measurements and overall, the XENON100 upper limit becomes more constraining in the inelastic scenario. Nevertheless, one could conceivably argue that the combination of

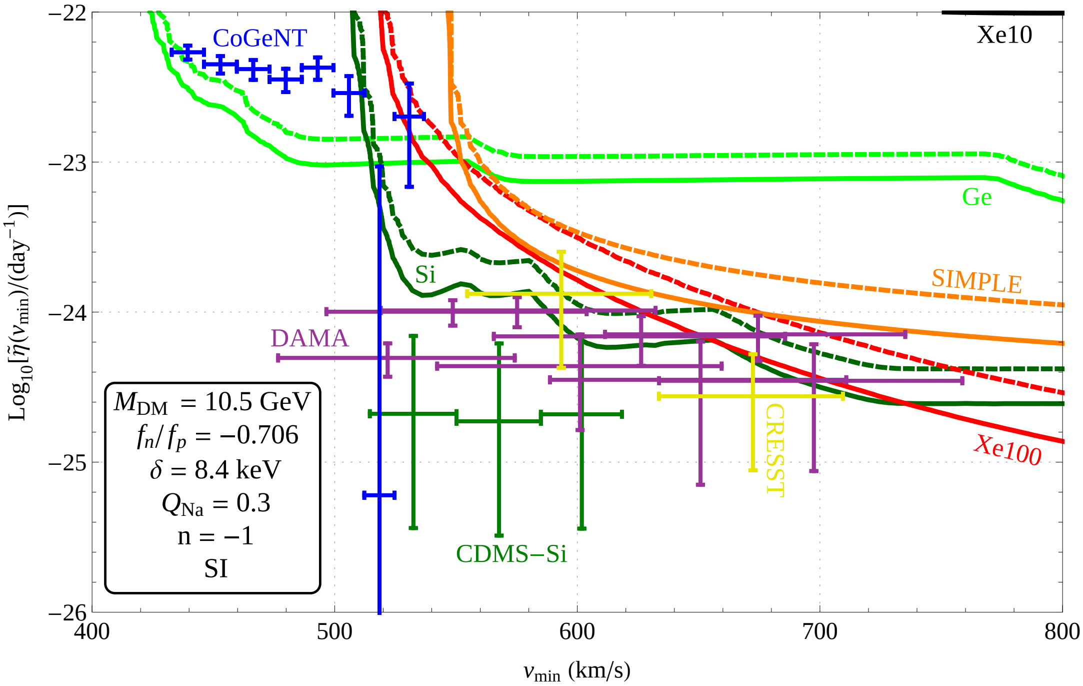

FIGURE 6.6: Momentum-dependent inelastic isospin-violating spin-independent halo-independent DM fit to the experimental data in $\tilde{\eta}$-v_{min} space with $n = -1$, $M_{DM} = 10.5$ GeV, $f_n/f_p = -0.706$, and $\delta = 8.4$ keV.

CoGeNT and CRESST-II data resembles a more realistic $\tilde{\eta}_0$ function for inelastic DM.

Moving on, let us consider momentum-dependent scattering in our study of halo-independent DM. Figures 6.6, 6.7, and 6.8 show the $\tilde{\eta}$ values and exclusion curves for inelastic IV SI DM with MD form factors with exponent $n = -1$, $n = 1$, and $n = 2$, respectively. In the $n = -1$ case, the benchmark parameter values are $M_{DM} = 10.5$ GeV, $f_n/f_p = -0.706$, and $\delta = 8.4$ keV. Since a form factor in the differential event rate proportional to $1/q^2$ results in a lower WIMP-proton cross section in order to compensate for the increase in events, and because $\tilde{\eta} \propto \sigma_p^{SI}$, there is an overall shift in the experimental results to lower values of $\tilde{\eta}$. The experimental picture is largely unchanged in that CDMS-Si does not agree with the results of CoGeNT and CRESST-II. On the other hand, CRESST-II and CoGeNT exhibit a greater amount of compatibility over both the elastic and inelastic momentum-independent IV models. Unfortunately, $n = -1$ MD scattering is not able to alleviate tensions between positive-signal and null experiments, and fails to construct agreement between measurements of $\tilde{\eta}_0$ and $\tilde{\eta}_1$.

As anticipated, Figure 6.7 demonstrates overall increases in measurements of $\tilde{\eta}$ for $n = 1$ MD scattering. The benchmark values of the parameters are given by $M_{DM} = 7.8$ GeV, $f_n/f_p = -0.808$, and $\delta = 4.0$ keV. The tensions between experimental results that existed

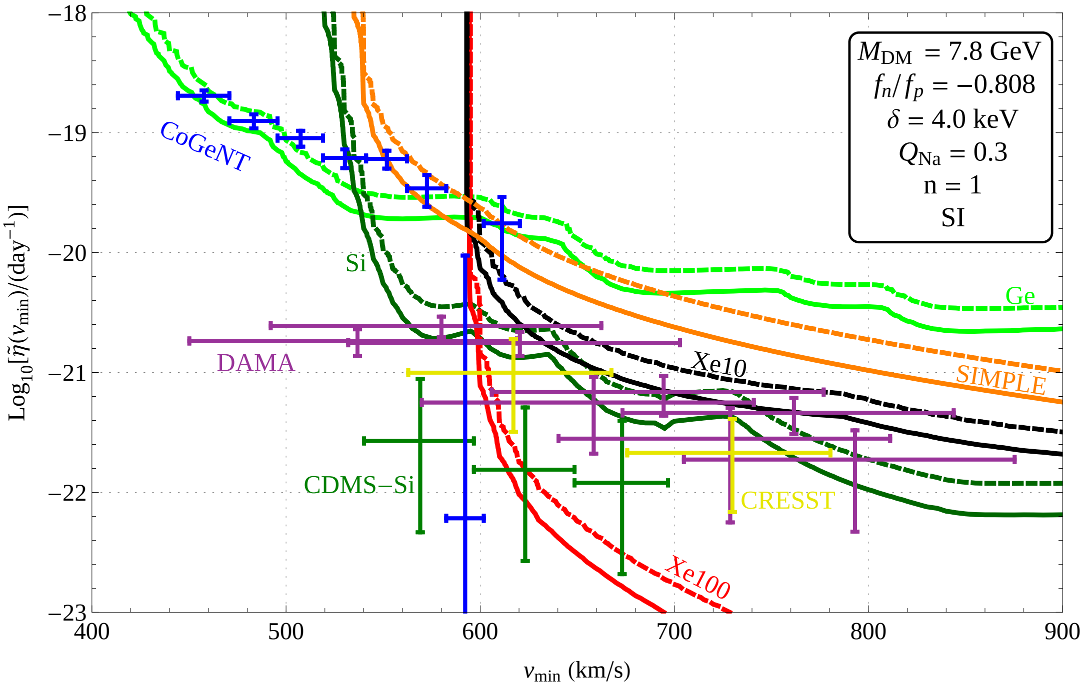

FIGURE 6.7: Momentum-dependent inelastic isospin-violating spin-independent halo-independent DM fit to the experimental data in $\tilde{\eta}$-v_{min} space with $n = 1$, $M_{DM} = 7.8$ GeV, $f_n/f_p = -0.808$, and $\delta = 4.0$ keV.

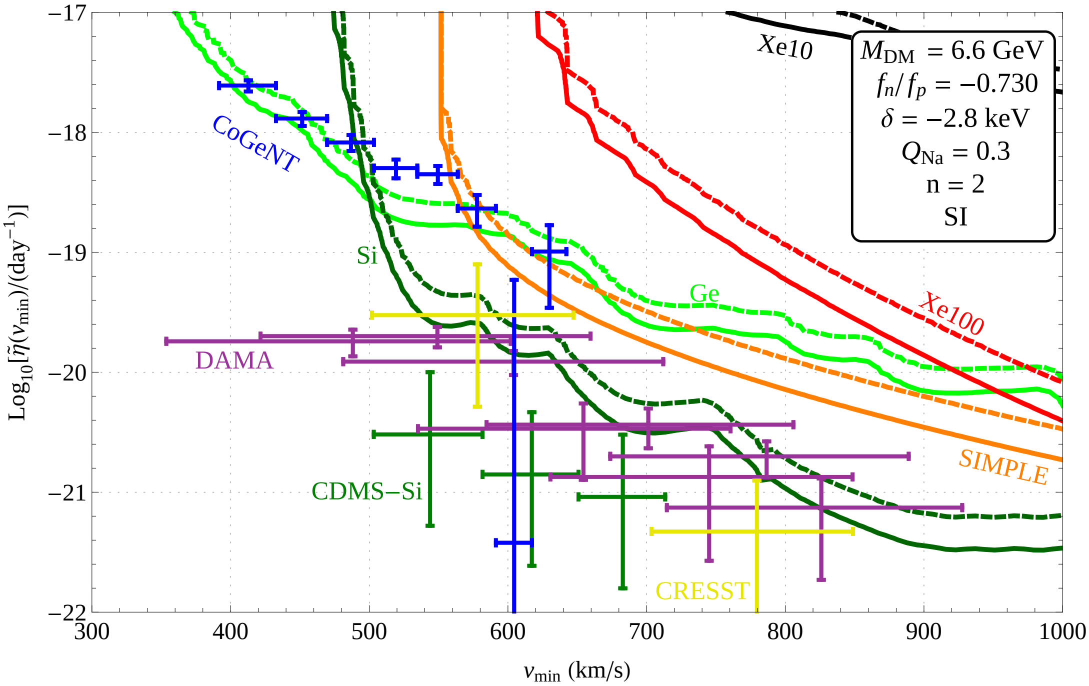

FIGURE 6.8: Momentum-dependent inelastic isospin-violating spin-independent halo-independent DM fit to the experimental data in $\tilde{\eta}$-v_{min} space with $n = 2$, $M_{DM} = 6.6$ GeV, $f_n/f_p = -0.730$, and $\delta = -2.8$ keV.

in all other models considered thus far remain largely unchanged. However, compared to the momentum-independent IV cases, the XENON100 bound is much more constraining due to the fact that in $n = 1$ scattering, the benchmark value of f_n/f_p deviates considerably from the optimal value of -0.7. As a result, a majority of the DAMA, CDMS-Si, and CRESST-II mearurements are ruled out.

Finally, Figure 6.8 investigates the impact of a MD form factor $\propto q^4$ for $M_{DM} = 6.6$ GeV, $f_n/f_p = -0.730$, and $\delta = -2.8$ keV. Even more so than in the $n = 1$ case, there is a trend in the positive-signal measurements to take on larger values of $\tilde{\eta}$. Again, this particular model suffers the same pitfalls as momentum-independent scattering. However in contrast to previous models, $n = 2$ MD scattering yields a much weaker 95.4% CL XENON100 constraint which is in complete agreement with all experimental measurements.

It should also be noted that for both $n = 1$ and $n = 2$ MD scattering, the CDMS-Ge bound is slightly diminished relative the $\tilde{\eta}_0$ measurements made by CoGeNT however, there is no compelling evidence to suggest any compatibility between the two experiments.

Arguably, the most illuminating realisation of our SI halo-independent analysis which is lost in the standard formalism, is the large incompatibility that exists between the DAMA and CRESST-II measurements. In the σ_p^{SI}-M_{DM} plane, DAMA and CoGeNT are found to be mildly compatible in some cases. On the other hand, since in v_{min}-space any reasonable model of the DM velocity distribution should result in $\eta_1 < \eta_0$, the halo-independent analysis reveals that DAMA is in strong contention with CRESST-II measurements.

6.5 Spin-dependent results

Consider now, a halo-independent analysis of direct detection data under a SD hypothesis of DM. The criteria upon which a successful fit to all the data is based will be the same as in the SI case. Our analysis of SD DM in Chapter 5 allows us to make a few predictions regarding a halo-independent analysis. Firstly, since SD favours larger values of the WIMP-nucleon cross section, we expect measurements of $\tilde{\eta}_0$ and $\tilde{\eta}_1$ to be large in comparison to SI DM. Furthermore, the SIMPLE and XENON100 exclusion curves will be the most consequential in constraining positive-signal data in $\tilde{\eta}$-v_{min} phase space. Finally, since silicon carries an isotope with spin, the

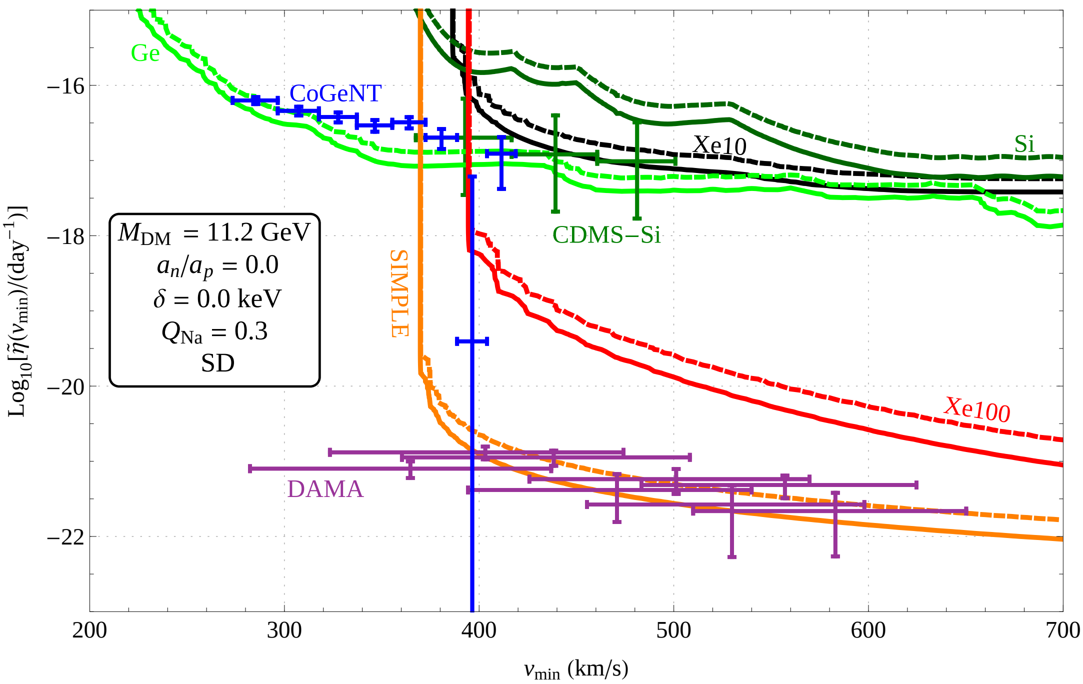

FIGURE 6.9: Elastic purely protonic spin-dependent halo-independent DM fit to the experimental data in $\tilde{\eta}$-v_{min} space with $M_{DM} = 8.0$ GeV, $a_n = 0.0$, $a_p = 1.0$, and $\delta = 0.0$ keV.

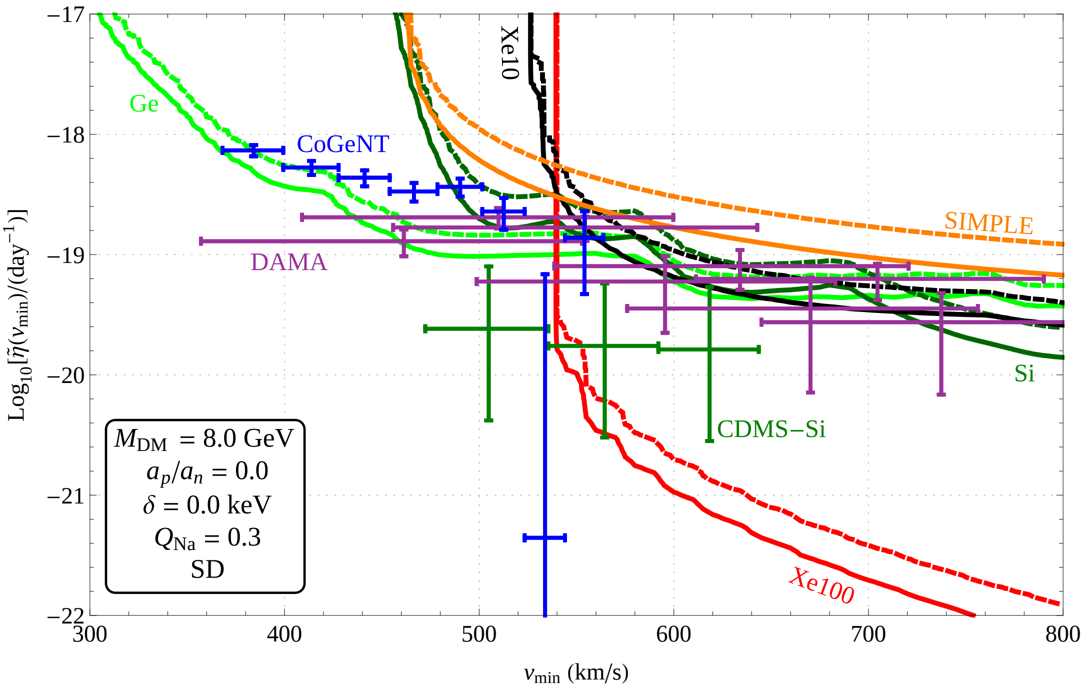

FIGURE 6.10: Elastic purely neutronic spin-dependent halo-independent DM fit to the experimental data in $\tilde{\eta}$-v_{min} space with $M_{DM} = 8.0$ GeV, $a_n = 1.0$, $a_p = 0.0$, and $\delta = 0.0$ keV.

CDMS-Si data will be able to provide measurements of $\tilde{\eta}_0$.

Figure 6.9 compares the unmodulated measurements of CoGeNT and CDMS-Si with the modulated measurements of DAMA against null upper limits in the elastic SD model with $a_n = 0$ and $a_p = 1$. The WIMP mass is taken to be $M_{DM} = 8.0$ GeV. A feature unique to this situation, is the exceptional agreement between the various $\tilde{\eta}$ measurements. Not only are the CDMS-Si and CoGeNT evaluations of $\tilde{\eta}_0$ mutually consistent, they are both sufficiently greater than measurements of $\tilde{\eta}_1$ procured by DAMA. Unfortunately, the positive-signal data is almost entirely ruled out by one or more null constraints. Constraints due to the CDMS-Ge bound have a marked consequence for the data points of CoGeNT, not to mention, large portions of the CDMS-Si favoured region. In addition, the SIMPLE exclusion curve rejects completely measurements made by CDMS-Si, and excludes most of the DAMA data points.

Setting $a_p = 0$ and $a_n = 1$ in the elastic SD model with $M_{DM} = 8.0$ GeV, one obtains in Figure 6.10 the results of the corresponding v_{min}-space analysis. Figure 6.10 illustrates a clear deterioration of the global fit between positive-signal experiments. In fact, of all the models considered thus far in the halo-independent formalism, purely neutronic SD scattering results in the greatest conflict between CoGeNT and DAMA data. In addition, measurements of the unmodulated $\tilde{\eta}_0$ function are in contention, specifically in the case of the lower-velocity CDMS-Si data points. On the other hand, there is significant weakening in the SIMPLE constraint; however, a combination of upper limits placed by CDMS-Ge and XENON100 conspire to exclude a majority of v_{min}-space.

Allowing the SD isospin-violation ratio to float, Figure 6.11 investigates halo-independent DM with elastic couplings for parameter values $M_{DM} = 8.74$ GeV and $a_n/a_p = 2.93$. Besides a slight improvement in the upper limit placed by SIMPLE, there is no strong evidence that suggests a generalized SD isospin violation ratio be used over the standard $a_n/a_p = 0$ case. Because the DAMA data points shift to larger values of $\tilde{\eta}$ relative XENON100, most of the measurements which probe higher values of v_{min} are excluded by XENON100. Also, a strengthenig occurs in the case of the CDMS-Si exclusion curve, and it remains that the SIMPLE and CDMS-Ge bounds combine to reject almost all umodulated measurements. Despite all of this, the CDMS-Si and CoGeNT measurements of $\tilde{\eta}_0$ are marginally compatible, and taking the upper limits of the CDMS-Si data points are sufficiently larger than the DAMA results for $\tilde{\eta}_1$.

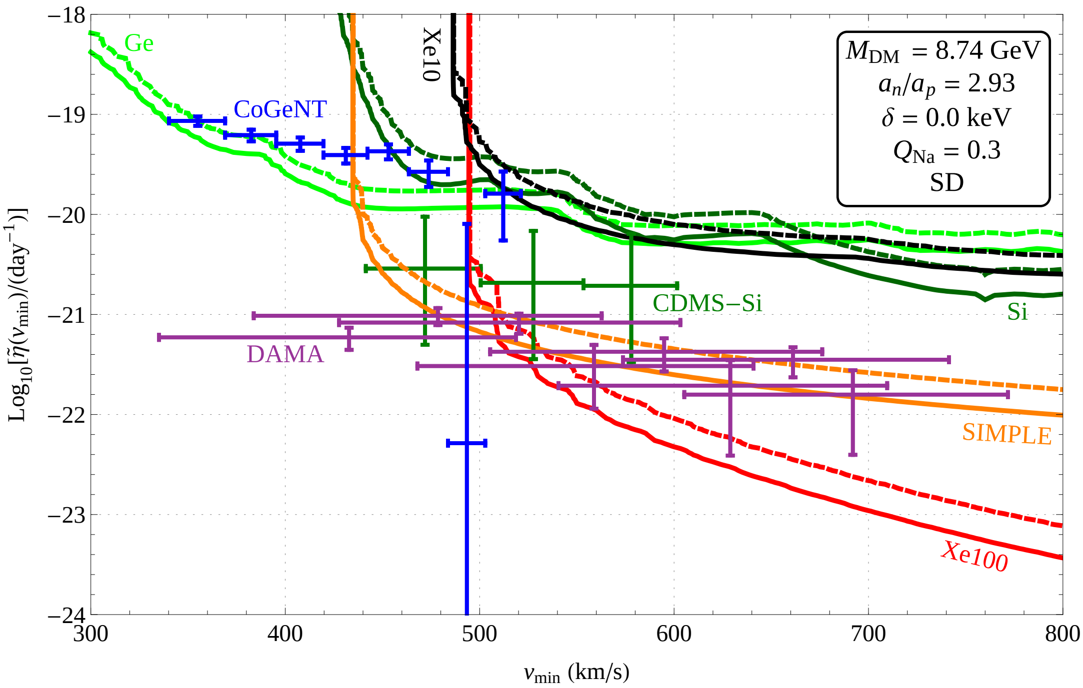

FIGURE 6.11: Elastic isospin-violating spin-dependent halo-independent DM fit to the experimental data in $\tilde{\eta}$-v_{min} space with $M_{DM} = 8.74$ GeV, $a_n/a_p = 2.93$, and $\delta = 0.0$ keV.

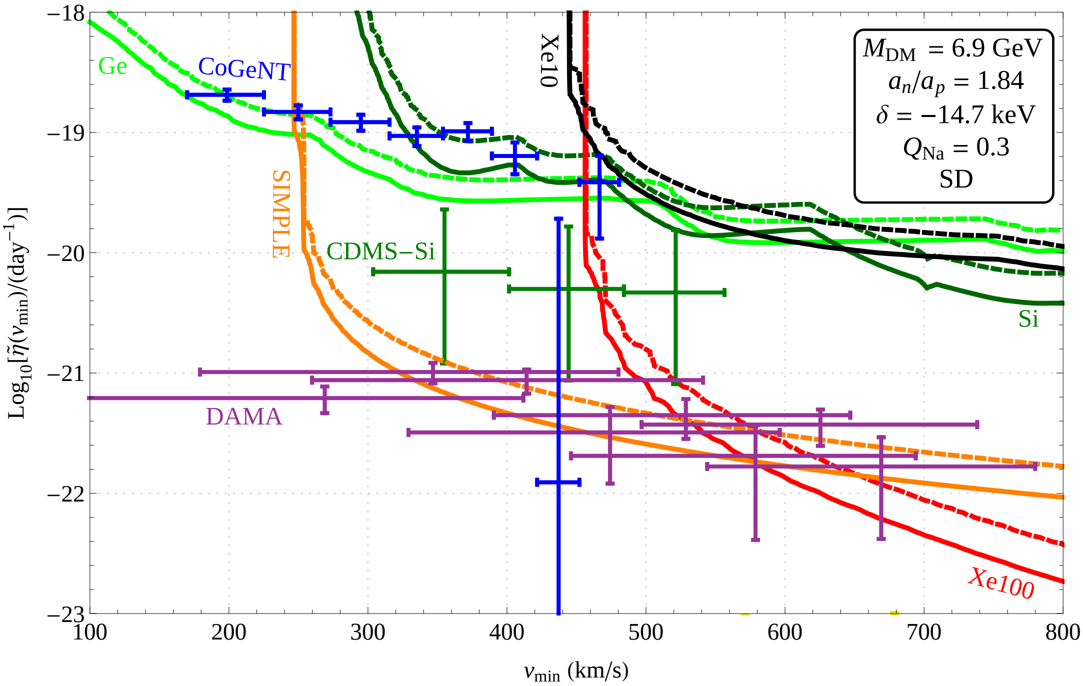

FIGURE 6.12: Inelastic isospin-violating spin-dependent halo-independent DM fit to the experimental data in $\tilde{\eta}$-v_{min} space with $M_{DM} = 6.9$ GeV, $a_n/a_p = 1.84$, and $\delta = -14.7$ keV.

Turning to a model which involves generalized inelastic and SD IV couplings, Figure 6.12 plots the results in v_{min}-space for parameter values $M_{DM} = 6.9$ GeV, $a_n/a_p = 1.84$, and $\delta = -14.7$ keV. There is an overall shift to lower values of v_{min} for all measurements of the $\tilde{\eta}$ functions with a relatively larger shift in the case of DAMA and CDMS-Si. Compared to the elastic IV SD scenario, the SIMPLE and CDMS-Si bounds have become comparatively more constraining at smaller values of v_{min}, whereas the XENON100 bound is found to reject fewer data points. Compatibility between unmoduated and modulated measurements is mostly unaffected with respect to the elastic IV SD case, although there is a small improvement between the CDMS-Si and DAMA data. Lastly, the smallest-velocity CDMS-Si measurement is in conflict with the values of $\tilde{\eta}_0$ favoured by CoGeNT.

The results of a generalized MD analysis of SD DM are found to not improve the halo-independent picture any further and we refer the interested reader to Appendix C to examine the $n = -1$ and $n = 1$ phase space plots.

Our investigation of SD dark matter epitomizes the apparent disconsonance between the standard and halo-independent formalisms. Consider the results of elastic protonic SD DM. In Chapter 5, strong disagreement between the DAMA and CoGeNT ROIs was obtained when the SHM was used to describe the DM velocity distribution. Conversely, in the halo-independent analysis, measurments made by DAMA were found to be compatible with those computed using CoGeNT data. Furthermore, almost all regions of v_{min}-space probed by CoGeNT were found to be excluded by the 95.4% CL CDMS-Ge bound however, in the σ_p-M_{DM} plots, large portions of the CoGeNT ROI were allowed by CDMS-Ge. As a result, this research has clearly demonstrated that both the standard and halo-independent formalisms of DM analysis must be implemented as complements to one another in order to make sophisticated conclusions regarding any model of DM.

Chapter 7

Summary and Conclusions

In the past, isospin-violating dark matter has shown great promise in its ability to explain the various excess signals reported by direct detection experiments while simultaneously circumventing null constraints. On the other hand, as the body of experimental data continues to grow, and as direct detection experiments become more sensitive to lower nuclear recoil energies, it appears as if models of dark matter which contain isospin-violating couplings have reached their limit.

In this dissertation, we reviewed the dark matter paradigm and introduced to the reader the field of direct detection of dark matter including: the theory behind dark matter event rates, and a discussion surrounding the most prominent ground-based dark matter searches. Following this, a review was given on the history of direct detection of dark matter and isospin-violating models with a focus on experimental and theoretical findings. In the final two chapters, our results for fitting current experimental data to isospin-violating dark matter and its possible extensions were presented in the manner of two formalisms: standard and halo-independent.

In the standard formalism, we investigated the experimental picture of dark matter through a series of $\sigma_p - M_{DM}$ phase space plots. Spin-independent, spin-dependent, mixed, elastic, inelastic, isospin-conserving, isospin-violating, and momentum-dependent models with possible combinations were all considered in our concerted effort to explain direct detection data. In all cases, there was a failure to meet the criteria under which an experimental fit could be deemed successful. Specifically speaking, in the spin-independent models, a combination of the XENON100 and CDMS-Si bounds caused any mutual overlap between positive-signal regions of interest to be rejected. In the spin-dependent case, the same went for the SIMPLE and XENON100 constraints. On the other hand, inelastic isospin-violating spin-dependent dark matter was shown to yield the best agreement between the DAMA and CoGeNT claims in a scenario which had yet to be explored until now. In this model, a fit to the DAMA and CoGeNT data was able to achieve a minimum value of the total chi-squared of $\chi^2_{tot} = 63.7$, which for 58 data points and 4 parameters corresponds to an optimal value of chi-squared of $\chi^2_{opt} = 54$. Finally, in the mixed model of DM, mutual positive-signal overlap that was able to avoid the XENON100 and CDMS-Si constraints was achieved and only marginally excluded by SIMPLE. Given that the SIMPLE bound has come under scrutiny, one might still imagine using isospin-violating DM as a way to explain current results.

The experimental picture was discovered to be no better in the halo-independent formalism. For the first time, the following halo-independent dark matter models were tested: inelastic and isospin-violating, inelastic-isospin-violating and momentum-dependent, and spin-dependent with all extensions. Furthermore, unique to this work, inelastic dark matter was studied in the confines of $\tilde{\eta} - v_{min}$ space. Out of all the models considered, none were able to produce consistent measurements of $\tilde{\eta}_0$ that could satisfy null constraints and be compatible with $\tilde{\eta}_1$ measurements. The most favourable model within the halo-independent formalism was the standard elastic purely protonic spin-dependent scenario which was the only model to obtain excellent agreement between CoGeNT and another unmodulated experiment.

Thus, we may conclude that our results do not support a dark matter interpretation of direct detection data in both the standard and halo-independent formalisms.

7.1 Future expectations for isospin-violating dark matter

The future of IVDM as a theoretical framework for explaining the excess signals of recent direct detection data will lie in the hands of upcoming experiments. As this work was nearing completion, the Large Underground Xenon (LUX) DM experiment released its first results corresponding to 85.3 live days$\times$118 kg of data acquisition [135]. So far there have been no observed events, resulting in an extracted limit on the DM-nucleon cross section which is the strongest reported by any experiment to date. Moreover, since LUX is composed of xenon, it will scale identically to XENON100 when converting IC bounds into IV ones. Thus the new LUX results are expected to rule out all positive-signal ROIs in both the SI and SD IVDM models. On the other hand, given the weakening of XENON100 that was observed in certain IV models of our halo-independent analysis, it is possible that the LUX bound may be avoided in this formalism.

It was pointed out in Chapter 5 that the much anticipated XENON1T DM search experiment will provide a greater sensitivity to probe the regions favoured by IVDM and could quite possibly exclude it altogether. In fact, if XENON1T fails to observe an excess signal that is unaccounted for by known backgrounds, then IVDM of the kind considered here will most likely be ruled out.

Another interesting upcoming direct detection experiment is DM-Ice. DM-Ice [136] is currently testing NaI crystal prototypes for a new DM experiment deployed deep in the ice of the South Pole. DM-Ice has the capacity to confirm or refute the DAMA/LIBRA claims of an annual modulation signature due to DM. This will be crucial in determining whether or not the DAMA signal is indeed a result of the DM annual modulation signature.

Whatever the future may hold for isospin-violating dark matter and its many extensions, let it remind us to continually think outside the simplest model of dark matter in our attempts to explain the mysterious and evasive nature of perhaps the most profound enigma of our time.

Appendix A

Integration of the Velocity Distribution

Results for the velocity integral of equation (2.18) using the SHM velocity distribution with a parameter α which allows one to turn on ($\alpha = 1$) or off ($\alpha = 0$) the truncating term. The analytic solutions are taken from reference [119]. We have the integral

$$\eta(E_{nr}) = \int_{v_{min}}^{\infty} \mathrm{d}^3 v \frac{f(\vec{v} + \vec{v_e})}{v}, \tag{A.1}$$

where the velocity distribution is given by

$$f(\vec{v}) = \begin{cases} \frac{1}{N}\big(\exp\left(-v^2/v_0^2\right) - \alpha \exp\left(-v_{esc}^2/v_0^2\right)\big) & \text{if } v < v_{esc} \\ 0 & \text{if } v > v_{esc} \end{cases}. \tag{A.2}$$

Using the definitions $x_{esc} = v_{esc}/v_0$, $x_{min} = v_{min}/v_0$, and $x_e = v_e/v_0$, where the velocities are magnitude values, the normalization constant N is found to be:

$$N = \pi^{3/2} v_0^3 \left[\mathrm{erf}(x_{esc}) - \frac{4}{\sqrt{\pi}} \exp\left(-x_{esc}^2\right) \left(\frac{x_{esc}}{2} + \alpha \frac{x_{esc}^3}{3} \right) \right]. \tag{A.3}$$

If $x_e + x_{esc} < x_{min}$ then,

$$\eta(E_{nr}) = 0. \tag{A.4}$$

If $x_e + x_{min} < x_{esc}$ then,

$$\begin{aligned}\eta(E_{nr}) &= \frac{\pi^{3/2} v_0^2}{2 N x_e} \Bigg[\mathrm{erf}(x_{min} + x_e) - \mathrm{erf}(x_{min} - x_e) \\ &\quad - \frac{4 x_e}{\sqrt{\pi}} \exp\left(-x_{esc}^2\right) \Bigg(1 + \alpha(x_{esc}^2 - x_e^2/3 - x_{min}^2) \Bigg) \Bigg]. \end{aligned} \tag{A.5}$$

If $x_{min} > |x_{esc} - x_e|$ and $x_e + x_{esc} > x_{min}$ then,

$$\begin{aligned}\eta(E_{nr}) &= \frac{\pi^{3/2} v_0^2}{2 N x_e} \Bigg[\mathrm{erf}(x_{esc}) - \mathrm{erf}(x_e - x_{min}) \\ &\quad - \frac{2}{\sqrt{\pi}} \exp\left(-x_{esc}^2\right) \Bigg(x_{esc} + x_e - x_{min} - \frac{\alpha}{3}(x_e - 2x_{esc} - x_{min})(x_{esc} + x_e - x_{min})^2 \Bigg) \Bigg]. \end{aligned} \tag{A.6}$$

Appendix B

Supplementary Phase Space Plots

Figures B.1 and B.2 are supplementary phase space plots showing the effects of a larger exothermic and endothermic inelastic mass splitting on the experimental fit to all the data, respectively.

Figure B.3 shows the experimental fit to all the data in f_n/f_p-δ phase space for a DM mass and cross section of $M_{DM} = 8.55$ GeV and $\sigma_p^{SI} = 2.90 \times 10^{-38}$ cm^2.

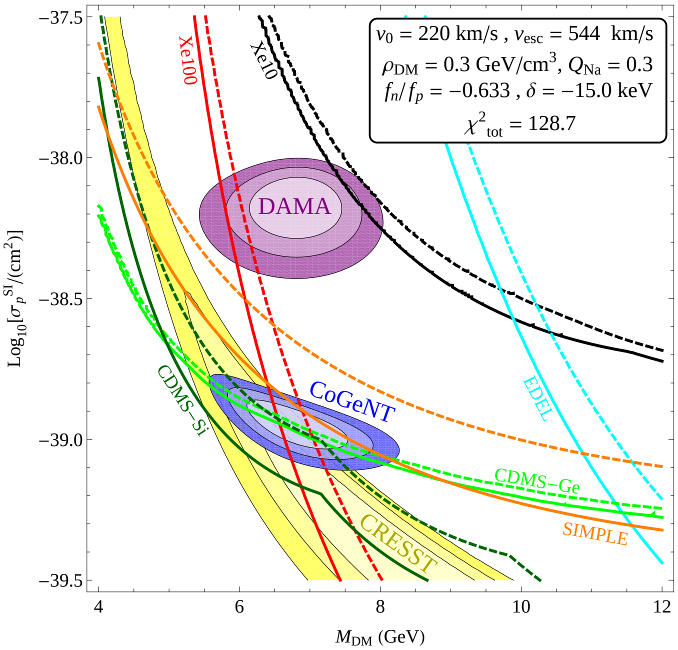

FIGURE B.1: Exothermic inelastic isospin-violating spin-independent DM fit to the experimental data in the $\sigma_p^{SI} - M_{DM}$ plane for larger (negative) mass splitting with $f_n/f_p = -0.633$ and $\delta = -15.0$ keV.

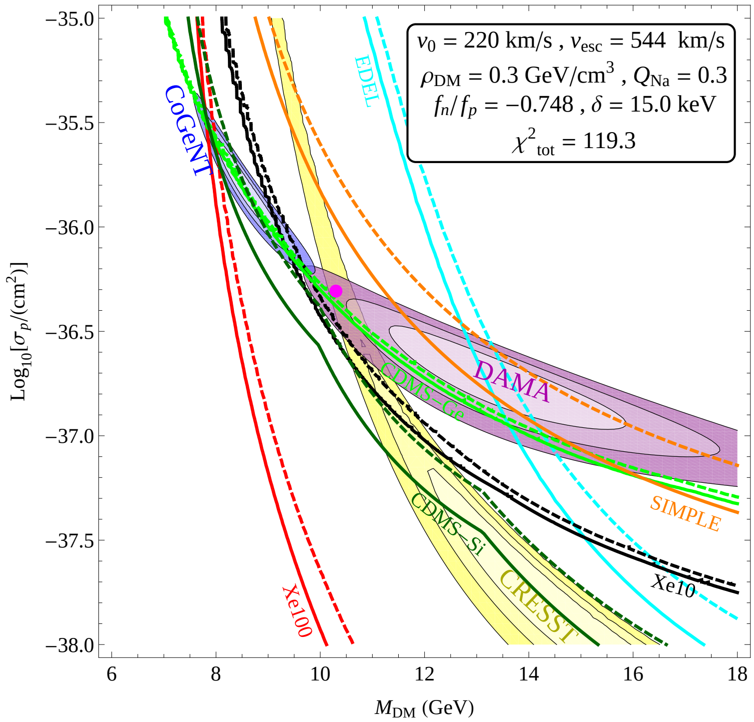

FIGURE B.2: Endothermic inelastic isospin-violating spin-independent DM fit to the experimental data in the $\sigma_p^{SI} - M_{DM}$ plane for larger mass splitting with $f_n/f_p = -0.748$ and $\delta = 15.0$ keV.

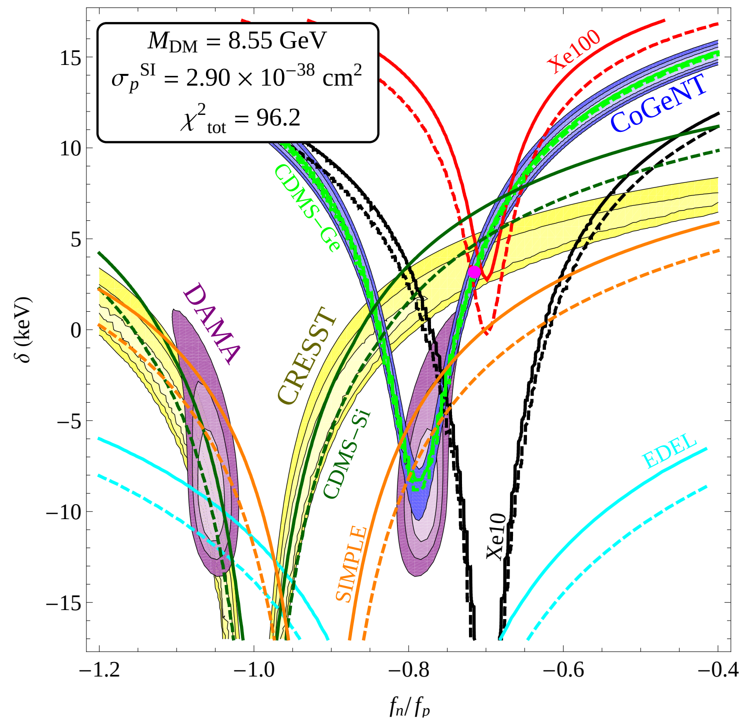

FIGURE B.3: Inelastic isospin-violating spin-independent fit to the experimental data in the f_n/f_p-δ plane with $M_{DM} = 8.55$ GeV and $\sigma_p^{SI} = 2.90 \times 10^{-38}$ cm^2.

Appendix C

Supplementary Halo-Independent Plots

Figures C.1 and C.2 show a $n = -1$ and $n = 1$ momentum-dependent, inelastic, isospin-violating, spin-dependent DM fit to the experimental data under the halo-independent formalism, respectively.

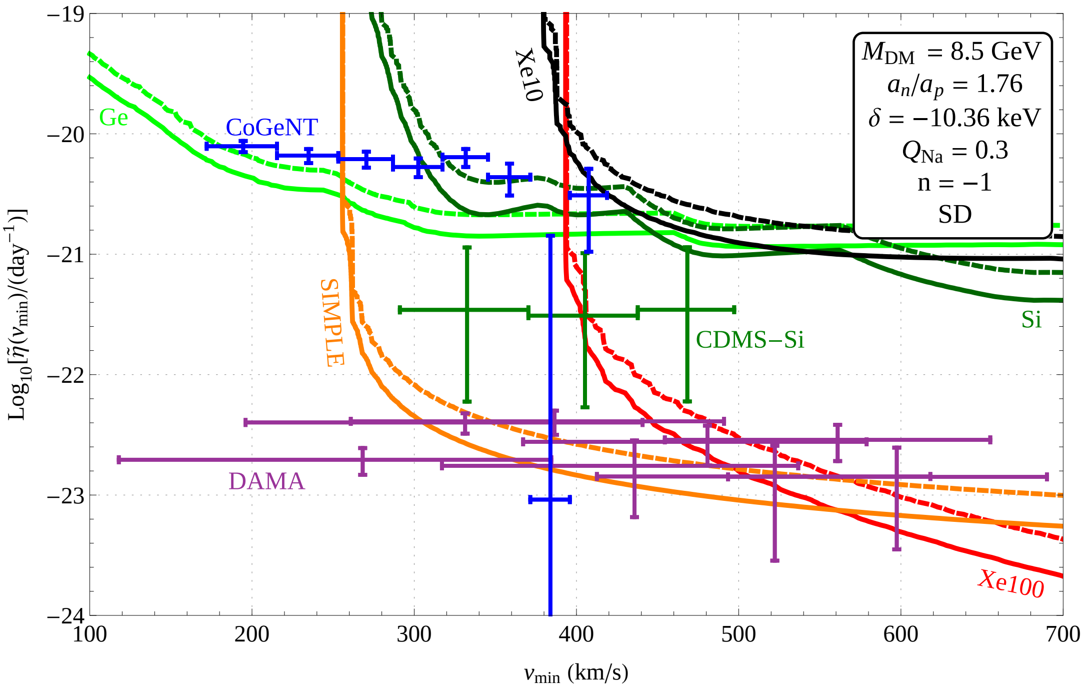

FIGURE C.1: Momentum-dependent inelastic isospin-violating spin-dependent halo-independent DM fit to the experimental data in $\tilde{\eta} - v_{min}$ space with $n = -1$, $M_{DM} = 8.5$ GeV, $a_n/a_p = 1.76$, and $\delta = -10.36$ keV.

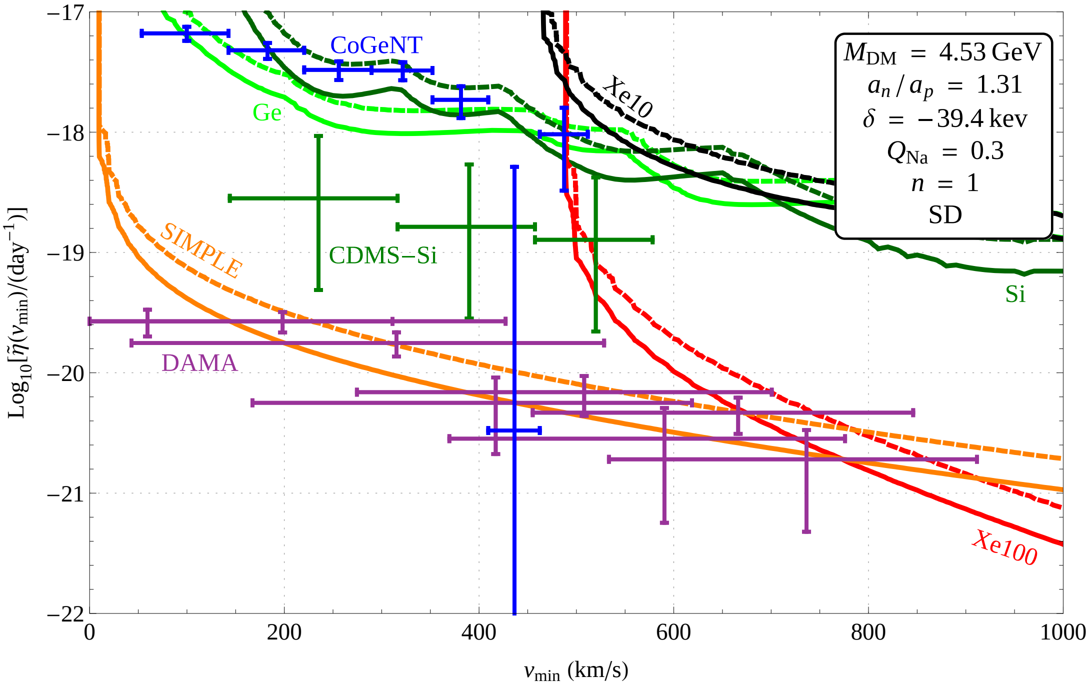

FIGURE C.2: Momentum-dependent inelastic isospin-violating spin-dependent halo-independent DM fit to the experimental data in $\tilde{\eta} - v_{min}$ space with $n = 1$, $M_{DM} = 4.53$ GeV, $a_n/a_p = 1.31$, and $\delta = -39.4$ keV.

References

[1] J. H. Jeans, Mon. Not. Roy. Astron. Soc. **82**, 122–132 (1922).

[2] E. Öpik, Bull. de la Soc. Astr. de Russie **12**, 150 (1915).

[3] J. C. Kapteyn, Astrophys. J. **55**, 302 (1922).

[4] J. H. Oort, Bull. Astron. Inst. Netherlands **6**, 249 (1932).

[5] F. Zwicky, Helvetica Physica Acta **6**, 110 (1933).

[6] S. van den Bergh, [arXiv:astro-ph/9904251].

[7] J. Bekenstein, Contemporary Physics **47**, 387–403 (2006), [arXiv:astro-ph/0701848].

[8] K. G. Begeman, A. H. Broeils, and R. H. Sanders, Mon. Not. Roy. Astron. Soc. **249**, 523 (1991).

[9] E. Corbelli and P. Salucci, [arXiv:astro-ph/9909252].

[10] L. Bergstrom, Rept. Prog. Phys. **63**, 793 (2000), [arXiv:hep-ph/0002126].

[11] J. P. Kneib, Y. Mellier, R. Pello, J. Miralda-Escude, J. F. Le Borgne, H. Bohringer, J. P. Picat, [arXiv:astro-ph/9504038].

[12] G. Hinshaw *et* al. [WMAP Collaboration], Astrophys. J. Suppl. **208**, 19 (2013), [arXiv:1212.5226 [astro-ph.CO]].

[13] P. A. R. Ade *et* al. [Planck Collaboration], [arXiv:1303.5076 [astro-ph.CO]].

[14] M. Taoso, G. Bertone, and A. Masiero, JCAP **0803**, 022 (2008), [arXiv:0711.4996 [astro-ph]].

[15] G. Steigman and M. S. Turner, Nucl. Phys. **B253**, 375 (1985).

[16] G. Jungman, M. Kamionkowski, and Kim Griest, Phys. Rept. **267**, 195 (1996), [arXiv:hep-ph/9506380].

[17] K. Garrett and G. Duda, Adv. Astron. **968283**, (2011), [arXiv: 1006.2483 [hep-ph]].

[18] S. De Lope Amigo, W. M.-Y. Cheung, Z. Huang, and S.-P. Ng, JCAP **0906**, 005 (2009), [arXiv:0812.4016 [hep-ph]].

[19] A. H. G. Peter, C. E. Moody, A. J. Benson, and M. Kamionkowski, PoS **IDM2010**, 084 (2011), [arXiv:1011.4970 [astro-ph.CO]].

[20] S. D. McDermott, H.-B. Yu, and K. Zurek, Phys. Rev. **D83**, 063509 (2011), [arXiv:1011.2907 [hep-ph]].

[21] D. N. Spergel and P. J. Steinhardt, Phys. Rev. Lett. **84**, 3760-3763 (2000), [arXiv:astro-ph/9909386].

[22] M. Bradac, D. Clowe, A. H. Gonzalez, M. Markevitch, and S. W. Randall, Astrophys. J. **679**, 1173-1180 (2008), [arXiv:0704.0261 [astro-ph]].

[23] A. Ibarra, D. Tran, and C. Weniger, Int. J. Mod. Phys. **A28**, 1330040 (2013), [arXiv:1307.6434 [hep-ph]].

[24] J. D. Lewin and P. F. Smith, Astropart. Phys. **6**, 87-112 (1996).

[25] M. Cannoni, J. D. Vergados, and M. E. Gomez, Phys. Rev. **D83**, 075010 (2011), [arXiv:1011.6108 [hep-ph]].

[26] J. L. Feng, J. Kumar, D. Marfatia, and D. Sanford, Phys. Lett. **B703**, 124-127 (2011), [arXiv:1102.4331 [hep-ph]].

[27] S. Golwala, Ph.D. thesis, UC Berkeley (2000).

[28] D. G. Cerdeno, M. Fornasa, J .H. Huh, and M. Peiro, Phys. Rev. **D87**, 023512 (2013), [arXiv:1208.6426 [hep-ph]].

[29] V. A. Bednyakov and F. Šimkovic, Phys. Part. Nucl. **37**, S106-S128 (2006), [arXiv:hep-ph/0608097].

[30] M. R. BUckley and W. H. Lippincott, Phys. Rev. **D88**, 056003 (2013), [arXiv:1306.2349 [hep-ph]].

[31] J. J. Fan, M. Reece, and L.-T. Wang, JCAP **1011**, 042 (2010), [arXiv:1008.1591 [hep-ph]].

[32] H.-B. Jin, S. Miao, and Y.-F. Zhou, Phys. Rev. **D87**, 016012 (2013), [arXiv:1207.4408 [hep-ph]].

[33] M. C. Smith *et* al. , Mon. Not. Roy. Astron. Soc. **379** 755-772 (2007), [arXiv:astro-ph/0611671].

[34] D. G. Cerdeno and A. M. Green, In *Bertone, G. (ed.): Particle dark matter, Cambridge University Press, New York, 347-369 (2010)*, [arXiv:1002.1912 [astro-ph.CO]].

[35] M. Kuhlen *et* al., JCAP **1002**, 030 (2010), [arXiv:0912.2358 [astro-ph.GA]].

[36] M. Vogelsberger *et* al., Mon. Not. Roy. Astron. Soc. **395**, 797-811 (2009), [arXiv:0812.0362 [astro-ph]].

[37] S. H. Hansen, B. Moore, M. Zemp, and J. Stadel, JCAP **0601**, 014 (2006), [arXiv:astro-ph/0505420].

[38] J. March-Russell, C. McCabe, and M. McCullough, JHEP **05**, 071 (2009), [arXiv:0812.1931 [astro-ph]].

[39] F. S. Ling, E. Nezri, E. Athanassoula, and R. Teyssier, JCAP **1002**, 012 (2010), [arXiv:0909.2028 [astro-ph.GA]].

[40] A. M. Green, Phys. Rev. **D66**, 083003 (2002), [arXiv:astro-ph/0207366].

[41] P. Belli, R. Cerulli, N. Fornengo, and S. Scopel, Phys. Rev. **D66**, 043503 (2002), [arXiv:hep-ph/0203242].

[42] J. D. Vergados, S. H. Hansen, and O. Host, Phys. Rev. **D77**, 023509 (2008), [arXiv:0711.4895 [astro-ph]].

[43] M. Lisanti, L. E. Strigari, J. G. Wacker, and R. H. Wechsler, Phys. Rev. **D83**, 023519 (2011), [arXiv:1010.4300 [astro-ph.CO]].

[44] J. F. Navarro, C. S. Frenk, and S. D. White, Astrophys. J. **462**, 563–575 (1996), [arXiv:astro-ph/9508025].

[45] N. Evans, C. Carollo, and P. de Zeeuw, Mon. Not. Roy. Astron. Soc. **318**, 1131 (2000), [arXiv:astro-ph/0008156].

[46] J. Diemand, M. Kuhlen, and P. Madau, Astrophys. J. **657**, 262-270 (2007), [arXiv:astro-ph/0611370].

[47] J. Diemand et. al., Nature **454**, 735-738 (2008), [arXiv:0805.1244 [astro-ph]].

[48] C. E. Aalseth *et* al. [CoGeNT Collaboration], Phys. Rev. Lett. **106**, 131301 (2011), [arXiv:1002.4703 [astro-ph.CO]].

[49] C. E. Aalseth *et* al. [CoGeNT Collaboration], Phys. Rev. **D88**, 012002 (2013), [arXiv:1208.5737 [astro-ph.CO]].

[50] S. Chang, J. Pradler, and I. Yavin, Phys. Rev. **D85**, 063505 (2012), [arXiv:1111.4222 [hep-ph]].

[51] J. Collar, Private communication.

[52] P. J. Fox, J. Kopp, M. Lisanti, and N. Weiner, Phys. Rev. **D85**, 036008 (2012), [arXiv:1107.0717 [hep-ph]].

[53] R. Bernabei *et* al. [DAMA Collaboration], Eur. Phys. J. **C56**, 333 (2008), [arXiv:0804.2741 [astro-ph]].

[54] R. Bernabei *et* al. [DAMA Collaboration], Phys. Lett. **B480**, 23 (2000), [arXiv:astro-ph/0305542].

[55] M. Farina, D. Pappadopulo, A. Strumia, and T. Volansky, JCAP **1111**, 010 (2011), [arXiv:1107.0715 [hep-ph]].

[56] J. I. Collar, Phys. Rev. **C88**, 035806 (2013), [arXiv:1302.0796 [physics.ins-det]].

[57] J. Schmaler *et* al. [CRESST Collaboration], [arXiv:0912.3689 [astro-ph.IM]].

[58] G. Angloher *et* al. [CRESST Collaboration], Eur. Phys. J. **C72**, 1971 (2012), [arXiv:1109.0702 [astro-ph.CO]].

[59] L. Stodolsky *et* al. [CRESST Collaboration], J. Phys. Conf. Ser. **384**, 012013 (2012),

[60] R. Foot, Phys. Rev. **D88**, 025032 (2013), [arXiv:1209.5602 [hep-ph]].

[61] E. Aprile *et* al. [XENON100 Collaboration], Astropart. Phys. **35**, 573-590 (2012), [arXiv:1107.2155 [astro-ph.IM]].

[62] E. Aprile *et* al. [XENON100 Collaboration], Phys. Rev. Lett. **107**, 131302 (2011), [arXiv:1104.2549 [astro-ph.CO]].

[63] E. Aprile *et* al. [XENON100 Collaboration], Phys. Rev. Lett. **109**, 181301 (2012), [arXiv:1207.5988 [astro-ph.CO]].

[64] C. Savage, G. Gelmini, P. Gondolo and K. Freese, Phys. Rev. **D83**, 055002 (2011), [arXiv:1006.0972 [astro-ph.CO]].

[65] J. I. Collar, [arXiv:1006.2031 [astro- ph.CO]].

[66] S. Yellin, Phys. Rev. **D66**, 032005 (2002), [arXiv:physics/0203002 [physics.data-an]].

[67] E. Aprile *et* al. [XENON100 Collaboration], [arXiv:1207.3458 [astro-ph.IM]].

[68] J. Angle *et* al. [XENON10 Collaboration], Phys. Rev. Lett. **107**, 051301 (2011), [arXiv:1104.3088 [astro-ph.CO]].

[69] J. I. Collar, [arXiv:1106.0653 [astro-ph.CO]].

[70] J. I. Collar, [arXiv:1010.5187 [astro-ph.IM]].

[71] J. M. Cline, Z. Liu, and W. Xue, Phys. Rev. **D87**, 015001 (2013), [arXiv:1207.3039 [hep-ph]].

[72] J. Angle *et* al. [XENON10 Collaboration], Phys. Rev. Lett. **107**, 051301 (2011).

[73] Z. Ahmed *et* al. [CDMS Collaboration], Phys. Rev. Lett. **102**, 011301 (2009), [arXiv:0802.3530 [astro-ph]].

[74] remove

[75] Z. Ahmed *et* al. [CDMS Collaboration], Phys. Rev.Lett. **106**, 131302 (2011), [arXiv:1011.2482 [astro-ph.CO]].

[76] Z. Ahmed *et* al. [CDMS Collaboration], [arXiv:1203.1309 [astro-ph.CO]].

[77] J. I. Collar, [arXiv:1103.3481 [astro-ph.CO]].

[78] R. Agnese *et* al. [CDMS Collaboration], [arXiv:1304.4279 [hep-ex]].

[79] M. Felizardo *et* al. [SIMPLE Collaboration], Phys. Rev. Lett. **108**, 201302 (2012), [arXiv:1106.3014 [astro-ph.CO]].

[80] J. I. Collar, [arXiv:1106.3559 [astro-ph.CO]].

[81] C. E. Dahl, J. Hall, and W. H. Lippincott, Phys. Rev. Lett. **108**, 259001 (2012), [arXiv:1111.6192 [astro-ph.CO]].

[82] E. Armengaud *et* al. [EDELWEISS Colaboration], Phys. Rev. **D86**, 051701(R) (2012), [arXiv:1207.1815 [astro-ph.CO]].

[83] M. W. Goodman and E. Witten, Phys. Rev. **D31**, 3059 (1985).

[84] A. Drukier and L. Stodolsky, Phys. Rev. **D30**, 2295 (1985)

[85] S. P. Ahlen et al., Phys. Lett. **B195**, 603 (1987).

[86] D. O. Caldwell, R. M. Eisberg, D. M. Grumm, M. S. Witherell, B. Sadoulet, F. S. Goulding, and A. R. Smith, Phys. Rev. Lett. **61**, 510 (1988).

[87] D. Reusser et al., Phys. Lett. **B255**, 143 (1991).

[88] S. Osetrov *et* al., in Proc. Workshop on Dark Matter in Astro–and Particle Physics (World Scientific, Singapore, 1997), eds. H. V. Klapdor–Kleingrothaus and Y. Ramach- ers, p. 473.

[89] E. G. A. Morales *et* al., Phys. Rev. **D51**, 1458 (1995).

[90] R. Bernabei *et* al., Phys. Lett. **B389**, 757 (1996).

[91] R. Bernabei *et* al., Nucl. Phys. B (Proc. Suppl.) **70**, 79 (1998).

[92] D. E. Di Gregorio *et* al., Nucl. Phys. (Proc. Suppl.) **B38**, 394 (1995).

[93] M. Beck, Nucl. Phys. B (Proc. Suppl.) **35**, 150 (1994).

[94] L. Baudis *et* al., Phys. Rev. **D59**, 022001-1 (1998).

[95] P. F. Smith *et* al., Phys. Lett. **B379**, 299 (1996).

[96] A. Bottino *et* al., Phys. Lett. **B295**, 330 (1992).

[97] A. Bottino, F. Donato, G. Mignola, S. Scopel, P. Belli, and A. Incicchitti, Phys. Lett. **B402**, 113-121 (1997), [arXiv:hep-ph/9612451].

[98] A. Bottino *et* al., Nucl. Phys. B (Proc. Suppl.) **28A**, 314 (1992).

[99] R. Barbieri, M. Frigeni, and G.F. Giudice, Nuc. Phys. **B311**, 725 (1989).

[100] A. Kurylov and M. Kamionkowski, Phys. Rev. **D69**, 063503 (2004), [arXiv:hep-ph/0307185].

[101] F. Giuliani, Phys. Rev. Lett. **95**, 101301 (2005), [arXiv:hep-ph/0504157].

[102] J. Kopp, T. Schwetz, and J. Zupan, JCAP **1002**, 014 (2010), [arXiv:0912.4264 [hep-ph]].

[103] S. Chang, J. Liu, A. Pierce, N. Weiner, and I. Yavin, JCAP **1008**, 018 (2010), [arXiv:1004.0697 [hep-ph]].

[104] M. T. Frandsen, F. Kahlhoefer, J. March-Russell, C. McCabe, M. McCullough, and K. Schmidt-Hoberg, Phys. Rev. **D84**, 041301 (2011), [arXiv:1105.3734 [hep-ph]].

[105] J. Kopp, T. Schwetz, and J. Zupan, JCAP **1203**, 001 (2012), [arXiv:1110.2721 [hep-ph]].

[106] C. Arina, Phys. Rev. **D86**,123527 (2012), [arXiv:1210.4011 [hep-ph]].

[107] J. Yang, [arXiv:1302.5416 [hep-ph]].

[108] J. L. Feng, J. Kumar, D. Sanford, Phys. Rev. **D88**, 015021 (2013), [arXiv:1306.2315 [hep-ph]].

[109] P. Fox, J. Liu, and N. Weiner, Phys. Rev. **D83**, 103514 (2011), [arXiv:1011.1915 [hep-ph]].

[110] M. T. Frandsen, F. Kahlhoefer, C. McCabe, S. Sarkar, and K. Schmidt-Hoberg, JCAP **1201**, 024 (2012), [arXiv:1111.0292 [hep-ph]].

[111] P. Gondolo and G. B. Gelmini, JCAP **1212**, 015 (2012), [arXiv:1202.6359 [hep-ph]].

[112] E. Del Nobile, G. B. Gelmini, P. Gondolo, J.-H. Huh, [arXiv:1304.6183 [hep-ph]].

[113] M. T. Frandsen, F. Kahlhoefer, C. McCabe, S. Sarkar, and K. Schmidt-Hoberg, JCAP **1307**, 023 (2013), [arXiv:1304.6066 [hep-ph]].

[114] N. Bozorgnia, J. Herrero-Garcia, T. Schwetz, and J. Zupan, JCAP **1307**, 049 (2013), [arXiv:1305.3575 [hep-ph]].

[115] E. Del Nobile, G. Gelmini, P. Gondolo, and J.-H. Huh, JCAP **1310**, 048 (2013), [arXiv:1306.5273 [hep-ph]].

[116] C. Arina, [arXiv:1310.5718 [hep-ph]].

[117] M. T. Ressell and D. J. Dean, Phys. Rev. **C56**, 535–546 (1997), [arXiv:hep-ph/9702290].

[118] P. C. Divari, T. S. Kosmas, J. D. Vergados, and L. D. Skouras, Phys. Rev. **C61**, 054612 (2000).

[119] C. McCabe, Phys. Rev. **D82**, 023530 (2010), [arXiv:1005.0579 [hep-ph]].

[120] T. Piffl *et* al., [arXiv:1309.4293 [astro-ph.GA]].

[121] R. Catena and P. Ullio, JCAP **1008**, 004 (2010), [arXiv:0907.0018 [astro-ph.CO]].

[122] F. Nesti and P. Salucci, PoS **DSU2012**, 041 (2012), [arXiv:1212.3670 [astro-ph.CO]].

[123] C. Moni Bidin, G. Carraro, R. A. Mendez, and R. Smith, Astrophys. J. **751**, 30 (2012), [arXiv:1204.3924 [astro-ph.GA]].

[124] J. Bovy and S. Tremaine, Astrophys. J. **756**, 89 (2012), [arXiv:1205.4033 [astro-ph.GA]].

[125] Y. Bai and J. Berger, [arXiv:1308.0612 [hep-ph]].

[126] J. Cline and A. Frey, Phys. Rev. **D84**, 075003 (2011), [arXiv:1108.1391 [hep-ph]].

[127] W. de Boer and M. Weber, JCAP **1104**, 002 (2011), [arXiv:1011.6323 [astro-ph.CO]].

[128] P. W. Graham, R. Harnik, S. Rajendran, and P. Saraswat, Phys. Rev. **D82**, 063512 (2010), [arXiv:1004.0937 [hep-ph]].

[129] S. Chang, G. D. Kribs, D. Tucker-Smith, and N. Weiner, Phys. Rev. **D79**, 043513 (2009), [arXiv:0807.2250 [hep-ph]].

[130] K. Schmidt-Hoberg and M. W. Winkler, JCAP **0909**, 010 (2009), [arXiv:0907.3940 [astro-ph.CO]].

[131] P. Beltrame, [arXiv:1305.2719 [astro-ph.CO]].

[132] L. S. Lavina, [arXiv:1305.0224 [hep-ex]].

[133] M. Drees and C.-L. Shan, JCAP **0706**, 011 (2007), [astro-ph/0703651].

[134] P. J. Fox, G. D. Kribs, and T. M. P. Tait, Phys. Rev. **D83**, 034007 (2011), [arXiv:1011.1910 [hep-ph]].

[135] D. S. Akerib *et* al. [LUX COllaboration], [arXiv:1310.8214 [astro-ph.CO]].

[136] J. Cherwinka, *et* al., Astropart. Phys. **35**, 749 (2012), [arXiv:1106.1156 [astro-ph.HE]].